RECTIFIED ELECTROOSMOTIC FLOW IN MICROCHANNELS USING ZETA POTENTIAL MODULATION – CHARACTERIZATION AND ITS APPLICATION IN PRESSURE GENERATION AND PARTICLE TRANSPORT

By

WEN-I WU, B.Sc., M.Sc.

A Thesis Submitted to the School of Graduate Studies in Partial
Fulfilment of the Requirements for the Degree Doctor of Philosophy

McMaster University

RECTIFIED ELECTROOSMOTIC FLOW IN MICROCHANNELS USING ZETA POTENTIAL MODULATION – CHARACTERIZATION AND ITS APPLICATION IN PRESSURE GENERATION AND PARTICLE TRANSPORT

McMaster University DOCTOR OF PHILOSOPHY (2011) Hamilton, Ontario

TITLE: Rectified electroosmotic flow in microchannels using Zeta potential modulation – Characterization and its application in pressure generation and particle transport

AUTHOR: Wen-I Wu

B.Sc. (Cheng-Kung University)

M.Sc. (National Taiwan University)

SUPERVISOR: Professor P. Ravi Selvaganapathy

NUMBER OF PAGES: 122

ABSTRACT

Microfluidic devices using electroosmotic flows (EOFs) in microchannels have been developed and widely applied in chemistry, biology and medicine. Advantages of using these devices include the reduction of reagent consumption and duration for analysis. Moreover the velocity profile of EOFs, in contrast to the parabolic profile found in pressure-driven flows, has a plug-like profile which contributes significantly less to solute dispersion. It also requires no valve to control the flow, which is done with the appropriate application of electrical potentials, thus becomes one of the favourite techniques for sample separation. However, high potentials of several hundred volts are usually required to generate sufficient EOF. These high potentials are not practical for general usage and could cause electrical hazard in some applications. One of the possible solutions is the introduction of zeta potential modulation. The EOF in a microchannel can be controlled by the zeta potential at the liquid/solid interface upon the application of external gate potentials across the channel walls. Combined with AC EOF, it can rectify the oscillating flows and generate pressure that can be used for microfluidic pumping applications. Since the flow induced by the alternating electric field is unsteady and periodic, it is critical to visualize the flow with high spatial and temporal resolutions in order to understand fluid dynamics. A novel method to obtain high temporal resolution for high frequency periodic electrokinetic flows using phase sampling technique in micro particle image velocimetry (PIV) measurements are first developed in order to characterize the AC electroosmotic flow. After that, the principle of zeta potential modulation is demonstrated to transport particles, cells, and other micro organisms using rectified AC EOF in open microchannels. The rectified flow is obtained by synchronous zeta-potential modulation with the driving potential in the microchannel. Subsequently, we found that PDMS might not be the best material for some pumping and biomedical applications as its hydrophobic surface property makes the priming process more difficult in small microchannels and also causes significant protein adsorption from biological samples. A more hydrophilic and biocompatible material, polyurethane (PU), was chosen to replace PDMS. A polyurethane-based soft-lithography microfabrication including its bonding, interconnect integration and in-situ surface modification was developed providing better biocompatibility and pumping performance. Finally, an electroosmotic pumping device driven by zeta potential modulation and fabricated by PU soft lithography was presented. The problem of channel priming is solved by the capillary force induced by the hydrophilic surface. Its flow rate and pressure output were found to be controllable through several parameters such as driving potential, gate potential, applied frequency, and phase lag between the driving and gate potentials.

ACKNOWLEDGEMENTS

I would like to take this opportunity to express my sincere gratitude to people who helped and supported me, both personally and professionally, towards the completion of this dissertation.

First, I would like to thank my advisor, Professor Ravi Selvaganapathy. I am forever grateful for not only patiently instructing me and giving me supports, but also providing me advice on a large variety of subjects, ranging from microfluidics to chemistry, especially when I had troubles or failures during my research. Having lots of setbacks is terrible, however no one can guide you through is even worse. I am lucky having my supervisor around whenever I needed him.

Second, I would like to thank Professor Chan Ching for giving me access to resources within the laboratories and his valuable fluidic advice. The question he always asked "What's your progress this week?" made everyone anxious however it did keep me moving forward.

I also would like to thank Zhilin and Dorris (CEDT staff) for their time and help in cleanroom. I would like to thank Dr. Ewing for his mentoring in the particle image velocimetry and Kyla Sask for her support in surface modification and protein adsorption, of which results are presented in Chapter 4 and Chapter 6 respectively.

I am grateful to my group members, Geetha Mahadevan, Pouya Zangeneh, Bala Ganapathysubramani, Sarvesh Upadhyaya, Simon Loane, Arash Noori, Mohammed Hasnain, Salman Safari, Pouya Rezai, Siawash Shinwary, Bo Dang, Shihad Islam, Ali Shahid, Peter Lee, Leo Hsu and many others for their friendship, tremendous help and useful discussions.

Finally, I would like to thank my parents for their continuous support and encouragement over the years. Lastly, and most importantly, a big thank you to my wife, Tricia, for her understanding, selfless love and support during all these years. Without her, it would have been much harder for me to pursue the PhD degree. For that, I would like to dedicate this thesis to her.

TABLE OF CONTENTS

LIST OF FIGURES

LIST OF TABLES

LIST OF ABBREVIATIONS

AC	Alternating current
CCD	Charge-coupled device
C. elegans	Caenorhabditis elegans
CMOS	Complementary metal-oxide-semiconductor
CVD	Chemical vapour deposition
DC	Direct current
DI water	Deionized water
DMA	N,N'-dimethylacetamide
DMF	Dimethylformamide
DMSO	Dimethyl sulfoxide
EDL	Electrical double layer
EK	Electrokinetic
EOF	Electroosmotic flow
FEFC	Field-effect flow control
FET	Field effect transistor
fg	Fibrinogen
FPS	Frame per second
IC	Integrated circuit
IgG	Immunoglobulins
IPA	Isopropyl alcohol
LIFPA	laser-induced fleorescence photobleaching anemometer
MDI	4,4'-Methylene-bis (phenyl-diisocyanate)
MeO–PEO–OH	Monomethoxy-poly(ethylene glycol)
PBS	Phosphate buffered saline
PC	Polycarbonate
PDMS	Polydimethylsiloxane
PEO	Polyethylene oxide
PIV	Particle image velocimetry
PMMA	Poly(methyl methacrylate)
PolyMPC	Poly(2-methacryloyloxyethyl phosphorylcholine)
PS	Polystyrene
PTFE	Polytetrafluoroethylene
PTV	Particle tracking velocimetry
PU	polyurethane
RMS	Root mean squre
SEM	Scanning electron microscope
SR	Sampling rate
TEA	Triethylamine
THF	Tetrahydrofuran

Chapter 1 Introduction

An overview of the project goal and an introduction to the use of electroosmotic flow in microfluidic systems will be given in this chapter. Furthermore, an outline of the thesis will also be provided.

1.1 Project Goal

This research aims to understand the modulation of zeta potential in microfluidic devices and develops methods to control fluid flow in the micro scale. It further develops various methods and fabrication processes to characterize zeta potential modulation. Finally, application of zeta potential modulation in practice to transport particles and fluids is demonstrated.

1.2 Electroosmotic Flows in microfluidics

Microfluidic devices using electroosmotic flows (EOFs) in microchannels have been developed and are widely applied in chemistry, biology and medicine. Advantages of using these devices include the reduction of reagent consumption and duration for analysis. Moreover the velocity profile of EOFs, in contrast to the parabolic profile found in pressure-driven flows, has a plug-like profile which contributes significantly less to solute dispersion. It also requires no valve to control the flow, which is done with the appropriate application of electrical potentials, thus becomes one of the favourite techniques for sample separation. However, high potentials of several hundred volts are usually required to generate sufficient EOF. These high potentials are not practical for general usage and could cause electrical hazard in some applications. One of the possible solutions is the introduction of zeta potential modulation. The EOF in a microchannel can be controlled by the zeta potential at the liquid/solid interface upon the application of external gate potentials across the channel walls. This technique was first developed using fused silica capillaries with conductive layer deposited in the external surface in the early ’90[1]. Relatively high voltages of several kilo volts were applied on the external conductive layer to generate sufficient electric field to affect the zeta potential at the inner surface of capillary. With new advances in microfabrication, capillaries with much thinner walls become possible, thus allowing the use of lower potentials to affect the zeta potential and consequently control the EOF inside the capillary. The other major issue associated with EOF is water electrolysis which causes gas generation upon the application of electrical potential at the metal electrode in the solution.

AC EOF can be used to eliminate gas generation by using alternating potentials with sufficiently high frequencies, so that the electrolysis reaction on the electrodes can be reversed and bubble generation can be prevented. However, this only results in oscillating flows and zero net flow. Zeta potential modulation can be used to increase or decrease the EOF by an external gate potential. Combined with AC EOF, it can rectify the oscillating flows and generate pressure that can be used for microfluidic pumping applications.

1.3 Contributions to Articles

The following describes my contribution to the articles constituting Chapters 4-7. Professor Ravi Selvaganapathy provided guidance with the initial research focus and idea development and Professor Chan Ching provided the advice on the fluid mechanism and manuscript revision. Dr. Ewing who is the coauthor for Chapter 4 provided the guidance on the principle of particle image velocimetry and matlab® programing. Part of Chapter 6 was collaborated with Kyla Sask who is also the coauthor for Chapter 6 and provided her assistance on surface modification and protein adsorption. For all the research and study, I designed and performed all phases of the projects, from literature search, experiments through to data analysis. I generated the first drafts of the manuscripts and the initial responses to the comments of the journal reviewers.

1.4 Thesis outline

This thesis contains eight chapters presented in “sandwich” style. The content of the remaining chapters is summarized as follows:

Chapter 2: Literature review

This chapter provides the background information necessary to understand the concepts involved in designing an electroosmotic driven microfluidic device to perform specific functions; in this study pressure generation and particle transportation. The basics of electroosmotic flow are discussed and the primary relationships and equations are provided including the electric double layer, zeta potential, electroosmotic flow and zeta potential modulation. The major problems of DC-operated electroosmotic flows are also detailed. Finally, several techniques that can potentially improve these problems by modifying the surface charge are presented. Among them, the method of zeta potential modulation via externally applied gate voltage is chosen due to its easy integration with microfluidic devices and capability of dynamic control.

Chapter 3: Rectified AC electroosmotic flow Using Zeta Potential Modulation

In this chapter, the concept of the zeta potential modulation which is used to control the surface charge and its primary relationships and equations are introduced. Subsequently, the control of electroosmotic flows with the synchronized gate and driving potentials to rectify AC electroosmotic flows and the implementation in microfluidic system is presented. A validation using microfluidic device is also detailed including its microfabrication, electroosmotic mobility measurements. Since the flow induced by the alternating electric field is unsteady and periodic, it is critical to visualize the flow with high spatial and temporal resolutions in order to understand the fluid dynamics.

Chapter 4: Periodic Flow Characterization by Micro-PIV Measurement

In this chapter, a novel method to obtain high temporal resolution for high frequency periodic electrokinetic flows using phase sampling technique in micro particle image velocimetry (PIV) measurements are developed in order to characterize the AC electroosmotic flows. In this technique, the flow characteristics over a single cycle can be reconstructed from these unique points obtained over larger timeframe spanning a number of cycles, thus allowing measurement at higher temporal resolutions. Without upgrading to the costly high-speed equipment, this technique can be used to measure the flow variation of forced periodic flows and characterize their flow responses that can be helpful to obtain the optimum performance by choosing proper operation conditions and device designs.

Chapter 5: Particle transportation by Rectified Electroosmotic Flows

In this chapter, the principle of zeta potential modulation is demonstrated to transport particles, cells, and other micro organisms using rectified AC EOF in open microchannels. The rectified flow is obtained by synchronous zeta-potential modulation with the driving potential in the microchannel. The effects of dielectric layer, driving electric field, gate potential, applied frequency, and phase lag between the driving and gate signals on the particle velocities were investigated and used to control the particle movement that can be a low-cost alternative to optical tweezers in certain applications. Moreover, in this study we found that PDMS might not be the best material for some pumping and biomedical applications as its hydrophobic surface property makes the priming process more difficult in small microchannels and also causes significant protein adsorption from protein-containing fluids.

Chapter 6: Polyurethane-based Soft-lithography Microfabrication

To solve these problems, a more hydrophilic and biocompatible material, polyurethane (PU), was chosen to replace PDMS. PU is currently one of the most common material used in biomedical devices and can be processed easily due to its thermoplastic properties, thus make it the best candidate. In this chapter, we develop a polyurethane-based soft-lithography microfabrication to replace PDMS while providing better biocompatibility and pumping performance. Two new fabrication processes for making thin, transparent, flexible polyurethane (PU)-based microfluidic devices. We give details not only on the fabrication of microchannels but also their bonding, and the integration of fluidic interconnections as well as surface modification with hydrophilic polyethylene oxide (PEO) to improve their biocompatibility.

Chapter 7: Pressure Generation of Rectified Electroosmotic Pumps

Finally, an electroosmotic pumping device driven by zeta potential modulation and fabricated by PU soft lithography was presented. The flow rate and pressure output are characterized through several parameters as driving potential, gate potential, applied frequency, and phase lag between the driving and gate potentials. Direct measurements of the pressure generation are detailed without using flow rate conversion which has been found in most previous literature.

Chapter 8: Conclusions and Recommendations for Future Work

In this chapter, an overview of the conclusions and discussion that were presented in the previous chapters of this thesis is provided. Followed by the research contributions, recommendations for the future work are presented.

Chapter 2 Literature Review

2.1 Electroosmotic Flow

Electroosmotic flow was first reported in 1809 by the Russian physicist F.F. Reuss[2], and since then, it has been used for sample analysis, separation and mixing processes, drug delivery and total analysis systems. A typical electroosmotic fluid flow in a capillary tube is shown in Figure 2-1. When the capillary tube is negatively charged due to the formation of the electrical double layer, the applied electric field exerts a force in the direction of the cathode on the layer with excess ions of positive charge near the surface. The positively charged layer then viscously drags the rest of the electrolyte solution along with it and causes the fluid flow towards the cathode.

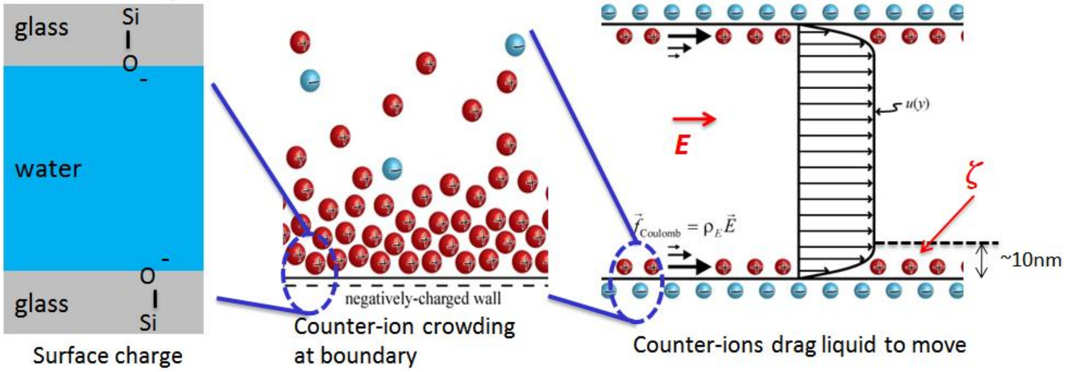

Figure 2-1 Electroosmotic flow in capillary tubes

2.2 Electric Double layer

At the interface between a solid and a polar liquid, most materials will develop a surface potential due to the separation of charges that occur because of pH dependent deprotonation or association of surface groups[3]. Consequently co-ions will be repelled and counter ions will be attracted to the surface and form the so called electrical double layer (EDL). In Figure 2-2(a), close to the surface a layer of immobilized counter ions will form due the electrostatic interaction with the surface. Further away from the surface the counter ions will have more freedom to move. This layer is referred to as the diffuse layer.

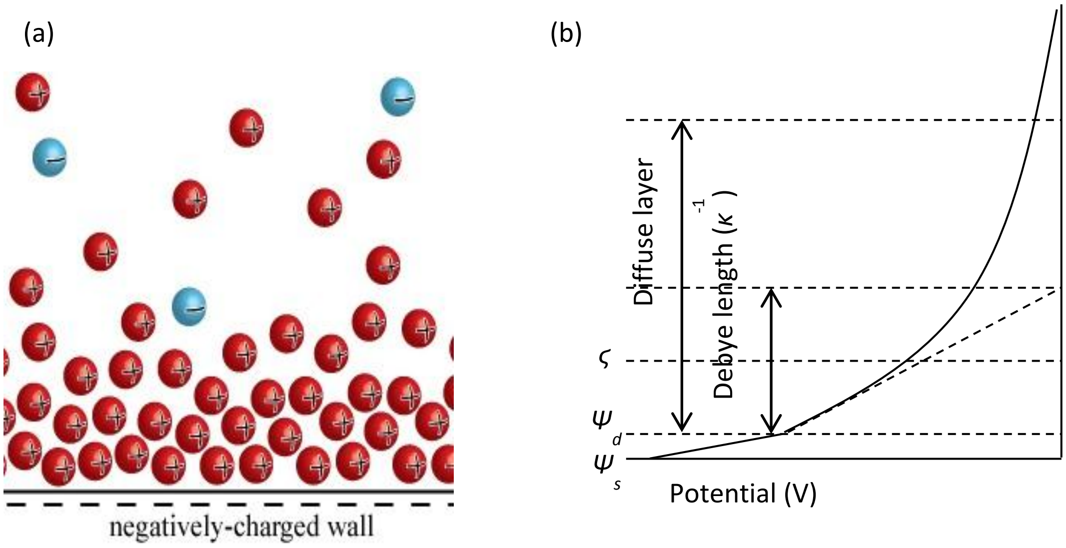

Figure 2-2 (a) Schematic of EDL according to the Stern model. (b) Schematic of electric potential profile.

The theory for diffuse layer was developed by Gouy and Chapman in the early 1900s[3]. Considering the case of a flat surface, ion distribution in the diffuse layer results in a net electric charge, this can be related to the electrokinetic potential as follows:

$$\varepsilon \nabla^2 \Psi = -\rho_f \tag{1}$$

For a one-dimensional problem, the equation simplifies to

$$\varepsilon \frac{d^2 \Psi}{dx^2} = -\rho_f \tag{2}$$

where ***ε*** is the dielectric constant, ***ψ*** is the electrical potential, ***x*** is the distance normal to the charged surface, and $\boldsymbol{\rho_f}$ is the space charge density which can be written by

$$\rho_f = \sum_{i=1}^{N} z_i e n_i \tag{3}$$

where n_i is the ionic number concentration of the i^{th} species, z_i is the valence of the i^{th} ionic species, e is the magnitude of the fundamental charge on an electron, and N is the number of ionic species in the electrolyte solution. Equation (1) and (3) are combined to give

$$\varepsilon \frac{d^2 \Psi}{dx^2} = -\sum_{i=1}^{N} z_i e n_i \tag{4}$$

The right-hand side can be written in terms of ψ using the Boltzmann distribution to result in the Poisson-Boltzmann equation

$$\varepsilon \frac{d^2\Psi}{dx^2} = -\sum_{i=1}^{N} z_i e n_{i\infty} \exp(-\frac{z_i e \Psi}{k_B T}) \tag{5}$$

Where k_B is the Boltzmann constant and T is the temperature. The Poisson-Boltzmann equation defines the electrical potential distribution in the diffuse layer adjacent to a charged surface. In the case of planar EDL, one can obtain an analytical solution for ψ for symmetric electrolytes without any further approximations. In particular, the Gouy-Chapman analysis does not require the linearization of the Boltzmann approximation and is a nonlinear theory. Considering a general case with symmetric electrolyte (z_+=-z_- =z). Equation (5) can be written as[3]

$$\varepsilon \frac{d^2\Psi}{dx^2} = -2zen_\infty \sinh(\frac{ze\Psi}{k_B T}) \tag{6}$$

The boundary conditions are ψ = Ψ_s when x = 0 and ψ=0 when x approaches infinity. Then Equation (6) can be solved to get a solution as

$$\Psi = 2\ln\left[\frac{1+\exp(-\kappa x)\tanh(\Psi_s/4)}{1-\exp(-\kappa x)\tanh(\Psi_s/4)}\right] \tag{7}$$

$$\text{Where } \Psi = \frac{ze\Psi}{k_B T} \text{ and } \Psi_s = \frac{ze\Psi_s}{k_B T} \tag{8}$$

Ψ is the dimensionless potential. In Equation (7), the κ^{-1} is defined as the Debye length shown in Equation (8). The Debye length is a measure of the EDL thickness, and is a property of the electrolyte solution. Table 2-1 shows the values of the Debye length for different electrolyte concentrations for the case of z = 1.

$$\kappa^{-1} = (\frac{\varepsilon k_B T}{2e^2 z^2 n_\infty})^{1/2} \tag{9}$$

Ionic Strength, mol/dm^{-3}	**Debye Length, nm**
10^{-6}	304
10^{-4}	30.4
10^{-2}	3.04

Table 2-1 Debye length under different ionic concentration[4]

2.3 Debye–Hückel Approximation

When the surface potential is small, the term $ze\psi/k_BT$ is smaller than unity and equation (6) can be rewritten as

$$\frac{d^2\Psi}{dx^2}=\frac{2e^2z^2n_\infty}{\varepsilon k_BT}\Psi=\kappa^2\Psi \tag{10}$$

Equation (10) is the linearized version of the Poisson-Boltzmann equation and is referred to as the Debye-Hückel approximation. Its solution is given by

$$\Psi=\Psi_s\exp(-\kappa x) \tag{11}$$

A comparison between the exact solution and the Debye-Hückel approximation solution is shown in Figure 2-3. The Debye–Hückel solution normally gives fairly close Ψ / Ψ_s variations for Ψ_s values as high as 3.[4]

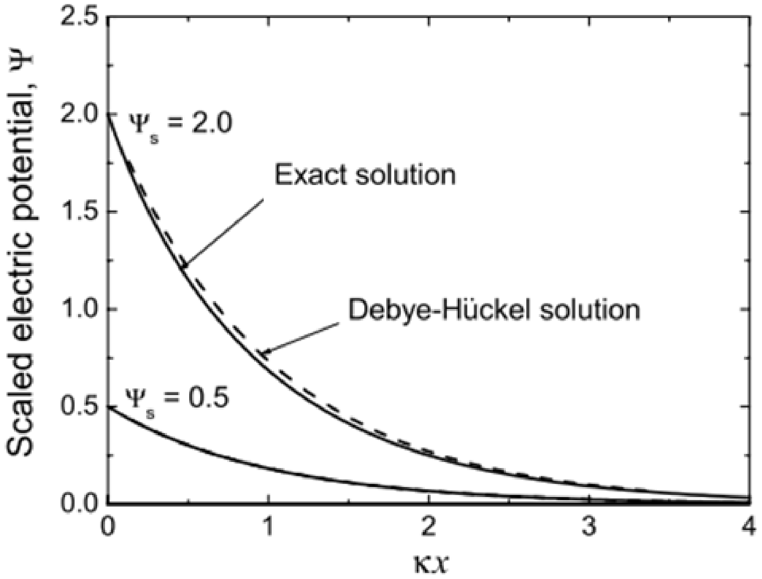

Figure 2-3 Comparison between exact and Debye- Hückel solutions.[4]

2.4 Zeta Potential

The Gouy–Chapman treatment of the diffuse double layer runs into some difficulties at small κx values when the surface potential, ψ_s , is large, because it has assumed that the ions are point charges and that the inner boundary of the EDL is located at the surface of the particle or material under consideration. In real systems, ions are of finite size and they can approach a surface to a distance not less than their radii. Stern[5] proposed a model in which the EDL inner boundary is given by approximately one hydrated ion radius. This inner boundary is referred to as the Stern plane. Ions whose centers are located within the Stern plane and they are considered to be immobile. Ions whose centers are located beyond the Stern plane form the diffuse mobile part of the electric double layer. Consequently, the mobile inner part of the electric double layer is located between one to two radii away from the surface. This boundary is referred to as the shear plane as shown in Figure 2-2(a). It is on this plane where the no-slip boundary condition is assumed to apply. The potential at the shear plane is referred to as the electrokinetic potential, more commonly known as the zeta potential (ζ). Experimental evidence suggests that the zeta potential is very slightly different in magnitude from the potential at Stern plane; it is customary to identify the Stern potential with the zeta potential.

When an axial potential is applied along the channel, the ions in the EDL will move with the electric field E. Due to viscous coupling between the EDL and the bulk fluid, a flow with an almost uniform velocity profile over the channel width will develop. The electroosmotic velocity for infinitesimally thin EDL is given by the Helmholtz-Smoluchowski relation[2]

$$u_{EO} = \mu_{EO} E = \frac{-\zeta\epsilon}{\mu} E \qquad \text{for DC case}$$

$$\text{Or} \quad u_{EO} = \mu_{EO} E = \frac{-\zeta\epsilon}{\mu} E \, sin(\omega t) \qquad \text{for AC case with sinusoidal waveform (12)}$$

where μ_{EO} is the electroosmotic mobility, ζ is the zeta potential, ε is the liquid dielectric constant, μ is the dynamic viscosity of the liquid, ω is the angular frequency of the applied potential and t is the time. The derivation of Equation (12) is showed in the following section.

2.5 Governing Equations

Assuming incompressible Newtonian fluid with constant viscosity, the bulk motion is governed by the incompressible Navier-Stokes equations

$$\rho \frac{\partial u}{\partial t} + \rho u \cdot \nabla u = -\nabla p + \mu \nabla^2 u + \rho g + f_b \tag{13}$$

f_b means any other body force. In electrokinetic transport processes, this body force arises due to an electric field. The electric body force on the fluid is given by

$$f_E = \rho_f E - \frac{1}{2} E \cdot E \nabla \varepsilon + \frac{1}{2} \nabla \left[\left(\rho \frac{\partial \varepsilon}{\partial \rho} \right)_T E \cdot E \right] \tag{14}$$

In our case, we assume an incompressible medium with constant electric permittivity. Hence, only the first term will be considered, which means[3]

$$f_E = \rho_f E = -\rho_f \nabla \Psi \tag{15}$$

Then equation (13) becomes

$$\rho \frac{\partial u}{\partial t} + \rho u \cdot \nabla u = -\nabla p + \mu \nabla^2 u + \rho g - \rho_f \nabla \Psi \tag{16}$$

For a steady-state creeping flow where inertia is neglected, equation (16) becomes

$$\nabla p = \mu \nabla^2 u + \rho g - \rho_f \nabla \Psi \tag{17}$$

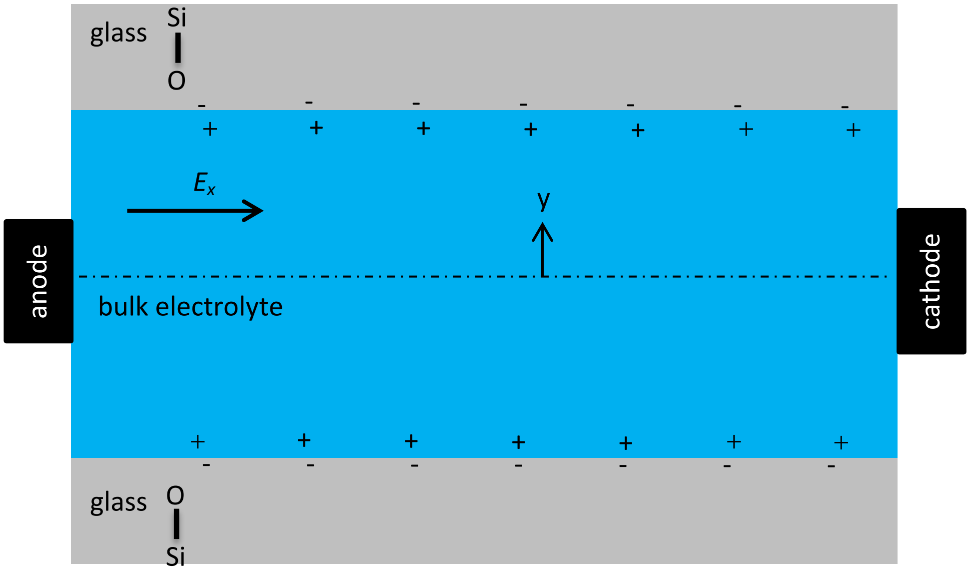

Figure 2-4 Electroosmotic and pressure-driven flows in a microchannel[4]

For simplicity, a two-dimensional and fully developed steady flow with no-slip boundary conditions are assumed, as shown in Figure 2-4. The momentum equation is

$$\mu \frac{d^2 u_x}{dy^2} = \frac{dp}{dx} + \rho_f \frac{\partial \phi}{\partial x} \tag{18}$$

The term *dp/dx* is a negative constant under the assumption of fully developed flow, and can be represented by *dp/dx* = $-p_x$. For a low surface potential, the free charge density can be written in[4]

$$\rho_f = -\varepsilon\kappa^2\Psi = -\varepsilon\kappa^2\zeta\frac{\cosh(\kappa y)}{\cosh(\kappa h)} \tag{19}$$

Substituting equation (19) into equation (18), we obtain

$$\mu\frac{d^2u_x}{dy^2} = -p_x + \varepsilon\kappa^2E_x\zeta\frac{\cosh(\kappa y)}{\cosh(\kappa h)} \tag{20}$$

The boundary conditions are $u_x = 0$ when $y = h$ (no-slip condition) and $du_x/dy = 0$ when $y = 0$ (symmetry flow in y- direction). The solution of equation (20) is given by

$$u_x(y) = u_x = \frac{h^2p_x}{2\mu}\left[1-\left(\frac{y}{h}\right)^2\right] - \frac{\varepsilon E_x\zeta}{\mu}\left[1-\frac{\cosh(\kappa y)}{\cosh(\kappa h)}\right] \tag{21}$$

The first term represents the pressure-driven flow velocity and it is normally referred to as Poiseuille flow. The second term represents the electroosmotic flow velocity which has a plug-like profile. For given system properties, the local velocity is directly proportional to the applied electrical potential gradient. Also, equation (21) shows the electroosmotic velocity is much dependent on the EDL thickness, κ^{-1}.

The pressure driven term in Equation (21) can be rewritten as the normalized local velocity which can be expressed by

$$\frac{u_{x,press}}{(h^2p_x/2\mu)} = U_{x,press} = 1-(\frac{y}{h})^2 \tag{22}$$

The normalized local velocity is parabolic when plotted against normalized transverse position, *y/h*, as shown in Figure 2-5(a). Figure 2-5(b) shows the variation of the normalized local velocity due to electroosmotic flow, written as

$$\frac{u_{x,el}}{-\left(\varepsilon E_x\zeta/\mu\right)} = \frac{u_{x,el}}{-\Omega E_x} = U_{x,el} = 1-\frac{\cosh(\kappa h\cdot\frac{y}{h})}{\cosh(\kappa h)} \tag{23}$$

where

$$\Omega = \frac{\varepsilon\zeta}{\mu} \tag{24}$$

The normalized electroosmotic velocity profile in the microchannel depends strongly on the dimensionless channel gap κh. For large κh values, the velocity profile becomes flat in the central region of the flow channel. In practice, for channels of h < 10μm with a (1:1) electrolyte concentration as low as 10^{-6}M, the κh value is quite large and the velocity profile is fairly flat.[4]

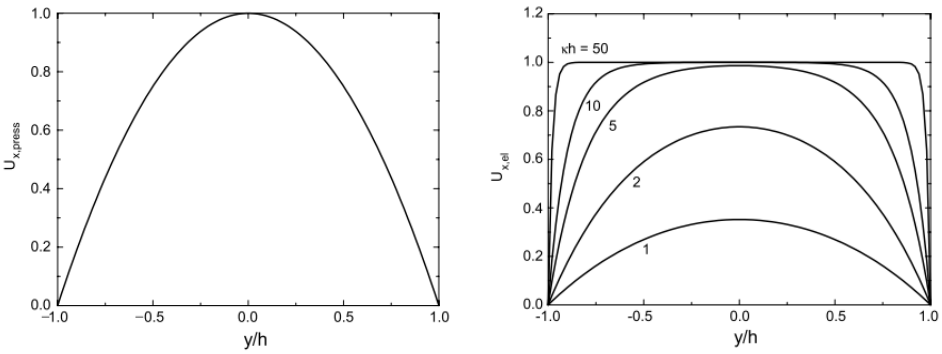

(a) Pressure driven flow (b)Electroosmotic flow

Figure 2-5 Variation of dimensionless local velocity[4]

From equation (21), the velocity distribution for purely electroosmotic flow can be expressed as

$$u_x(y) = -\frac{\varepsilon E_x \zeta}{\mu}\left[1 - \frac{\cosh(\kappa y)}{\cosh(\kappa h)}\right] \tag{25}$$

For κh >> 1, the electroosmotic velocity profile becomes uniform, given by the Helmholtz–Smoluchowski expression

$$u_x(y) = -\frac{\varepsilon E_x \zeta}{\mu} \tag{26}$$

This velocity can also be known as the electroosmotic velocity u_{EO}.

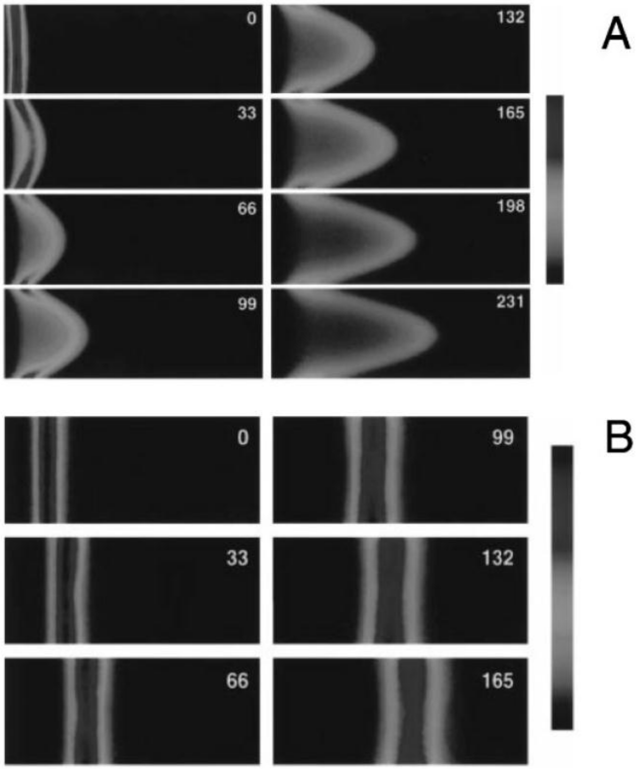

Figure 2-6 Development of low profiles. A) pressure-driven flow; B) electroosmotic flow[6]

Equation (21) shows that pressure-driven flow becomes impractical as the channel width *h* becomes very small. Meanwhile, the channel width *h* does not affect the electroosmotic velocity. Consequently, electroosmotic flow becomes practical for very narrow channels. Moreover, Equation (22) and Figure 2-6(a) shows that pressure-driven flow has a parabolic distribution of the flow velocities with the largest velocity at the center of the channel and zero velocity at the walls. On the other hand, Equation (23) and Figure 2-6(b) shows a plug-like profile with a very uniform velocity distribution across the entire cross section of the channel. Hence, electroosmotic flow has the minimum dispersion when transporting fluid zones as shown in Figure 2-6. Combined with its other advantages, like no moving parts, compact size, make it becomes more suitable for micro total analysis systems and lab-on-chip applications.

2.6 Electroosmotic Pumping Operated in DC

The first electroosmotic pump structure (generating significant pressure) was demonstrated by Theeuwes[7] in 1975. Other notable contributions include that of Gan *et al.*[8] who demonstrated pumping of several electrolyte chemistries; and Paul *et al.*[8] and Zeng *et al.*[9] who demonstrated generation of pressures in the order of 10 atm and higher. Yao *et al.*[10]presented experimentally validated, full Poisson–Boltzmann models for porous electroosmotic pumps. They demonstrated a pumping structure less than 2

cm^3 in volume that generates 33 ml/min and 1.3 atm at 100 V. Despite the improvement in the performances (flow rate and pressure), several issues remain to be investigated.

2.6.1 Issue I: Electrolysis

The main issue with electroosmotic pump is water electrolysis and bubble generation at the metal electrodes. During operation, electroosmosis and electrolysis occur at the same time. Electroosmosis requires ion current in the fluid and a continuous ion current is possible only if electrolysis takes place at the metal electrodes. Water electrolysis is occurred when the electrodes are operated with more than 2V. Hydrogen is generated at the cathode and oxygen is generated at the anode.

Anode: $2H_2O \rightarrow 4H^+ + 4e^- + O_2$ E^O=-1.23 V

Cathode: $2H_2O + 2e^- \rightarrow H_2 + 2OH^-$ E^O=-0.83 V

E^O represents the standard reduction potential with respect to a standard hydrogen electrode at 300K, 1 atm and 1 Molar electrolyte concentration. The negative sign indicates that spontaneous evolution of hydrogen and oxygen is not thermodynamically favourable. However, when a potential of more than 2V is applied across the electrochemical system, these reactions occur at the anode and the cathode and any residual voltage is applied across the solution that is used to generate electroosmotic flow. The gases generated as part of the reaction will form bubbles in the electrolytes, and these bubbles tend to clog the channel and result in an increased hydraulic resistance to fluid flow. Also, pH value of the electrolyte will fluctuate near the electrodes, which would cause the change of zeta potential.

Current methods of avoiding bubble generation include placing the metal electrodes outside the channels using gel[11], replacing the electrode with inert electrodes[12], using liquid bridges[13] or ion exchange membrane[14] as ion conductors. Another method is to use AC driving signals to eliminate electrolysis effect. Some metals have a certain degree of permeability for hydrogen. Running the pump in AC mode will make each electrode work as an anode and a cathode. If the hydrogen generated during the cathodic half-cycle is stored in the metal electrode and removed during the anodic half-cycle, the electrodes will be bubble-free. However, use of symmetrical AC signal will produce no net flow. Therefore, other methods independent of the driving signal are needed to rectify the flow direction. Mounting rectifying valve system[12], applying asymmetric AC driving signals[15], and modulating the zeta potential[13] have been proposed to eliminate the bubble generation. Other methods that run in AC mode include surface-electrode driven EO flow[16], and travelling wave EO flow[17]. Common to these devices are that although the flow rates (measured in the unit $\mu L\ min^{-1}V^{-1}cm^{-2}$) are comparable to the above mentioned, their pressure capacities are low, typically only 1−10 PaV^{-1}. The main application of these devices is manipulation of suspended particles. However, AC driving signal still seems to be most promising due to its compatibility with the microfabrication process and convenient implement among these methods. More work need to be done in order to characterize the effect of the applied frequency and signal profile on the generated flow.

2.6.2 Issue II: High Driving Potential

Most electroosmotic pumps require high voltages to obtain enough flow rates and pressures, thus increasing the difficulty of integrating single stage pumps with complementary metal–oxide–semiconductor Integrated circuit (CMOS IC), and thus limiting their applications. Furthermore, the high voltage required sometimes produces an undesirable electrophoresis when the liquid is a mixture of many substances. To overcome this issue, Takamura *et al.*[11] proposed a cascade pump with 10-stage connections which could generate a pressure 25kPa at 10V. Chen *et al.*[9] characterized the performance of single stage, 2-stage and 3-stage electroosmotic pump, and found a 2-fold (~7MPa) and 3-fold (~10MPa) pressure of single stage (~3MPa) are generated in a 2-stage and 3-stage electroosmotic pumps respectively at the same driving voltage (5kV). So far, Most of the electroosmotic micropumps pertain to single stage pumps, which use one or several packed microchannels connected in parallel between the positive and grounding poles of the power supply. Little work had been done on multi-stage electroosmotic pumping. In these multi-stage electroosmotic pumps, we can observe reversed flow between stages as shown in Figure 2-5(a), due to the reverse electric field direction. In order to eliminate the reversed flow between stages, either the width of channel between stages has to be increased to induce less reversed pressure, or the length of channel between stages has to be increased to diminish the reversed electrical field strength. However, both methods increase the device footprint and complexity. Thus, this area remains to be explored.

2.7 Zeta Potential Modulation

In electroosmotic pumping, instead of the applied electrical potentials, the flow can be controlled with the modification of the surface charge at the solid/liquid interface. This can be achieved by both electrical and chemical means. Electronic control of the surface charge can be performed by embedding a gate electrode in the microchannel wall. The application of a gate potential will then modify the surface potential through capacitive coupling. Lee *et al.*[18] first introduced the zeta potential control inside a capillary by applying a gate voltage at the outer surface of the capillary. The thickness of the capillary wall was 100 mm, so the required gate voltage to obtain a distinct change in zeta potential was in the order of 10^3 V. Control of zeta potential at a relatively low gate voltage can be achieved by either reducing chemical ionization or enhancing the induced charge. Chemical ionization of surface silanol groups can be minimized by using a dilute solution[19] or a low pH buffer solution[20]. However, the utilization of low pH buffer restricts the applicability of this technique to acidic buffer only. This problem can be overcome, to some degree, by coating the channel wall. Hayes *et al.*[21] found that coating the capillary walls with large organo silanes could better control the local zeta potential, and that the technique could be used for a wide range of buffer pH. On the other hand, to maximize the effects of induced charge via externally applied gate voltage, a very thin channel wall (insulator or capacitor) is needed because the wall capacitance is inversely proportional to the thickness of the wall. Schasfoort *et al.*[22] were the first group to report field-effect control using a microchannel. They fabricated ultra-thin silicon nitride layers (390 nm), which exhibited a low gate voltage flow control (in the order of 10 V) in a silicon microchip.

2.8 Summary

Although the electroosmosis has been discovered for more than 200 years and the first electroosmotic pumping devices have been demonstrated more than 30 years ago, some critical issues involving electrolysis and electrical hazards haven’t been solved. The aim of this study was to develop an electroosmotic pumping method using zeta potential modulation, characterize it applications in pressure generation and particle transport.

Chapter 3 Principle of Rectified AC Electroosmotic Flow Using Zeta Potential Modulation

3.1 Zeta Potential Modulation

In electroosmotic pumping, the flow can be controlled with the modification of the surface charge at the solid/liquid interface. In this chapter, the method using zeta potential modulation to modify the surface charge will be further investigated.

3.1.1 Electrical Capacitor Model

The structures and methods of controlling the zeta potential at the solid/liquid interface have been developed since early 90's.[1] Here, outer surfaces of capillaries were coated with electrical conductive layers forming the electrodes (gate electrode) that could be used to modulate the charges on the interior surface of the capillaries. EOF was generated inside the capillary upon the application of driving potential across the capillary while the zeta potential at the inner surface of capillary can be modulated upon the application of gate potential at the outer surface and capillary wall itself acted as an electrical insulator. The insulator, the Stern and diffuse double layer can be described by capacitors as shown in Figure 3-1.

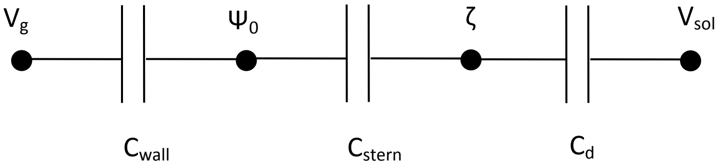

Figure 3-1 Capacitor model for zeta potential modulation

At moderate and low ionic concentrations, the potential drop over the Stern capacitance is negligible. In cases where the same frequency is used for the gate and channel potentials, the influence of the gate potential on the local zeta potential can be described by the formula below[23],

$$\Delta\zeta = \frac{C_{wall}}{C_d}\left[V_g - V_d\right] \tag{27}$$

where C_{wall} and C_d are the capacitance of the gate insulator and the diffuse double layer respectively, V_g and V_d are the amplitude of the applied gate and channel potential respectively, and $\Delta\zeta$ the induced difference in the zeta potential. The capacitance of the gate insulator, C_{wall}, is given by equation (28). Here A is the surface area, d_{wall} is the thickness of the insulator, and ε_0 and ε_r are the dielectric constant of vacuum and of the solution respectively.

$$C_{wall} = \frac{\varepsilon_0 \cdot \varepsilon_r . A}{d_{wall}} \tag{28}$$

The capacitance of the diffuse double layer, C_d, is given by equation 29[24]. Here λ is the Debye length, F is the Faraday constant, and R is the universal gas constant.

$$C_d = \left(\frac{\varepsilon_0 \varepsilon_r}{\lambda}\right) A\cosh\left(\frac{zF}{2RT}\zeta\right) \tag{29}$$

The operating principle of the zeta potential modulation in EOF is schematically illustrated in Figure 3-2. Under a constant driving electric field across the channel (or capillary), the amplitude and direction of EOF can be modulated by varying the local zeta potential which can be controlled by the potential applied on the gate electrode. Figure 3-2, case (a) describes the condition when no gate potential is applied. The EOF velocity is fixed and is dependent on the static zeta potential (negative in this case) at the surface. Case (b) describes the condition when this native negative zeta potential is further increased upon application of a negative potential at the gate electrode. This leads to additional accumulation of positive charges on the solution side of the double layer, thereby increasing the EOF velocity. Conversely, in case (c), application of a positive potential at the gate electrodes leads to neutralization of some of the native charge on the surface thereby leading to reduced amount of charge reflected in the solution side of the double layer. In some instances when the applied gate potential is large, this may lead to reversal of charge in the solution side of the double layer leading to reversal of EOF direction.

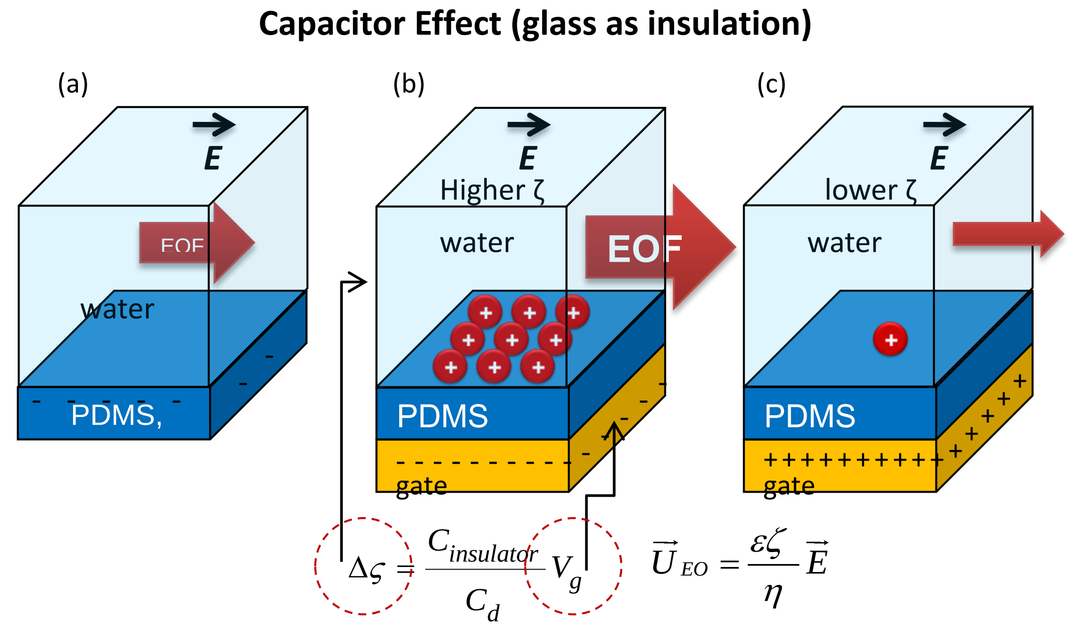

Figure 3-2 Illustration of the zeta potential modulation in EOF (a) original EOF without zeta potential modulation; (b) Faster EOF when the zeta potential is enhanced by a negative potential applied on the gate electrode; (c) reversed EOF when the polarity of zeta potential is reversed by a positive potential applied on the gate electrode.

3.2 AC EOF with the Zeta Potential Modulation

The application of alternating current (AC) potentials offers the advantage of electrolysis suppression. The EOF velocity obtained by the application of an AC electric field can be expressed as

$$U_{EO} = \frac{\varepsilon \cdot \zeta_0}{\eta} \frac{V_d}{L} \cdot \sin(\omega t) \tag{30}$$

When the zeta potential is not modulated using the gate electrode, the net velocity and therefore the net flow over one cycle of a symmetrical alternating signal is zero. However, when the local zeta potential is modulated with the same frequency as the driving potentials, the zeta potential is no longer static and modulates in the same way as the driving potential. This produces an oscillating EOF that is rectified and results a net flow. The zeta potential modulation in the case that the gate and driving potentials have the same frequency ω with a phase lag Φ can be derived from equation (1) and expressed as

$$\Delta\zeta = \frac{c_{wall}}{c_d}\left[V_g \sin(\omega t) - V_d \sin(\omega t + \phi)\right] \tag{31}$$

The working principle of the rectified AC EOF is depicted in Figure 3-3. Here the zeta potential is modulated by synchronizing the potential of the gate electrode (gate potential) with the potential applied across the channel (driving potential)

Therefore during the first half cycle, as shown in Figure 3-3(a), the electric field created by the driving potential is toward the right and the gate potential is negative. The zeta potential of the channel walls close to the gate electrode is enhanced over its native state since more positive ions are attracted to the surface to balance the charges on the gate electrode. The EOF velocity in this half cycle is enhanced over the native state. During the second half cycle shown in Figure 3-3(b), the gate potential becomes positive, therefore a lesser number of positive ions than in the native state will be attracted to the surface which decreases the zeta potential and reduces the EOF velocity. When this positive gate potential is larger than a certain threshold potential, the negative counter ions near the surface can be completely replaced by positive ions which results in a positive zeta potential and reversal of electroosmotic flow. Since the driving electric field is also reversed at this stage, the electroosmotic flow (Equation 1) under an alternating electric field can be rectified by this mechanism, while it would have a net-zero flow rate without the synchronization of the zeta potential modulation.

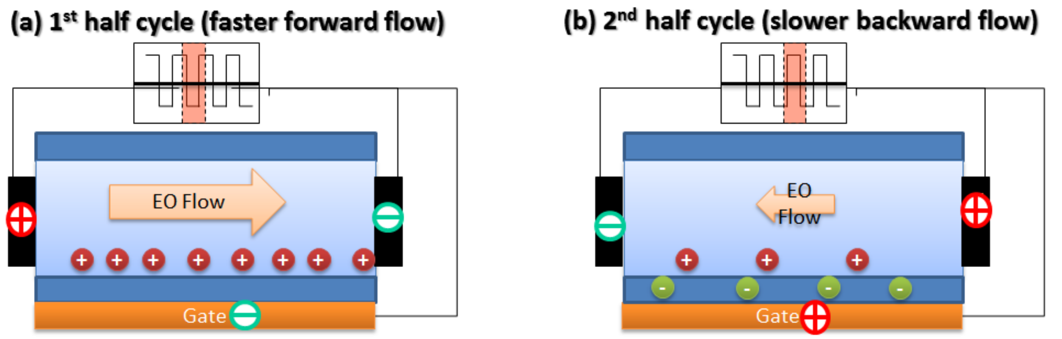
(a) 1st half cycle (faster forward flow)

(b) 2nd half cycle (slower backward flow)

Figure 3-3 Schematic of the rectified AC EOF using zeta potential modulation. (a) At the 1st half cycle, the electroosmotic flow velocity is enhanced over the native state due to the accumulating positive ions near the surface when a positive driving potential and a negative gate potential are applied. (b) At the 2nd half cycle, the electroosmotic flow is reduced or even reversed due to the accumulating negative ions near the surface when a negative driving potential and a positive gate potential are applied.

When the gate potential is synchronized with the driving potential, the modulated EO velocity can be expressed as

$$U_{EO} = \frac{\varepsilon}{\eta}\zeta_0 \frac{V_d}{L} \cdot \sin(\omega t) + \frac{\varepsilon}{\eta}\frac{C_{PDMS}}{C_d} V_g \frac{V_d}{L} \cdot \sin^2(\omega t) \tag{32}$$

Generally, AC driven flow will result in a zero net flow rate. However, when the zeta potential can be modulated and synchronized with channel axial potential, gas evolution due to electrolysis at the electrodes that provide the axial electric field is suppressed, while a net EOF flow is generated.

3.3 Validation using Microfluidic Device

To prove the concept of zeta potential modulation, an electroosmotic microfluidic device is designed and fabricated as shown in Figure 3-4. The device consists of two parts - the gate electrode substrate and the microfluidic channel. The gate electrode substrate is built from a Pyrex glass with coated Cr/Au layers which is covered with 10μm thick spin-coated PDMS as an insulating layer. The microfluidic channel is obtained through PDMS soft-lithography process using SU-8 moulds. The mould master is silanized with trimethylchlorosilane vapour which can make the master surface more hydrophilic and consequently facilitate the PDMS peeling process afterward. The channel dimension is 200μm in width, 80μm in height, and 20mm in length. Holes are punched through PDMS in order to attach PTFE tubing (ID0.032"/OD0.056") for the inlet and outlet. After surface activation in 80W oxygen plasma for 1 minute, the microfluidic channel is bonded to the gate electrode substrate. Two platinum wires with 250μm diameter are inserted into the PTFE tubing as the driving electrodes as shown in Figure 3-4(f). Experiments were performed with 0.1mM PBS, DI water, and methanol as the working fluid, and flow velocity is measured by tracking the movement of 1μm polystyrene beads under a microscope.

(a) SU-8 channel mold

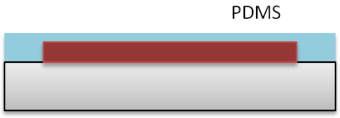

(b) PDMS casting

(c) Peel off PDMS channel

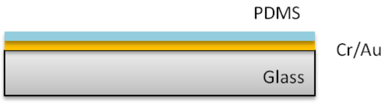

(d) spin-coated PDMS over gate

(e) Microchannel integration

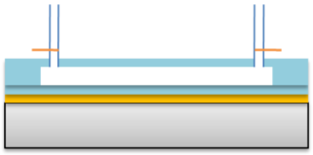

(f) Tubing and insert driving

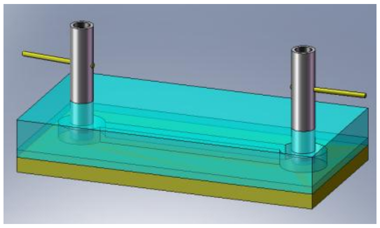

(g) Schematic overview

Figure 3-4 Process flow and schematic overview

3.4 Electroosmotic Mobility in PDMS Microfluidic Channels

To determine the proper working fluid for electroosmotic flow, the electroosmotic mobility of methanol, DI water (20MOhm), and 0.1mM Phosphate Buffer Solution (PBS) is measured in PDMS microfluidic channel by tracking neutral 1μm-polystyrene beads (Kisker, Germany) under microscope. The channels are filled with methanol, DI water, and 0.1mM PBS individually. Two platinum wires are then inserted in inlet and outlet as the driving electrodes. The electroosmotic velocity is then determined from the beads movement under different driving voltage. The results are shown in Figure 3-5 (no error bar due to single measurement for each data point). The slopes in Figure 3-5 represent for the electroosmotic mobility of $1\times10^{-8}m^2/Vs$ for methanol, $5\times10^{-8}m^2/Vs$ for DI water, and $2\times10^{-8}m^2/Vs$ for 0.1mM PBS in PDMS microchannels.

The concentration dependence of electroosmotic flow can be observed by comparing the trend lines of DI water and 0.1mM PBS. It can be seen that the EOF mobility is smaller for 0.1 mM PBS solution as compared with DI water. This is because of the higher concentration of ions present in the buffer solution. When more counter-ions are available to screen the surface charge, the EDL thickness will decrease which leads to a lower zeta potential, thus results in a slower EOF for 0.1mM PBS. The relation between the surface potential and the electrolyte concentration shows a decrease in zeta potential with the square root of the concentration. During measurement, severe bubble generation has been observed in the microchannel filled with 0.1 mM PBS when driving voltage is larger than 400V. This could be caused by the lower electrical resistance of PBS.

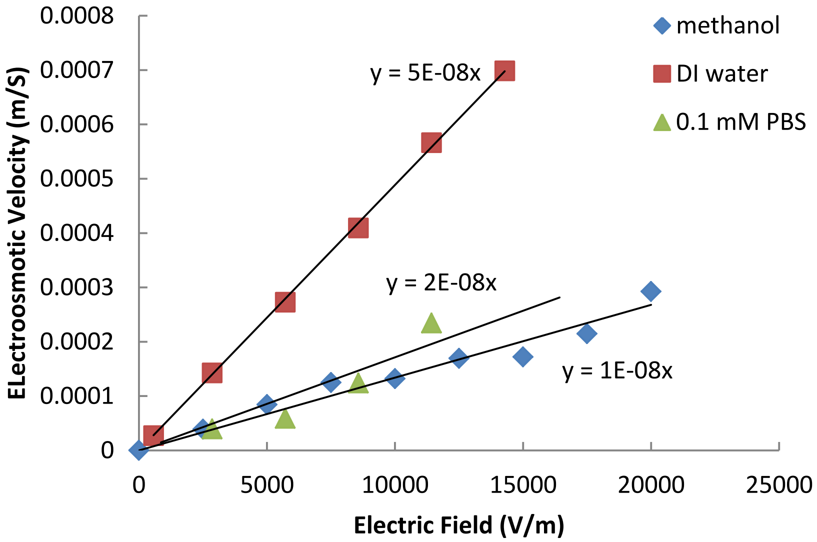

Figure 3-5 Comparison of EO flow velocity with electric field in methanol, DI water and 0.1mM PBS

3.5 Zeta Potential Modulation in PDMS Microfluidic Channels

To observe the effect of zeta potential modulation on flow velocity, the gate electrode is connected to one of the driving electrode, and the other driving electrode is grounded as shown in Figure 3-6. Figure 3-7 shows the observed EOF velocity as the peak driving voltage is varied from -500 to 500 V. It can be seen that the velocity increases as the peak voltage is increased as expected. In addition, the slope of the velocity increase is larger for positive voltages as compared to the negative voltages. This can be explained using equation 6. The 2nd term in equation (6) introduces asymmetry in EO velocity vs. gate voltage as seen in Figure 3-6, by shifting the curve up (blue curve: zeta potential modulation ON; red curve: OFF) and thereby achieving flow rectification. The EO mobility extracted from Figure 3-6 is shown in Figure 3-7 demonstrates a twofold modulation when a 500V gate voltage is applied. The slope in Figure 3-7 corresponds to the coefficient $(\varepsilon C_{PDMS})/(\eta C_d)$ in equation (6) which represents the effectiveness of gate potential on the EO mobility.

.

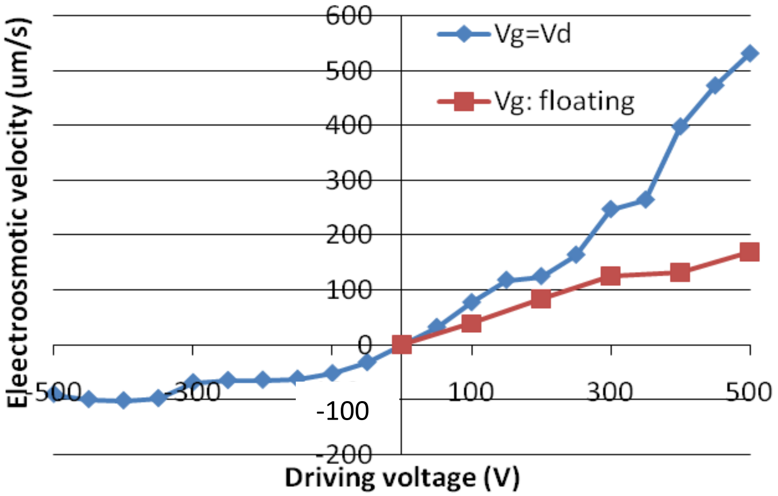

Figure 3-6 Rectification of EO velocity as gate is synchronized to driving voltage

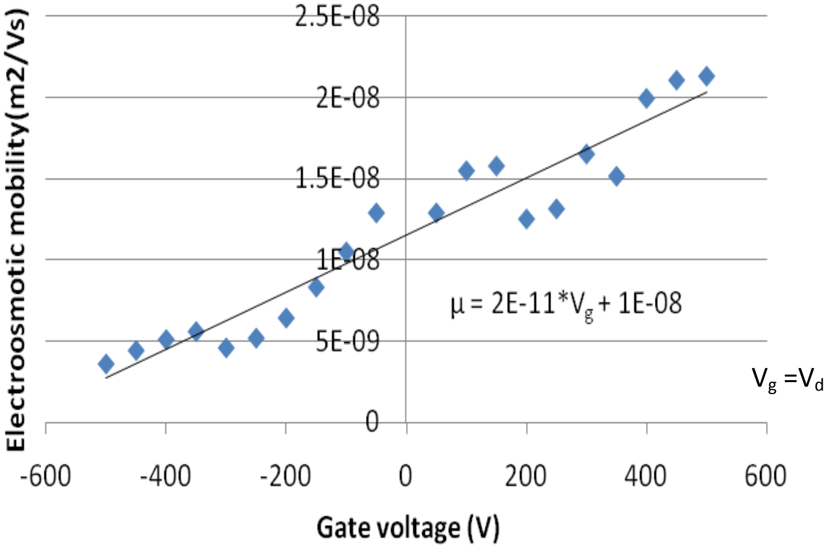

Figure 3-7 Mobility obtained at various gate voltages with synchronization

The particle tracking technique used above is only suitable for low working frequency (~1Hz) because of the recording frame rate of the camera is 30 fps only. However operating at a higher working frequency can avoid electrolysis and bubble generation over longer period of time. In the case of high working frequency, only the net displacement of the beads can be observed simply because the beads oscillate too fast to be captured. A different approach is adopted to analyze the experimental results. The net velocity of rectified EOF (U_{EO}) in an symmetry AC electric field can be expressed as the sum of the velocity in the positive half cycle (U_{EO}^{+}) and the velocity in the negative half cycle (U_{EO}^{-}) as equation (7).

$$U_{EO} = U_{EO}^{+} + U_{EO}^{-} \tag{33}$$

When the gate electrode is floating, U_{EO}^{+} should be equal to $-U_{EO}^{-}$, therefore the net velocity U_{EO} is zero. However, when the gate electrode is synchronized, the magnitude of U_{EO}^{+} and U_{EO}^{-} are not equal anymore, thus generate the rectified EOF. Therefore, the net velocity of the beads extracted from the recording frames can be used to calculate the variation of electroosmotic mobility $\Delta\mu_{EO}$.

$$U_{EO} = \mu_{EO}^{+}E^{+} + \mu_{EO}^{-}E^{-} = (\mu_{EO}^{+} - \mu_{EO}^{-})E = \Delta\mu_{EO}E \qquad (E^{+} = -E^{-} = E) \tag{34}$$

shows the variation of electroosmotic mobility at various gate voltages for methanol and DI water. As mentioned in the previous section, organic liquids should have larger variations in electroosmotic mobility (or zeta potential) under the gate voltage effect, since the effect of the gate voltage on the EOF scales inversely proportional to the dielectric constant of the solution which now can be verified from Equation (5). Table 3-1 lists the properties of some common working liquids for electroosmotic flow. Because of the low dielectric constant, organic working liquids should be able to demonstrate the effect of gate voltage effect better and also generate more AC rectified EOF. Although acetone has the lowest dielectric constant, it is not compatible with PDMS microfluidic device since acetone causes swelling and detachment in PDMS[25]. The reason of only two data points for DI water in is the polystyrene beads tend to stick to the surface of PDMS channel, thus causes some difficulties in measurement.

Working liquid	**Dielectric constant**	**EO mobility (m^2/Vs)** **(experimental results)**
0.1mM PBS	78.4	2×10^{-8}
DI water	78.4	5×10^{-8}
Methanol	32.7	1×10^{-8}
Acetone	20.6	--------

Table 3-1 Properties of working liquids

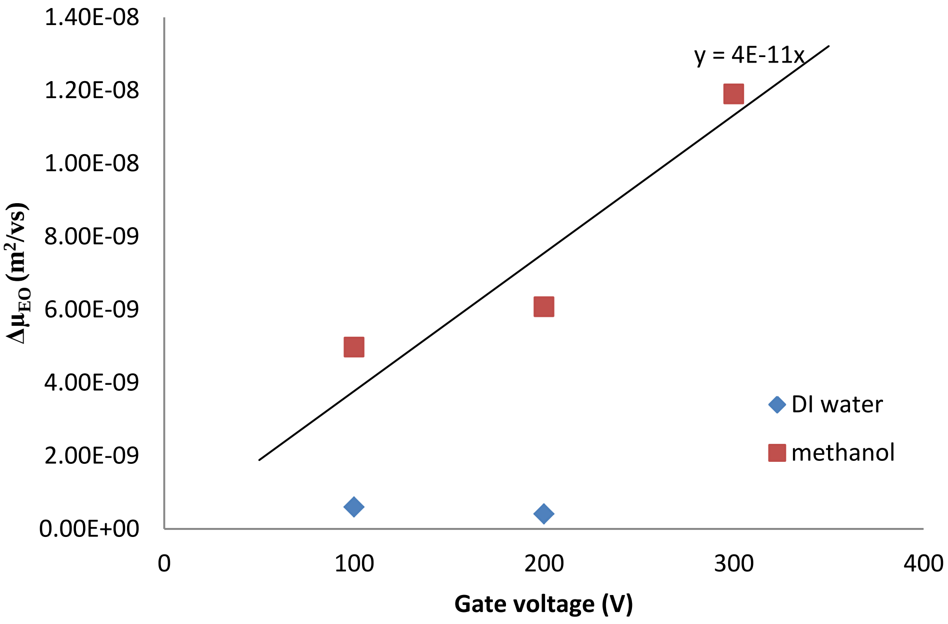

Figure 3-8 Variation of electroosmotic mobility at various gate voltages

3.6 Summary

The method using zeta potential modulation to modify the electroosmotic mobility is introduced. Based on this method, the AC EOF can be rectified theoretically by synchronizing the gate potential with the driving potential. A PDMS-based microfluidic device is designed and developed to investigate this effect and the experimental results prove that the electroosmotic mobility can be effectively modified using a potential applied on the gate electrode. This modified electroosmotic mobility can be used to rectify the oscillating flow in AC EOFs that will be investigated and demonstrated in the following chapters. However, the measurement method used here by tracking the particle movement is limited to flows with very low frequencies (<1 Hz). Since the flow induced by the alternating electric field with high frequency is unsteady, it is critical to visualize the flow with high spatial and temporal resolutions in order to understand the fluid dynamics.

Chapter 4 Measurement of Periodic Flow Using Micro Particle Image Velocimetry with Phase Sampling Technique

This chapter is a reproduction of the following article to be submitted to Journal of Experiments in Fluids. A method to obtain high temporal resolution for high frequency periodic electrokinetic flows using phase sampling technique in micro particle image velocimetry (PIV) measurements are developed in order to characterize the AC electroosmotic flows. In this technique, the flow characteristics over a single cycle can be reconstructed from these unique points obtained over larger timeframe spanning a number of cycles, thus allowing measurement at higher temporal resolutions. Without upgrading to the costly high-speed equipment, this technique can be used to measure the flow variation of forced periodic flows and characterize their flow responses that can be helpful to obtain the optimum performance by choosing proper operation conditions and device designs.

Authors: Wen-I Wu, Daniel Ewing, P. Ravi Selvaganapathy, and Chan Y. Ching

Publication Information: To be submitted

Submitted Date: To be determined

Measurement of Periodic Flow Using Micro Particle Image Velocimetry with Phase Sampling Technique

Wen-I Wu, Daniel Ewing, P. Ravi Selvaganapathy, and Chan Y. Ching
McMaster University, Canada

4.1 Abstract

This paper reports a phase-sampling method using conventional micro particle image velocimetry (PIV) for forced periodic flows. In this technique, each velocimetry data set from laser pulses represents a unique point in phase of a periodic flow. The flow characteristics over a single cycle can be reconstructed from these unique points obtained over larger timeframe spanning a number of cycles, thus allowing measurement at higher temporal resolutions. The flow measurements were performed for AC electroosmotic flows with a high operation frequency (> laser pulse repetition-rate) using phase-sampling and verified with results from phase-locking technique. Although the temporal resolution is limited by the shortest camera exposure time and the time separation between laser pulses, the theoretical sampling resolution can be as low as 20 µs for 100Hz periodic flows with sufficient number of dataset, and a resolution of 200 µs was obtained in the experiment using 40 sets of velocimetry results that only took <10 sec for laser to collect the results.

4.2 Introduction

Microfluidics is the science and technology of flows in the microscale and their control. It has found widespread applications in chemical and biochemical analysis due to various advantages stemming from miniaturization and integration, such as faster analysis, higher efficiency, portability and low reagent consumption[26]. Flows in the microscale are usually laminar and simpler to analyse as compared to their macroscale counterparts. Nevertheless, various unusual phenomena dominate in the microscale, due to high interface surface to volume ratio, that is not evident in the macroscale. Understanding and control of these dominant phenomena is the optimal way to control fluid transport in the microscale. Surface charge and surface forces have been exploited over the past decade to control fluid motion. They have spawned new areas of research, namely, electrokinetics[27] and electrowetting[28] that have many applications in microfluidics.

Electrokinetic phenomenon, deals with fluid flow through the application of an electric field. Any polar fluid in contact with a solid surface such as the walls of a microchannel, produces a separation of charge across the interface called an electrical double layer.

Application of an electric field parallel to the double layer produces a body force on the charges and moves the charges in the fluid along the direction of the electric field. This movement of the fluid layer close to the wall causes viscous drag on the rest of the fluid causing bulk motion of the fluid. As the charges are generated at the surface, the electrokinetic phenomena are dominant in the microscale where the surface to volume ratio is high. Most applications[27,29,30] using electrokinetic flows are operated by applying a constant electric field (DC mode) and they produce constant velocity profiles at steady state. More recently, alternating[15,31–36] electric fields have been used in order to avoid bubble generation and joule heating[13,15,37] which have been major impediments for DC electrokinetics. Pulsed DC electric fields had also been found to enhance the electrophoretic separation by control of the rise time of the electroosmotic flow[38]. Under an unsteady applied electric field, the body force produced and therefore the flow induced is also unsteady but periodic. In order to study the fluid dynamics under such conditions and understand the causal effects between the electric field, body force and the flow field, it is critical to measure the flow field with high spatial and temporal resolutions.

Currently there are various velocimetry methods including particle image velocimetry (PIV)[39–42], particle tracking velocimetry (PTV)[43,44], Molecular tagging velocimetry[45], laser interferometry[46], ultrasonic Doppler sensors[47] and thermal pulse sensors[48] to measure the flow velocity. Among them, only PIV and PTV can produce two or three dimensional vector fields and measure fluid motion with length scales ranging from 10^{-4} to 10^{-7} m due to their ease of integration with microscopy. PTV typically tracks single or few particles within the nearest neighbour while PIV uses cross-correlation techniques with high particle densities to determine the particle displacement within an image pair. The avoidance of Brownian motion with high seeding density makes PIV methods more desirable for microscale and nano scale fluid mechanics[49]. In PIV, the fluid is seeded with tiny fluorescent particles which are carried with the flow and the position of these particles over the entire flow field is imaged in quick succession. Correlation between the position of the particles and their changes between the two successive images provide the local velocity field. Since PIV methods use an ensemble-averaged correlation to obtain accurate results and the region of interest is in the micrometer scale, short time intervals between two images is necessary. To realize short time intervals, double pulse lasers are synchronized with the PIV camera. Thus, a typical micro PIV system consists of a double pulse laser, a CCD camera, a timing controller, an epi-fluorescent microscope, objective lens, colour filters and associated optics. In such conventional micro-PIV systems, the highest temporal resolution is in the range of 100-300ms and is limited by the frame rate of CCD camera which are typically 4-10 frames per second (FPS) as well as its sensitivity in detecting low fluorescence. Electrokinetic flows operated under pulsed DC and AC potentials can require a temporal resolution of tens of miliseconds or lower. The spatial root-mean-square (RMS) velocity of an oscillating flow can be measured using convectional PIV; however, the measurement of the time evolution of the velocity field can be challenging using such a system.

Several techniques, such as the use of high speed cameras and continuous-wave lasers[50], phase-locking techniques[51–54] and laser-induced fluorescence photobleach anemometering (LIFPA)[55], have been developed to improve the temporal resolutions. High-speed equipment however is not easily accessible due to its relatively high cost. LIFPA, while providing a temporal resolution in the 5-10µs range, cannot provide velocity field information. Phase-locking techniques that synchronize the laser pulses with the triggering signals of electrokinetic flows will allow the measurement of transient flows such as acoustic streaming velocities and transient electroosmotic flow under an applied DC potential. However, the process is complicated. For example, the velocity field at a specific time t_1 after the flow has be initiated can be acquired by setting the delay time between the triggering signals for electrokinetic flows and the laser pulses as t_1. To obtain data at different times in the transient, the systems have to be reset and the measurement repeated for a second time t_2. Thus, while a phase-locking technique can improve the temporal resolution, it is a tedious, multi-experiment methodology. A temporal resolution of 500 µs has been reported using high speed equipment[50] and phase-locking technique[51] and is constrained by the shortest camera exposure time.

The objective of this study was to develop a novel phase-sampling technique to obtain such temporal resolution measurements using a conventional micro PIV system. Thus method differs from previous methods in that it does not require either precise synchronization control or elaborate procedures while providing accurate measurement capability and high sampling resolution. Moreover this technique can be extended to any forced periodic flow triggered by external signals such as AC electroosmotic flows.

4.3 Methods

A PIV system generally uses a set of two laser pulses with a known time separation ΔT between their firing, to illuminate florescent particles in the fluid that act as flow tracers. The fluorescing particles are excited at a specific wavelength of the laser and emitted at another wavelength that is acquired by image sensors to avoid interference. The camera synchronized with laser pulses captures the images and the displacement of the particles between the two images are computed by cross-correlation within an interrogation area. The velocity field can be obtained from the displacement and the given time separation ΔT. Most PIV systems have high spatial resolution, but low temporal resolution and are more suited for measuring steady state flows.

The phase-sampling technique developed in this study is used to measure velocity fields at arbitrary phases. The main criterion that determines whether this technique can be used is that the flow characteristics of the periodic flows should be highly repeatable. Rather than obtaining the velocity field for multiple time instances over a single cycle, a single dataset of the velocity field along with its timestamp is obtained per cycle. By mismatching the frequency of sampling (laser repetition rate) and the periodic flow (external driving frequency) as shown in Figure 4-1 velocity field datasets from subsequent cycles that represent a unique phase of the periodic flow can be obtained. When repeated for a number of cycles, a high temporal resolution velocity field for a single cycle can be reconstructed.

Consider the pair of laser pulses at a laser repetition rate or repeating at a frequency of f_L shown in Figure 4-1(c). The external driving voltage in this instance is an AC signal with a frequency of f_D and it is assumed to start at time t = 0 as shown in Figure 4-1(a). Figure 4-1(b) represents the flow response upon the application of the AC signal. The velocity field V_1 from the first pair of laser pulses is captured at time t_1 which can be arbitrary and is the initial time delay between the driving potential signal which initiates the fluid movement and the image capture. The velocity field V_2 obtained from the second pair of laser pulses is at time t_2 which is equal to $t_1+(1/f_L)$. Since the objective is to reconstruct velocity field in a single cycle, certain number of period m need to be subtracted to reveal its equivalent phase in a single cycle. The equivalent phase of the flow is given by $\varphi_1 = 2\pi\cdot[t_1-m\cdot(1/f_D)]/(1/f_D)$ with m= 3, and at time t_2 is $\varphi_2 =2\pi\cdot[t_2-m\cdot(1/f_D)]/(1/f_D)$ with m= 6 which is equal to $2\pi\cdot[(t_1+1/f_L)-6\cdot(1/f_D)]/(1/f_D)$. Therefore, the equivalent phase φ_n for a given timing t_n can be expressed as

$$\begin{aligned}\phi_n &= \frac{2\pi[(t_1+\frac{n-1}{f_L})-m\cdot\frac{1}{f_D}]}{\frac{1}{f_D}} \\ &= 2\pi[f_D\cdot(t_1+\frac{n-1}{f_L})]-2\pi\cdot m\end{aligned} \tag{1}$$

where m is chosen so that φ_n falls between 0 and 2π. Each velocimetry dataset from the laser pulses would represent a unique point in phase for a periodic flow. By simply extending the measurement duration without suspending the experiment or resetting the laser, the velocity field at various phase locations can be obtained to reconstruct the flow characteristics over one cycle of the periodic flow.

The temporal resolution using the phase-sampling technique would depend on the measurement duration and the frequency mismatch between laser repetition and driving voltage. For high frequency periodic flows, the frequency of the external driving voltage f_D is typically higher than the frequency of laser pulse f_L. When velocity data sets are collected under the condition, $f_D = N \cdot f_L$, it is essentially similar to the phase-locking technique and each measurement corresponds to the same phase. However, when $f_D \neq N \cdot f_L$, each measurement will represent an unique and different phase, thereby increasing the temporal resolution of the measurement, and is referred to here as phase sampling. Theoretically, the highest sampling resolution (SR) using this technique can be expressed as

$$\begin{aligned} &SR = \frac{1}{f_D \cdot X} \text{second} \\ &\text{where } \mathrm{X} = \text{denominator of the lowest reduced term} \left(\frac{f_D}{f_L} \right) \end{aligned} \tag{2}$$

For a measurement with f_L = 4.83 Hz and f_D = 100 Hz, the denominator X equals to 483 and the highest temporal resolution is 1/48300 second (20.7 µs). For example, the data at times t= 1/4.83, 2/4.83, 3/4.83, 4/4.83 will correspond to (340/48300), (197/48300), (54/48300), (394/48300) in a single cycle with a period of (483/48300) s. A serial of dataset with an interval of 1/48300 s can be obtained by simply extending the sampling duration and results in a sampling resolution of 20 µs.

4.3.1 Experimental Methods

The micro PIV system from TSI Inc. (Shoreview, Minnesota) is used in this study and consists of a double pulsed Nd:YAG laser with a repetition rate f_L= 4.83 Hz. The working fluid was seeded with 1.0 µm diameter polystyrene fluorescent beads (Invitrogen) that had an excitation wavelength of 540 nm and emission wavelength of 560 nm. The test solution was deionized water with a seeding density of 2 × 10^9 beads/mL. A digital 1.4 megapixel CCD camera (TSI PIVCAM 14-10) with a resolution of 1376 × 1040 pixels, pixel size of 6.45 µm and frame rate of 10 FPS was used to image the flow. A 20X objective lens is used and results in a 0.7 mm × 0.5 mm field of view. A synchronizer (TSI LASERPULSE™ 610034) automates the control of the timing between laser pulses, camera and camera interfaces during system set-up and image acquisition. Figure 4-2 shows the schematic of the experimental setup. We demonstrate the application of the phase-sampling technique in measuring velocity profiles for AC electrokinetic (EK) flows that are increasingly used due to reduced voltages and minimal electrolysis, as compared to DC EK flows. The AC electroosmotic flow is obtained by applying a 200V AC potential across the microfluidic channel. The driving voltage for the AC electroosmotic flows was generated from a function generator (Tektronix AFG3022B), amplified through a power amplifier (Trek 677B, gain= 200, slew rate >15 V/µs) and connected to the driving electrodes. A 12-bit, 10,000 sample-per-second (S/s) analog-to-digital (A/D) converter (National Instruments USB-6008) is used to record the driving signals and laser pulses that are time-stamped. Each velocity field dataset is phase-mapped in a Matlab® program using the algorithm shown in Eq. (1) with reference to the driving signal and the procedure shown in Figure 4-2 (b) to convert the velocimetry dataset into average velocity. The test conditions are summarized in Table 4-1.

The microfluidic device for testing was fabricated using an Pyrex glass substrate with spin-coated PDMS (12µm) on top to provide uniform electroosmotic mobility distribution in the microfluidic channels. The spin-coated PDMS was prepared by mixing a 10:1 ratio of PDMS prepolymer/curing agent (Sylgard 184, Dow Corning) mixture with hexane (3:1 weight ratio). The mixture was dispensed on top of the glass substrate and spun at 7000 rpm for 30 sec, resulting in a PDMS film of 12 µm thickness. After that, the PDMS film is cured at 85 °C for 4 min. The PDMS channel (L 10 mm×W 450 µm×H 100 µm) was fabricated using soft-lithography process on a SU-8 mould with the integrated interconnect[56] (ϕ3 mm Silicon tubing, Cole Parmer) and then bonded to the PDMS-coated glass substrate after surface activation with oxygen plasma at 60 W for 1 min. Two Ø250µm Platinum wires are inserted into the reservoirs and used as driving electrodes.

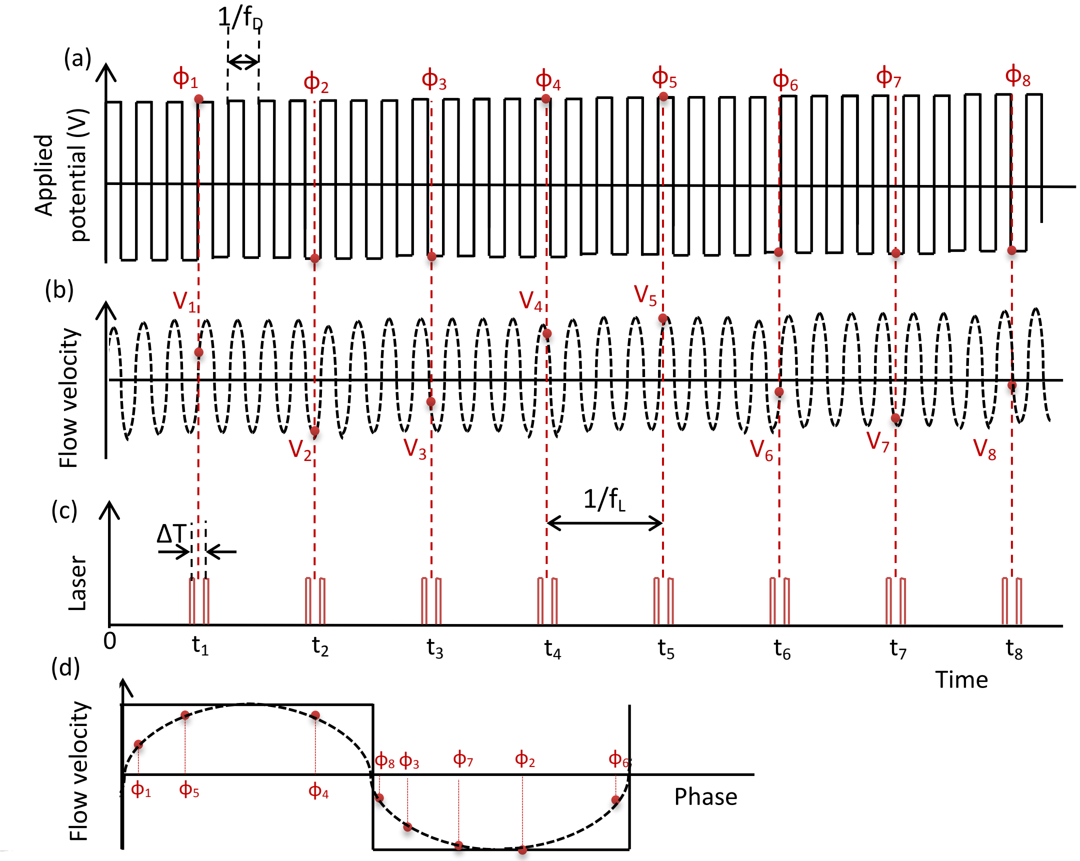

Figure 4-1 Schematic illustration of the phase sampling technique. (a) Timing diagram of the driving potential with a frequency of f_D; (b) timing diagram of the flow response under the driving potential; (c) timing diagram of the laser pulses with a frequency of f_L to obtain the flow velocity datasets at different times; (d) the reconstructed flow velocity within a single cycle.

Table 4-1 ***Experimental conditions for the phase sampling technique***

Pulse repetition rate	4.83 Hz
ΔT between pulses	500 µs to 2 ms
Exposure	500 µs
No. of pulse	40
Bead	1 µm polystyrene
Channel dimension	L10 mmxW450 µm xH100 µm

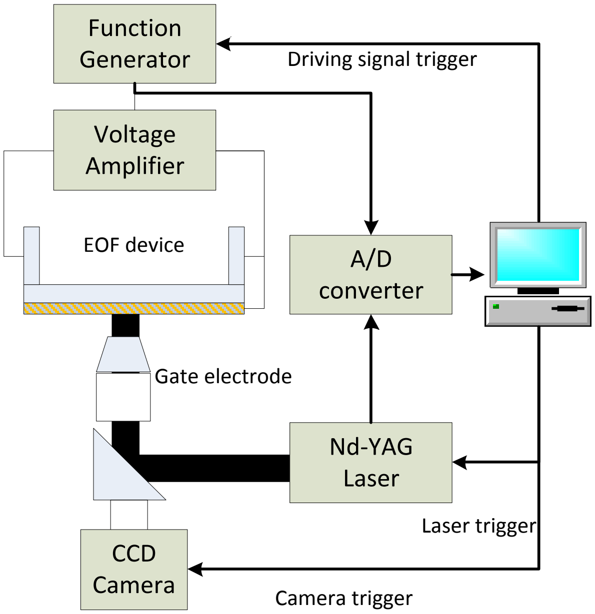

Figure 4-2 ***Schematic illustration of) the setup using phase-sampling technique in micro PIV systems***

4.4 Results and Discussion

When an electrical potential is applied across the microchannel, the order of the response time of the electroosmotic flow to reach steady state can be estimated as[57]

$$\tau_{EO} = O(D_h^2 \rho / \mu) \tag{3}$$

where D_h is the hydraulic diameter of the microchannel, ρ and μ are the solution density and viscosity. For DI water and hydraulic diameter of 100 μm, the estimated response time is in the order of 10^{-2} s. This response time imposes the highest frequency of the fully developed AC electroosmotic flow to be 100Hz in this microfluidic channel. Resolving such frequencies is a challenge for conventional micro-PIV due to its low temporal resolution. The phase-sampling technique developed in this study is able to measure the time evolution of the AC electroosmotic flows.

The average velocity profiles of the EOF for different times under a 200V 10Hz sinusoidal signal are shown in Figure 4-3(b). The velocity is averaged in the y direction over the interrogation area (Figure 4-3(a)). Some bad vectors shown in Figure 4-3(a) were caused by polystyrene fluorescent beads that were stuck on the bottom PDMS surface and gradually became background noise[58]. For all times, the velocity profile is nearly uniform across the entire channel width. The time evolution of the EOF for an applied sinusoidal signal with 200V using the phase-sampling technique is shown in Figure 4-4 for applied frequencies of10 Hz, 50Hz and 100 Hz. The velocity of the fluid is seen to closely follow the electrical signal without any delay. The velocity U_{EO} can be expressed by the product of electroosmotic mobility μ_{EO} and the sinusoidal electric field E and given by the Helmholtz-Smoluchowski (HS) formula:

$$\overrightarrow{U_{EO}}(t) = \mu_{EO}\vec{E}(t) = \frac{\varepsilon\xi}{\eta}E_0 \cdot \sin(2\pi \cdot f_D \cdot t) \tag{4}$$

where ζ is the zeta potential, ε is the permittivity, and η is the viscosity of the working liquid. The flow should remain in steady state when the applied frequency is less than the response time of the flow. The flow velocities in Figure 4-4 show a sinusoidal variation as the applied electric field. The results were compared with that from the phase-locking technique at phase φ = 45°, 90°, and 135°. There is a good agreement between the results from the phase-sampling and phase locking techniques at these phases. The phase sampling and phase locking technique can be used as complimentary methods. For instance, the phase-sampling can be used to obtain a fast scan for the entire flow field and subsequently the phase-locking can be followed up to investigate the flow in detail at a particular time or phase without starting from the beginning.

The effect of the time-averaging can be evaluated by considering the theoretical velocity signal at time t as

$$U_{Theoretical}(t) = U_{EO}(t) \tag{5}$$

The measured velocity using PIV at time t is the displacement over ΔT and can be expressed as

$$\begin{aligned} U_m &= \frac{1}{\Delta T}\int_{t-1/\Delta T}^{t+1/\Delta T}\frac{\varepsilon\xi}{\eta}\sin(2\pi \cdot f_D \cdot t)dt \\ &= [\frac{\sin(2\pi \cdot f_D \cdot \frac{\Delta T}{2})}{\pi \cdot f_D \cdot \Delta T}] \cdot \frac{\varepsilon\xi}{\eta}\sin(2\pi \cdot f_D \cdot t) \\ &= [\frac{\sin(2\pi \cdot f_D \cdot \frac{\Delta T}{2})}{\pi \cdot f_D \cdot \Delta T}] \cdot U_{Theoretical} \end{aligned} \tag{6}$$

The coefficient of $U_{Theoretical}$ in Eq. 6 represents the effect using PIV and it is 0.999, 0.984, and 0.935 for a driving frequency f_D of 10Hz, 50Hz and 100Hz respectively. Thus, the averaging feature in PIV causes 6.5% error in amplitude at 100Hz. The amplitude deviation from Eq. 6 are compared with the experimental values for three different driving frequency f_D in Figure 4-5. As the applied frequency increases, the amplitude of the flow velocity decreases as the induced error due to the time-averaging increases and the frequency approaches the limit of the response time.

Measurements were also performed using a square waveform driving potential to investigate the capability of this technique in measuring transient flows. Due to the step change in voltage, there will be a transient period for the flow at each step change. The velocity profiles of the EOF at different times under a 10Hz square-waveform signal with 200V amplitude using the phase-sampling technique is shown in Figure 4-6. Upon the application of the electric field, the EOF first occurs near the boundary while the bulk fluid at center is nearly stationary as shown in cases of 6.5° (1.8ms) and 183.6° (51ms). The profile becomes plug-like once it reaches steady state. The time evolution of the EOF flow is shown in Figure 4-7 and compared with the results from the phase-locking technique. The velocity of the fluid is seen to closely follow the electrical signal. However the transient phenomena such as the rising and falling regions appear as the frequency increases. Rise times (from 10% to 90% of the step height) of less than 5 ms, 2 ms and 1.5 ms for 10 Hz, 50 Hz and 100 Hz respectively are observed which match the theoretical prediction (10^{-2} s). There is a good agreement between the two measurement techniques. Under steady state, the measured velocity using PIV would have no time-averaging effect. This is satisfied for the condition

$$U_m = U_{Theoretical} \text{ when } \Delta T < t < \frac{1}{2f_D} - \Delta T \text{ and } \frac{1}{2f_D} + \Delta T < t < \frac{1}{f_D} - \Delta T \qquad (7)$$

However in the transient, the measured velocity at time t can be expressed as

$$U_m = \frac{{}^{\varepsilon\xi}\!/_{\eta}\,\cdot}{\Delta T} E_0 \cdot (t - \frac{1}{2f_D}) \text{ when } \frac{1}{2f_D} - \Delta T < t < \frac{1}{2f_D} + \Delta T \qquad (8)$$

Therefore, the profiles during transients would be distorted slightly because of the time-averaging method. The amplitude variation of theoretical prediction using Eq. 7 and experimental results are plotted against the driving frequency f_D in Figure 4-5. As the frequency increases and approaches 100 Hz (corresponding to the response time of the fluid), the amplitude of the EOF decreased. The variation of the flow velocity with phase takes a sigmoidal shape within the transient region indicating that the flow is not able to respond to the alternate electric fields under a high frequency. Moreover, the transient phase between the steady flows is also clearly observed.

As the transient happens within the order of 10^{-2} *s*, this experiment clearly demonstrates the high temporal resolution of this technique which is not possible in conventional micro PIV systems. A sampling resolution of 0.2 ms can be found in the cases of 100 Hz shown in Figure 4-4(c) and Figure 4-7(c) by using 40 sets of results and having the laser repetition rate f_L of 4.83 Hz and the driving frequency f_D of 100 Hz. A theoretical sampling resolution of 20 µs as calculated in Eq. 3 can be obtained by simply extending the experiment duration in order to collect sufficient datasets for the phase-sampling algorithm to process although in practice the highest sampling resolution depends on the shortest camera exposure time and the time separation between laser pulses.

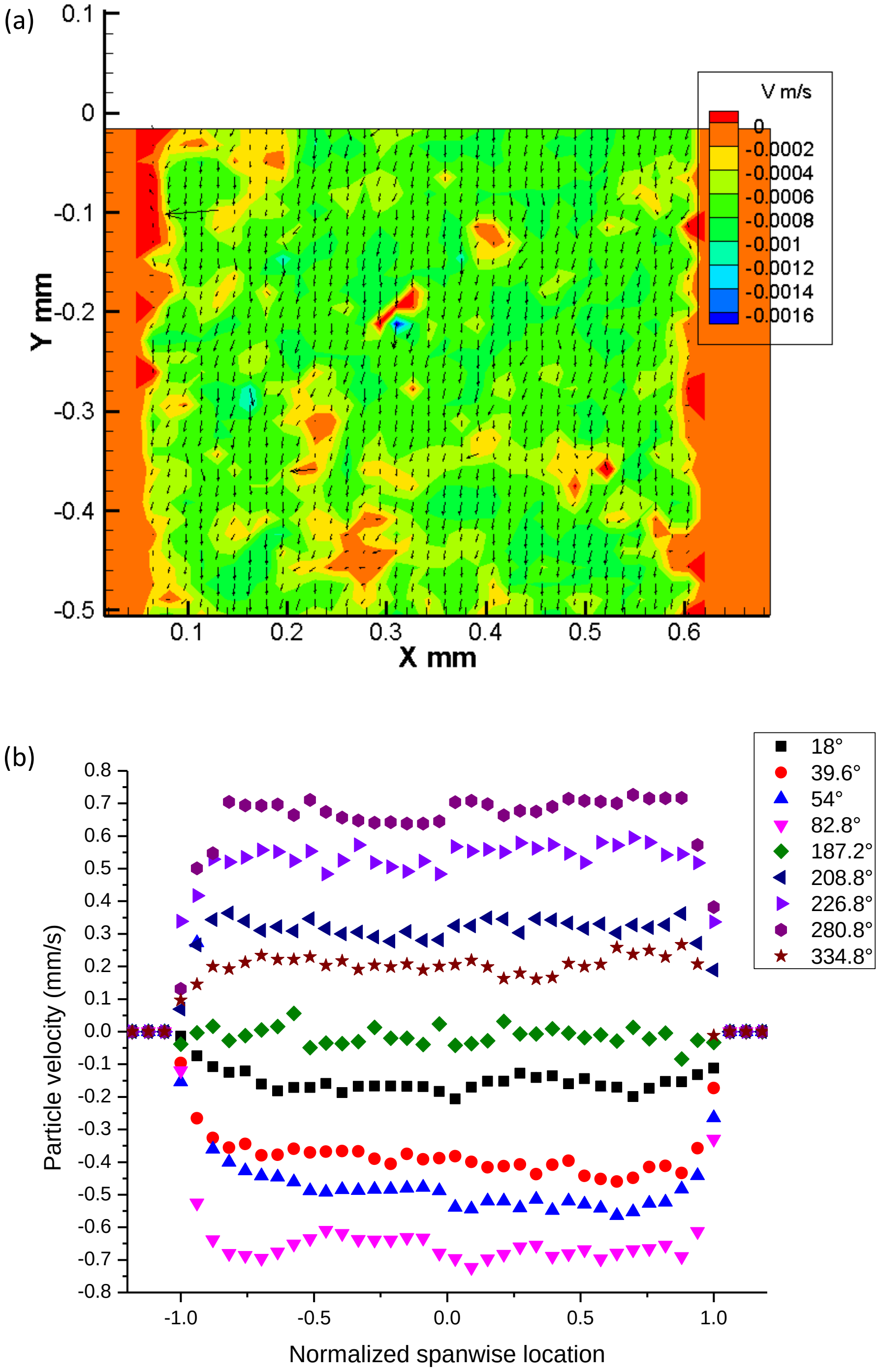

Figure 4-3 ***(a) Representative velocity vector field in the interrogation area at t= 23ms; (b) Velocity profiles at different times of the electroosmotic flow when a 10Hz sinusoidal signal with 200V amplitude is applied across the microfluidic channel.***

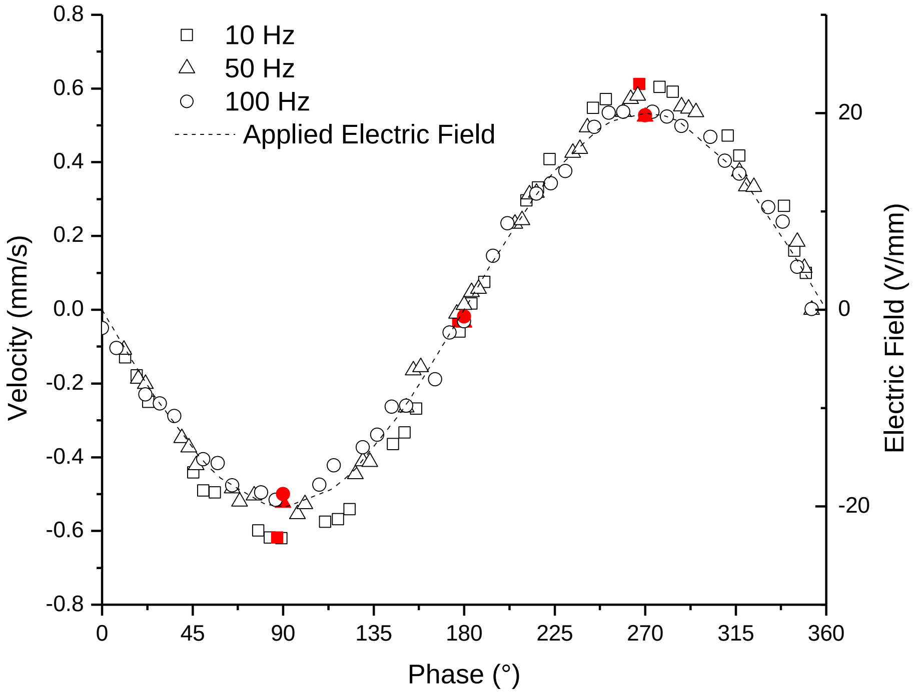

Figure 4-4 The sinusoidal flow variation using phase sampling technique under various frequencies when 200V is applied across the microfluidic channel compared to results obtained from phase-locking technique (red solid legend). The dash line represents the applied electric field across the microchannel channels.

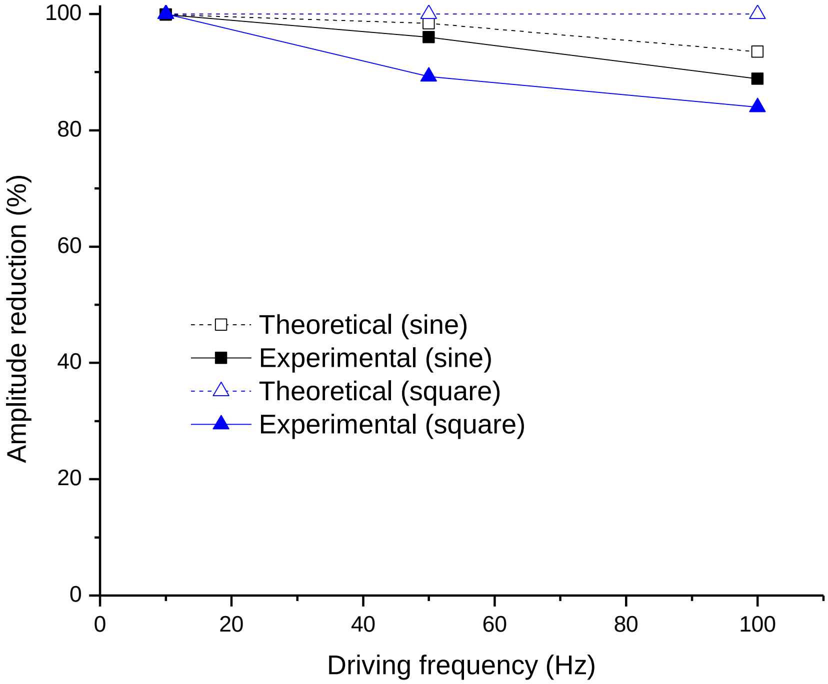

Figure 4-5 Amplitude comparisons between theoretical predictions (Eq. 6 and 7) and experimental results.

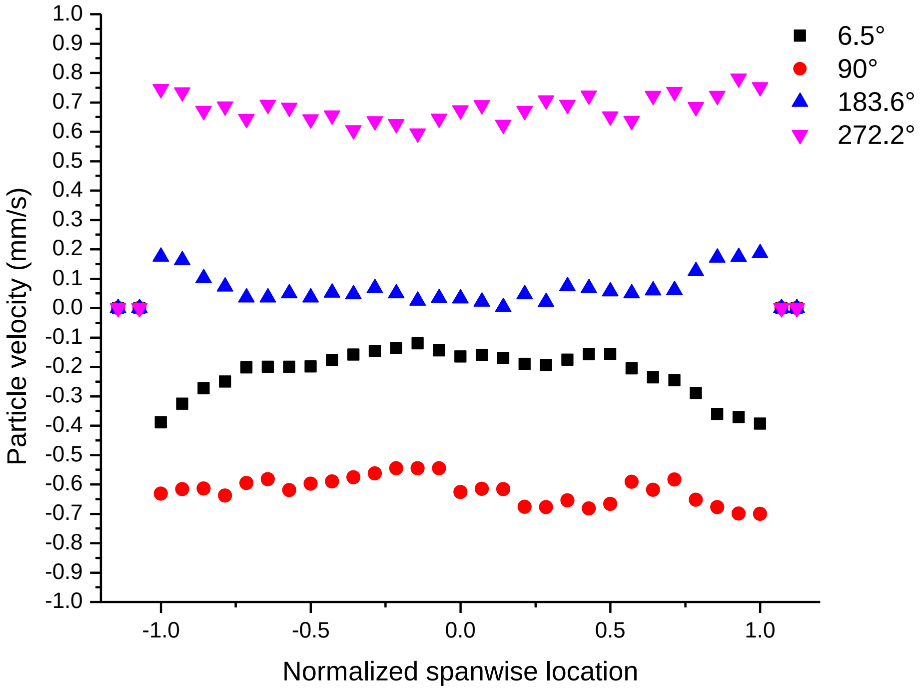

Figure 4-6 Temporal velocity profiles of electroosmotic flow when a 10Hz square-waveform signal with 200V amplitude is applied across the microfluidic channel evaluated from the PIV measurement using phase-sampling technique.

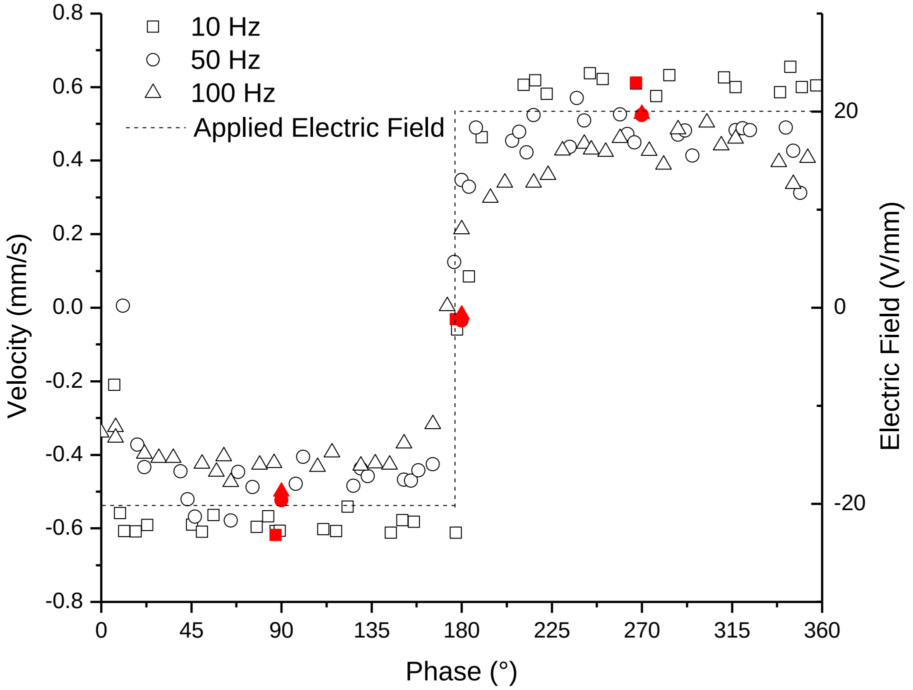

Figure 4-7 The square-waveform flow variation using phase sampling technique under various frequencies when 200V is applied across the microfluidic channel compared to results obtained from phase-locking technique (red solid legend). The dash line represents the applied electric field across the microchannel channels.

4.5 Conclusions

A new measurement technique has been successfully demonstrated for periodic flows using micro-PIV. A theoretical sampling resolution of 20 µs for 100Hz periodic flows can be obtained using the phase-sampling technique with sufficient number of dataset, and a resolution of 200 µs was demonstrated in the study using 40 sets of velocimetry results that took less than 10 sec for laser to collect the results. Flow measurements were performed for AC electroosmotic flows with a high operating frequency of 100 Hz (> laser pulse repetition-rate of 4.83 Hz) using phase-sampling. The results using phase-sampling technique show a rise time of 1.5 ms for 100Hz AC electroosmotic flows that matches the theoretical prediction. Moreover a good agreement with the results using phase-locking was found while eliminating the elaborate work and reducing experimental time. This study proves that this technique can be a beneficial tool to provide the time resolved measurements and the capability to capture the dynamic aspects of the forced periodic flow field in microfluidic devices.

Nomenclature

ΔT: time separation between two pairs of laser pulses

f_L: laser repetition rate

f_D: frequency of the driving potential

φ_n: equivalent phase

D_h: hydraulic diameter

ρ: density of the working solution

μ: dynamic viscosity of the working solution

U_{EO}: velocity of the electroosmotic flow

μ_{EO}: electroosmotic mobility

E: electric field

ζ : zeta potential

ε: permittivity

η: kinematic viscosity of the working solution

Chapter 5 Transport of Particles and Micro Organisms in Microfluidic Channels Using Rectified AC Electroosmotic Flow

This chapter is a reproduction of the following article to be submitted to Journal of Biomicrofluidics. The principle of zeta potential modulation is demonstrated to transport particles, cells, and other micro organisms using rectified AC EOF in open microchannels. The rectified flow is obtained by synchronous zeta-potential modulation with the driving potential in the microchannel. The effects of dielectric layer, driving electric field, gate potential, applied frequency, and phase lag between the driving and gate signals on the particle velocities were investigated and used to control the particle movement that can be a low-cost alternative to optical tweezers in certain applications. Moreover, in this study we found that PDMS might not be the best material for some pumping and biomedical applications as its hydrophobic surface property makes the priming process more difficult in small microchannels and also causes significant protein adsorption from protein-containing fluids.

Authors: Wen-I Wu, P. Ravi Selvaganapathy, and Chan Y. Ching

Publication Information: Journal of *Biomicrofluidics* 5, 2011, 013407-1 – 013407-12. doi:10.1063/1.3553011

Accepted Date: 3 January 2011

TRANSPORT OF PARTICLES AND MICRO ORGANISMS IN MICROFLUIDIC CHANNELS USING RECTIFIED AC ELECTROOSMOTIC FLOW

Wen-I Wu, P. Ravi Selvaganapathy, Chan Y. Ching*

5.1 Abstract

A new method is demonstrated to transport particles, cells, and other micro organisms using rectified AC electroosmotic flows in open microchannels. The rectified flow is obtained by synchronous zeta-potential modulation with the driving potential in the microchannel. Experiments were conducted to transport both neutral, charged particles and microorganisms of various sizes. A maximum speed of 50µm/sec was obtained for 8µm polystyrene beads, without any electrolysis, using a symmetrical square waveform driving electric field of 5V/mm at 10 Hz and a 360V gate potential with its polarity synchronized with the driving potential (phase lag = 0°).

5.2 Introduction

The processing of biological specimens in micro devices typically involves transporting these objects precisely to different locations on the micro device in order to perform various operations. A number of methods has been developed to transport particles and cells in closed channels using pressure-driven flow[59,60], electrokinetics[61], electroosmosis[62–64], electrowetting[65], and dielectrophoresis[66–68]. Most of these methods are only applicable in closed microchannels and cell transportation in open microfluidic devices is seldom reported. Open microchannels have their top side open to the ambient air and can provide advantages like maintaining the physiological conditions for normal cell growth and for introducing accurate amounts of chemicals and biological materials. Currently, the use of optical tweezers[69,70] is the mainstream method to manipulate particles and cells in open plates and microchannels. However, it requires complex optical setups and expensive lens systems that limit their widespread use.

Rectified AC electroosmotic flows[13,35,37] have been used for fluid flow in closed microfluidic systems. Compared to traditional AC electroosmosis (ACEO) where the flow is generated by the action of an electric field on its own induced diffuse charge near a polarizable surface and mostly operated at a frequency higher than 1kHz, this rectified AC electroosmotic flow is obtained by synchronization of zeta-potential modulation of the walls of the microchannel with the AC axial driving voltage along the microchannel. The objective of this study was to demonstrate the use of this rectified flow to transport both neutral and charged particles of various sizes in an open microchannel. The technique that we have demonstrated here can potentially achieve the core functionality of optical tweezers in particle manipulation without its associated high cost.

5.3 Working Principle

When a potential is applied across an open microchannel, the charges in the double layer induce fluid flow close to the bottom surface. The fluid motion near the bottom wall can transport particles and cells that are close to the surface, through frictional drag. The flow velocity U_{EO} near the bottom wall can be expressed by the product of electroosmotic mobility μ_{EO} and the local electric field E as

$$\overrightarrow{U_{EO}} = \mu_{EO}\vec{E} = \frac{\varepsilon\xi}{\eta}\vec{E} \tag{1}$$

where ζ is the zeta potential, ε is the permittivity and η is the viscosity of the working liquid. However, the application of a DC voltage in a local area can lead to gas evolution through electrolysis. Although the gases generate can be evacuated easily in open channels, they change the local pH and ionic concentrations as well as introduction convection due to formation and release of gas bubbles. The application of an AC potential with simultaneous zeta-potential modulation through a gate electrode at the walls of the microchannel has been shown to induce rectified fluid flow while avoiding gas evolution[13,35,37]. The working principle of rectified AC electroosmotic flow is depicted in Figure 5-1. Here a driving potential, which is a symmetric square voltage waveform (V_d), is applied along the axis of the microchannel. Another symmetric square voltage waveform, the gate potential (V_g), is applied on the gate electrode and phase synchronized with the driving voltage. The gate electrode is located at the bottom of the microchannel and covered with a gate dielectric layer. The application of a gate potential, causes accumulation of oppositely charged ions in the solution side of the gate dielectric which changes the native charge in the double layer. The proper synchronization of the gate and driving potentials causes a simultaneous change in the axial electric field and the charge in the double layer, producing a rectified body force and thus fluid transport. This is illustrated for the case when the native zeta potential and the charge on the double layer are positive. During the first half cycle, as shown in Figure 5-1(b), the driving potential is positive and the gate potential is negative. The zeta potential of the walls of the microchannel close to the gate electrode is enhanced over its native state since more positive ions are attracted to the surface to balance the charges on the gate electrode. The electroosmotic flow velocity in this half cycle is enhanced over the native state. During the second half cycle, the gate potential is positive, therefore a lesser number of positive ions than in the native state will be attracted to the surface which decreases the zeta potential and reduces the electroosmotic flow velocity. When this positive gate potential is larger than a certain threshold potential, the negative counter ions near the surface can be completely replaced by positive ions which results in a positive zeta potential and reversal of electroosmotic flow. Since the driving electric field is also reversed at this stage, the electroosmotic flow (Equation 1) under an alternating electric field can be rectified by this mechanism, while it would have a net-zero flow rate without the synchronization of the zeta potential modulation.

When the gate electrode is covered with an insulator which interacts with the solution in the microchannel, the zeta potential in the gate region can be controlled by the application of a gate potential. The insulator, the Stern and diffuse double layer can be represented by capacitors as shown in Figure 5-2. When a square wave AC potential is applied to the gate electrode, the influence of the gate potential on the local zeta potential can be described by[23]

$$\Delta\xi = \frac{C_{insulator}}{C_d} V_g \cdot z(\omega t) \tag{2}$$

where $C_{insulator}$ and C_d are the capacitance of the insulator and electric double layer, and V_g is the gate potential. Also,

z(ωt) = 1 when ωt < π

z(ωt) = -1 when π < ωt < 2π

The capacitance of the insulator is given by

$$C_{insulator} = \frac{\varepsilon_0 \varepsilon_r A}{d_{insulator}} \tag{3}$$

where A is the surface area, $d_{insulator}$ is the thickness of the insulator, and ε_0 and ε_r are the dielectric constant of vacuum and of the solution respectively.

Multiplying Equation (2) by ε/η, the modified electroosmotic mobility μ_{EO} is obtained as

$$\Delta\mu_{EO} = \frac{\varepsilon}{\eta}\Delta\xi = \frac{\varepsilon}{\eta}\frac{C_{insulator}}{C_d} V_g \cdot z(\omega t) \tag{4}$$

When an AC square waveform driving potential V_d is applied along the channel length L, flow along the bottom wall is generated by the native zeta potential of the bottom surface. The flow is propagated to the bulk fluid due to viscous drag. The net displacement however is zero, unless the zeta potential is modulated. The net velocity ΔU induced by the zeta potential modulation can be expressed as

$$\begin{aligned} \Delta U &= \Delta\mu_{EO}[E_d \cdot z(\omega t + \phi)] \\ &= \frac{\varepsilon}{\eta}\frac{C_{insulator}}{C_d}\frac{V_g V_d}{L} \cdot z(\omega t) \cdot z(\omega t + \phi) \end{aligned} \tag{5}$$

Here the driving potential V_d has an angular frequency of ω and a phase lag of φ with respect to the gate potential. The influence of the driving potential V_d, gate potential V_g, applied frequency ω, phase lag φ and dielectric constant ε on particle transportation in an AC rectified electroosmotic flow in an open microchannel was experimentally determined in this study.

It should be noted that the rectified flow causes frictional drag on the particles close to the surface and enable their movement. In addition, the driving electric field will introduce electrophoretic transport of the particles themselves due to the charge present on them. However, the electrophoretic transport averages to zero for a symmetric AC driving voltage. This is clearly observed in cases where there the zeta potential of the gate voltage is not modulated.

5.4 Experimental Setup

The microfluidic device is fabricated using an insulating Pyrex glass substrate. A thin Cr/Au (20nm/200nm) layer is deposited on the glass substrate using e-beam evaporation and serves as the gate electrode. A thin layer of PDMS pre-polymer is spin coated on top of the Cr/Au and thermally polymerized at 80°C. Alternatively, silicon oxide is deposited by a CVD process. This thin dielectric layer serves as the dielectric of a capacitor and modulates the charge on the double layer close to the bottom surface of the microchannel when a potential is applied to the gate electrode. Next, a PDMS channel (20mm x 2mm x 3mm), open at the top and the bottom is fabricated using soft lithography processes. This channel is bonded on top of the gate electrode/dielectric after surface activation. Two Ø250µm Platinum wires are inserted into the reservoirs of the open channel and used as driving electrodes. A schematic view of the experimental device is shown in Figure 5-1(a).

A 10Hz symmetric AC square waveform from a function generator (Tektronix AFG3022B) is connected to a voltage amplifier (Trek 677B) as shown in Figure 5-3. The driving and gate potentials were generated by amplifying the signal from a function generator as shown in Figure 5-3. The gate potential can be directly connected to one of the driving electrodes to synchronize the zeta potential modulation with the driving signal. However, this could result in an excess driving electric field (E_d) and electrolysis problems since the required gate potential to modulate charges in the double layer is much larger than the required driving potential. To avoid this problem, two separate amplifiers are used to control the driving potential V_d and gate potential V_g independently. The two outputs of the function generator are identical with an adjustable phase lag between the two channels.

The Amplifier 1 (Falco Systems WMA-02, gain= 20) is connected to driving electrodes and the Amplifier 2 (Trek 677B, gain= 200) is connected to the gate electrodes since the required V_g is generally much larger than V_d. The gate potential is synchronized with the driving electrodes as shown in Figure 5-3(b). The zeta potential is modulated as the driving potential varied, thus generating a non-zero flow rate under an alternating electric field.

The channel is filled with DI water with 8µm, 25µm polystyrene and 11µm, 18µm hollow glass particles suspended in it in different experiments. When the driving signal is applied with the gate electrode disconnected and floating as shown in Figure 5-3(a), the particle moves back and forth and do not have a net motion since the zeta potential at the bottom surface is not modulated.

5.5 Results and Discussion

A series of experiments were performed using various particles that are listed in Table 5-1. The transport of neutral and charged particles is demonstrated using polystyrene and glass beads. The effect of particle size on the particle transport was investigated using different sized particles. Particle movements are observed and recorded at 30 frames per second under microscope with a frame resolution of 1024×768. Each frame is then analyzed in ImageJ® software to measure the particle displacement. Since the frame rate is lower than the applied frequency, it was not possible to obtain the instantaneous velocity of the particle. Figure 5-4 shows the schematic of particle location versus time. The average velocity can be obtained from ΔX and ΔT over certain cycles that depend on the applied frequency, and used in the study to represent the particle velocity in the following figures.

5.5.1 Effect of Dielectric layer

Since the gate electrode, the insulator and the double layer form a capacitor, a dielectric layer with thinner thickness $d_{insulator}$, higher dielectric constant ε_r and lower diffuse double layer capacitance C_d is preferable in terms of the effectiveness of the gate potential in inducing zeta potential modulation as seen in Equation (3) and (4). The effect of the dielectric layer was studied by comparing two different dielectric layers: Chemical-vapour-deposited (CVD) silicon oxide film (ε_r=5) and spin-coated PDMS film (ε_r=2.5). The CVD silicon oxide is grown on top of the gate electrodes under the conditions of SiH_4= 90sccm, N_2O= 70sccm, power= 50W, pressure= 650mT, temperature= 300°C, and duration= 4min in Technics Micro-PD series 900 chamber, resulting in an oxide film of 2400Å thickness. The spin-coated PDMS is prepared by mixing a 10:1 ratio of PDMS prepolymer/curing agent (Sylgard 184, Dow Corning) mixture with hexane (3:1 weight ratio). The mixture is dispensed on top of the gate electrode and spun at 7000 rpm for 30 sec, resulting in a PDMS film of 12µm thickness[71]. After that, the PDMS film is cured at 85°C for 4 min. Since the CVD silicon oxide has a higher dielectric constant and is thinner, the CVD film can generate rectified AC electroosmotic flow and subsequent particle movement at lower gate voltages (as low as 10 V) as shown in Figure 5-5(a). However, the CVD oxide film breaks down at higher voltages probably due to pin-holes. In the case of the spin-coated PDMS insulator, there is no observeable particle movement when V_g is under 100V. However, it was able to withstand higher gate voltages and produced particle movement above 100V (Figure 5-5(a)). In order to obtain the double layer capacitance of the oxide and the PDMS surfaces, Figure 5-5(a) is rearranged according to Equation (4) and shown in Figure 5-5(b). The slope of the curve then represents the inverse of the diffuse double layer capacitance density A/C_d. Therefore the capacitances C_d for the interfaces of DI water/PDMS and DI water/CVD oxide can be obtained as 16.24μF and 967 μF respectively. These parameters were then used to obtain the theoretical fluid flow velocity in subsequent experiments. Furthermore, due to its better breakdown properties, spin-coated PDMS was chosen as the gate dielectric in the following experiments.

5.5.2 Effect of Driving Electric Field E_d and Gate Potential V_g

The variation of the velocity of 8μm polystyrene particles with the driving potential for a symmetric square signal with a frequency of 10Hz, phase lag of 0° is shown in Figure 5-6(a). The gate potential V_g in this case is equal to the driving potential V_d since they are simply connected together as shown in Figure 5-3(a). The driving potential was varied from 0 to 600V. The trend-line in Figure 6(a) shows that the velocity of the particles increases with the driving electric field in a quadratic manner, consistent with Equation (5) when $V_g = V_d$. It can be seen that the particle velocity is closer to the fluid velocity as indicated by the trend line, at low speeds and voltages. At higher operating conditions and speed there is deviation. This could be due to the inertial effect of the large particles which cause them to overshoot as the fluid velocity is changing direction. Since the velocity that the particles achieve during the positive and negative half cycles are different, it could lead to a higher rectified velocity.

Although this configuration is simpler to implement, it does not allow independent optimization of the driving and gate signals. For example, it is desired to have a low driving voltage when transporting biological specimens in the fluidic channel while using a higher gate voltage to achieve a higher velocity. In another configuration, two amplifiers are used to control the V_d and V_g individually but with polarity of the signals synchronized as shown in Figure 5-3(b). The variation in the velocity as the electric field E_d from 0 to 20,000V/m with the gate potential V_g fixed at 100V is shown in Figure 5-6(b). The particle velocity is lower here as compared to the previous case since the gate voltage V_g is lower compared to the setup in Figure 5-6(a). Once again we see deviations of the particle velocity from the fluid velocity above 50 μm/sec.

We also performed experiments where the driving voltage and its frequency were fixed and the gate potential varied. This configuration might be more suitable for biological specimens. The velocity obtained by applying various gate potentials is plotted in Figure 5-7. Here, the frequency and amplitude of driving electric field was fixed at 10Hz and $2.5\text{x}10^3$ V/m. Three different particles were tested: 8μm polystyrene, 11μm and 18μm hollow glass particles. For all three cases, the particle velocity increases with an increase in the amplitude of the gate potential. The effectiveness of gate potential can be defined as particle velocity divided by gate voltage (slope in Figure 7) that is 7.42×10^{-3} μm/V·s for 8μm polystyrene particle, 4.84×10^{-3} μm/V·s for 11μm hollow glass particle and 4.23×10^{-3} μm/V·s for 18μm hollow glass particle. The 8μm polystyrene particle has the highest effectiveness since its size is the smallest. It also shows that the particle velocity can be controlled independently by V_g while maintaining a relatively low V_d to avoid electrolysis problems as well as damage to biological specimen. Furthermore, it can be seen that the size and weight of the particles does affect the particle transportation speed by 43% by comparing 11μm and 18μm hollow glass particles. Finally, the lower velocities obtained cause significant deviation of the particle velocity from the fluid velocity.

5.5.3 Effect of Applied Frequency f and Phase Lag ϕ

The effect of applied frequency was studied using an AC square signal with V_g= 500V, E_d= 2500V/m, phase lag φ = 0°, and varying the frequency from 0 to 120Hz for 25μm polystyrene particles. The range of frequency was limited by the performance of the amplifiers. As shown in Figure 5-8, there is no obvious trend for particle velocity with the applied frequency. The variation of the particle velocity is within ±6.5% of the average velocity over the entire frequency range. This suggests that a higher frequency can be chosen to avoid electrolysis issues at the driving electrodes without an adverse effect on the particle transport speed. However, this is only valid within certain frequency range. The electroosmotic flow depends on the electric double layer (EDL) built up at the channel wall, and this EDL essentially acts like a capacitor. This particular charging mechanism is typically referred to as capacitive charging. Therefore, as the applied frequency approaches the inverse of RC time constant, the charging effect in electric double layer becomes dominant, and this imposes a limitation on applicable frequency.

The phase lag was varied from 0° to 360° while V_d, V_g and frequency were maintained at 100V, 700V and 10Hz respectively. When the phase lag is equal to 0° and 360°, $z(\omega t)\cdot z(\omega t+\varphi) = z^2(\omega t)$ and the particle velocities will be the highest. When the phase lag approaches 90° and 270°, the flow stops and particles cannot be transported. Finally, when phase lag is 180°, $z(\omega t)\cdot z(\omega t+\varphi) = -z^2(\omega t)$ and the particle velocity is the lowest. This behaviour is clearly observed in the experimental data as shown in Figure 5-8. There was no time delay between the particle velocity and the applied signal when the phase lag changed from 0° to 360°. Also, we can see the size and weight of particle affect the velocity by comparing the results of 11µm and 18µm hollow glass particles.

5.5.4 Transportation of Cells

Tests were performed to investigate the transport of biological specimens such as embryos and nematode Caenorhabditis elegans (*C.elegans*). The size of the embryos is ~40µm in length and ~25µm in diameter while the length of the nematode is around 1mm. The transport of embryo for a 10Hz signal with square waveform, ±15V/cm driving electric field and ±400V gate potential for different phase lag is shown in Figure 5-10. A low driving potential and high gate potential is chosen to avoid joule heating and excessive electric current passing the solution as only the driving electrodes are physically in contact with the solution. Initially, the embryo is at rest, then it starts to move toward the left when the signal above with φ = 0° is applied. When t = 5.7sec, the phase is switched to φ = 180° and the embryo turns over and begins to move toward the right until t = 17.1sec. The embryo subsequently developed into a viable nematode worm, demonstrating that the driving signal applied was benign. We also transported adult nematodes using the same mechanism. Images showing the position of a nematode being transported under a 3Hz square signal with E_d= ±100V/cm and V_g= ±200V are shown in Figure 5-11. During the transportation when E_d and V_g are ON, the nematode is momentarily paralyzed due to the electric field across the channel as shown in the second photo of Figure 5-11. These conditions were chosen to demonstrate the motion of the nematode due to the rectified flow alone while eliminating the normal motion of the organism by temporary paralysis. Subsequent observations also revealed that the nematodes quickly recovered their movement and were viable. It should be noted that the electric field required to cause significant damage such as in the case of electroporation is usually around 1kV/cm. The driving electric fields used in this study were significantly lower than that. This technique allows the flexibility of reducing the driving signal while increasing the gate signal to achieve a higher velocity for transportation.

5.6 Conclusions

Particles and biological specimens such as embryos and nematodes were successfully transported in a microfluidic open channel using rectified electroosmotic flow. The effects of dielectric layer, driving electric field, gate potential, applied frequency, and phase lag between the driving and gate signals on the particle velocities were determined. Each parameter can be used independently to control the transportation of the particles. Our work shows that both of driving electric field and gate potential can increase the particle velocity efficiently. The experimental results also suggest a higher frequency can be chosen to avoid electrolysis without an adverse effect on the particle velocity. Besides, the phase lag between driving and gate potentials can be used to modulate the particle velocity and even reverse the particle movement without changing other parameters, which could be beneficial in precise positioning. The benefits of such device can be a low-cost alternative to optical tweezers in certain applications.

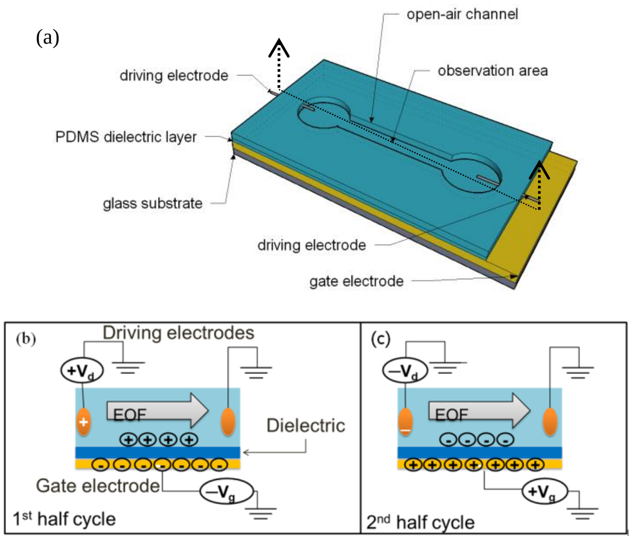

Figure 5-1 Rectified EOF device and its mechanism. a) Schematic of the microchannel device. b) At the 1st half cycle, the electroosmotic flow velocity is enhanced over the native state due to the accumulating positive ions near the surface when a positive driving potential and a negative gate potential are applied. c) At the 2nd half cycle, the electroosmotic flow is reduced or even reversed due to the accumulating negative ions near the surface when a negative driving potential and a positive gate potential are applied.

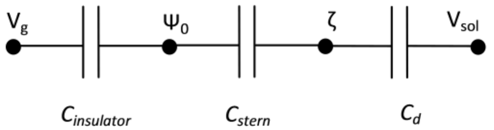

Figure 5-2 Three capacitor model for the zeta potential modulation at the solid/liquid interface where V_g is the gate potential applied on the gate electrode, Ψ_0 is the surface potential, ζ is the zeta potential and V_{sol} is the potential in the solution.

Table 5-1 Material information of the various particles

Product	Size (µm)	Material	Density (g/cm^3)
PPs-8.0, Kisker	8	Polystyrene	1.04
PPs-25.0, Kisker	25	Polystyrene	1.04
PBGH-11, Kisker	11	Hollow glass	1.1
PBGH-18, Kisker	18	Hollow glass	0.6

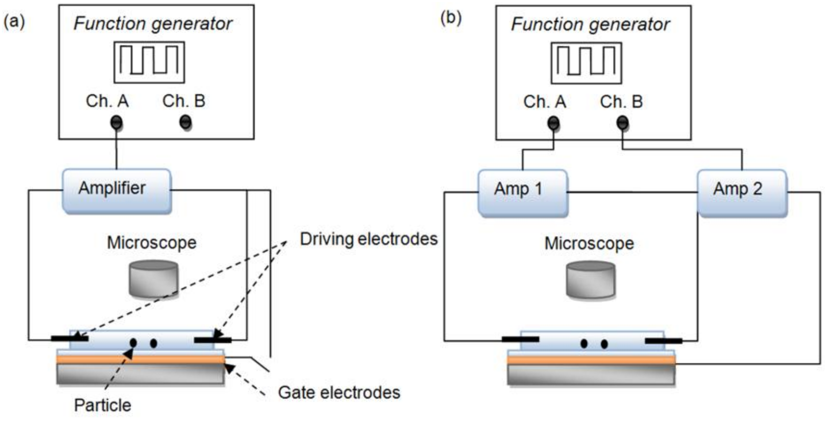

Figure 5-3 Experimental setup for zeta potential modulation. a) Configuration 1 where the driving and the gate potentials are coupled. b) Configuration 2 where the driving and gate potentials are independently controlled.

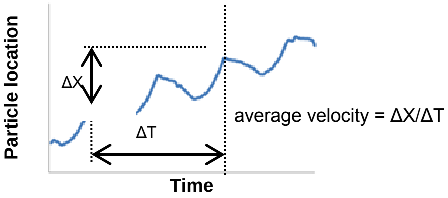

Figure 5-4 Schematic of particle location versus time

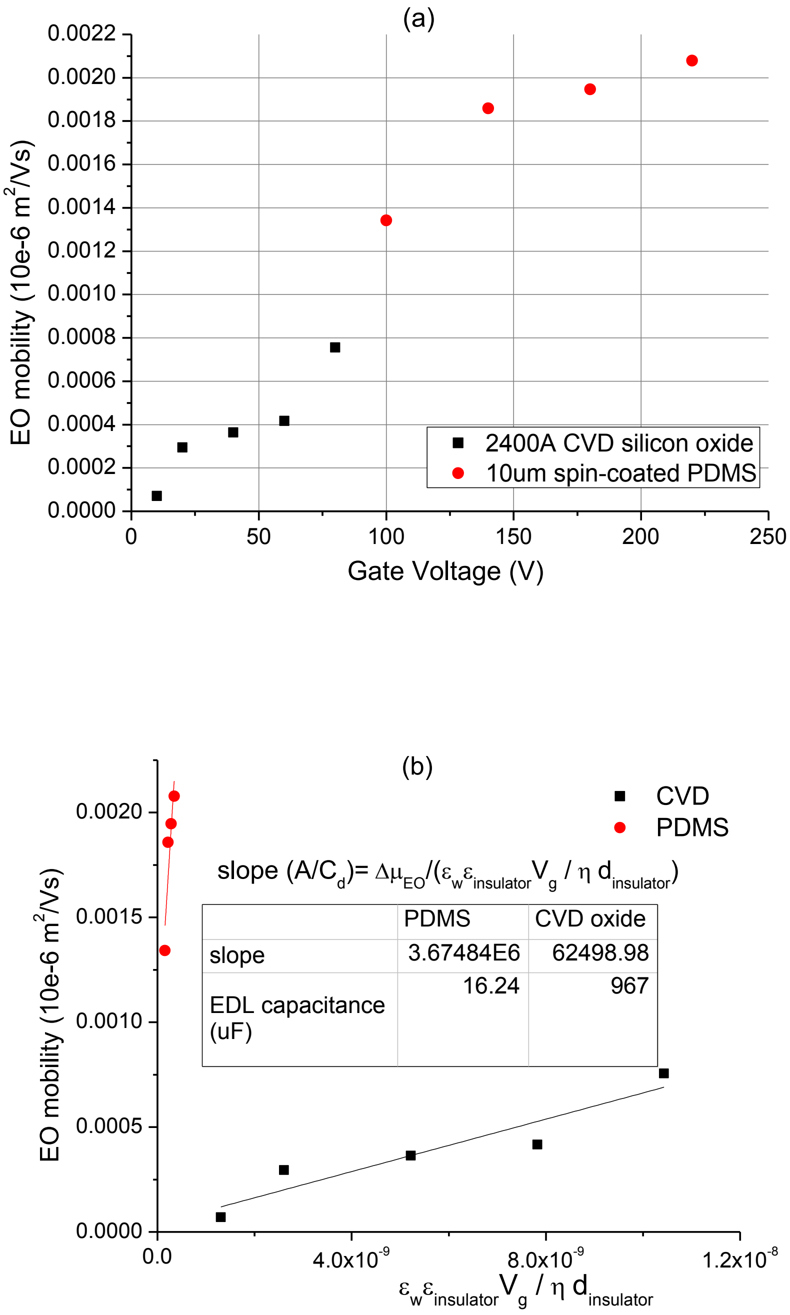

slope $(A/C_d) = \Delta\mu_{EO} / (\varepsilon_w \varepsilon_{insulator} V_g / \eta\, d_{insulator})$

	PDMS	CVD oxide
slope	3.67484E6	62498.98
EDL capacitance (uF)	16.24	967

Figure 5-5 Effect of the material of the dielectric layer on the electroosmotic mobility. a) Comparison of 2400Å CVD oxide and 12µm spin-coated PDMS. The CVD film can generate rectified AC electroosmotic flow and subsequent particle movement at lower gate voltages. b) Estimation of the double layer capacitance *C_d* from the slope of the curve which represents the inverse of the diffuse double layer capacitance density *A/C_d*.

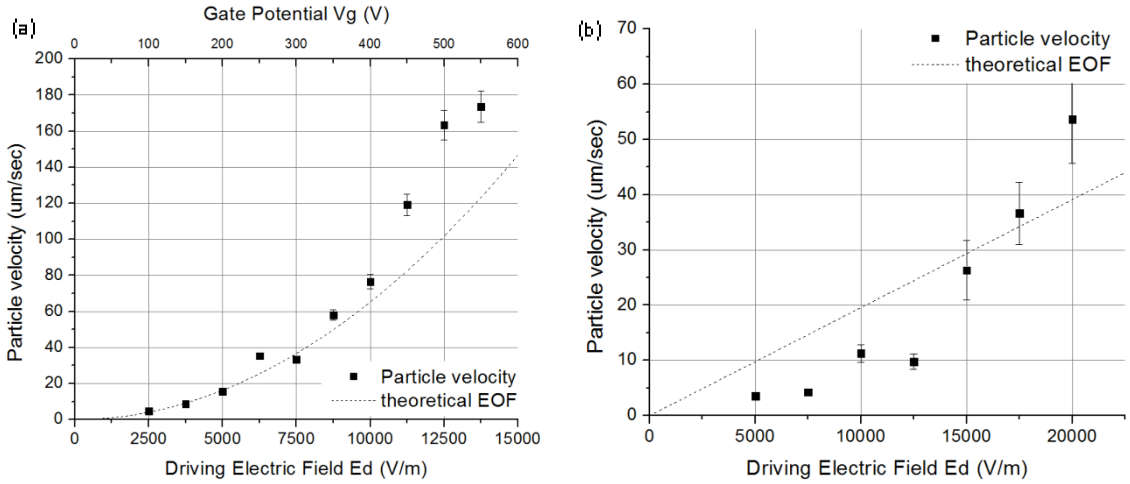

Figure 5-6 Effect of the driving electric field on the velocity of a 8 µm polystyrene particle. a) Configuration 1 where the driving and the gate potentials are coupled; Frequency is 10Hz. b) Configuration 2 where the driving and gate potentials are independently controlled; Frequency is 10Hz and gate potential is 100V. The theoretical velocity of the fluid flow is shown as the dotted line.

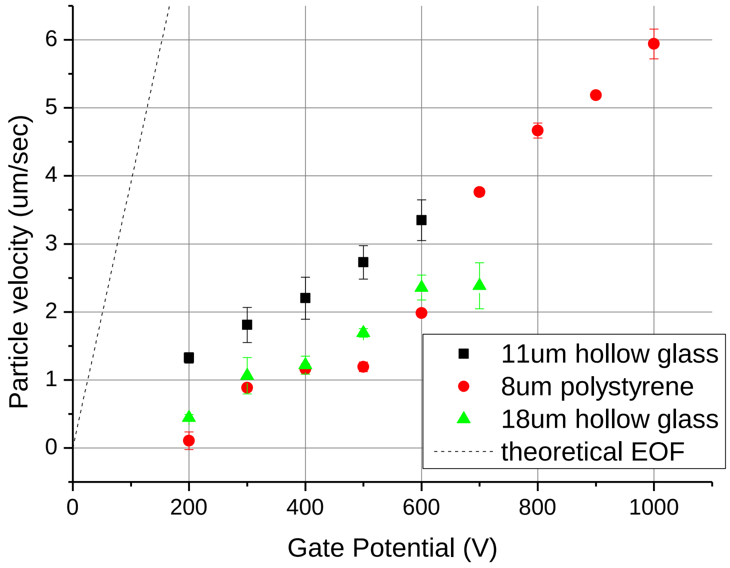

Figure 5-7 Effect of gate potential on the velocities of 8 µm polystyrene, 11 µm and 18 µm hollow glass particles when the driving electric field and frequency are kept at 2.5kV/m and 10Hz respectively. The theoretical velocity of the fluid flow is shown as the dotted line.

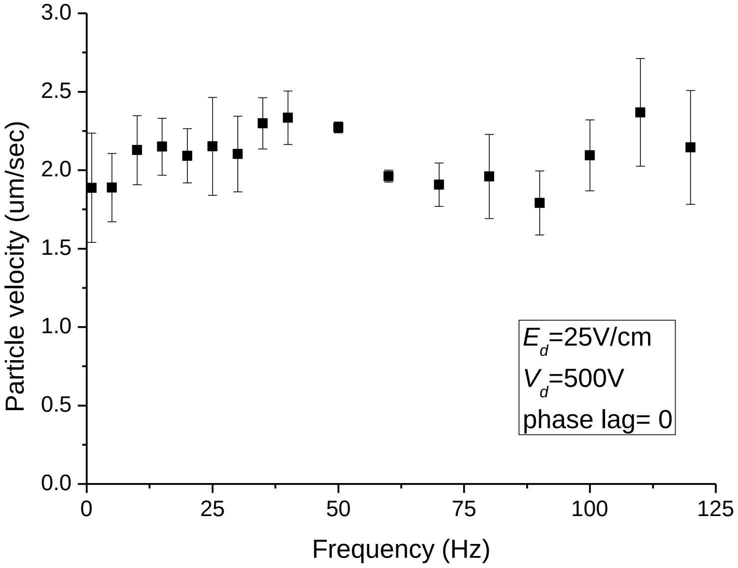

Figure 5-8 Effect of the applied frequency on the velocity of a 8 µm polystyrene particle when the driving electric field and gate potential are kept at 2.5kV/m and 500V respectively

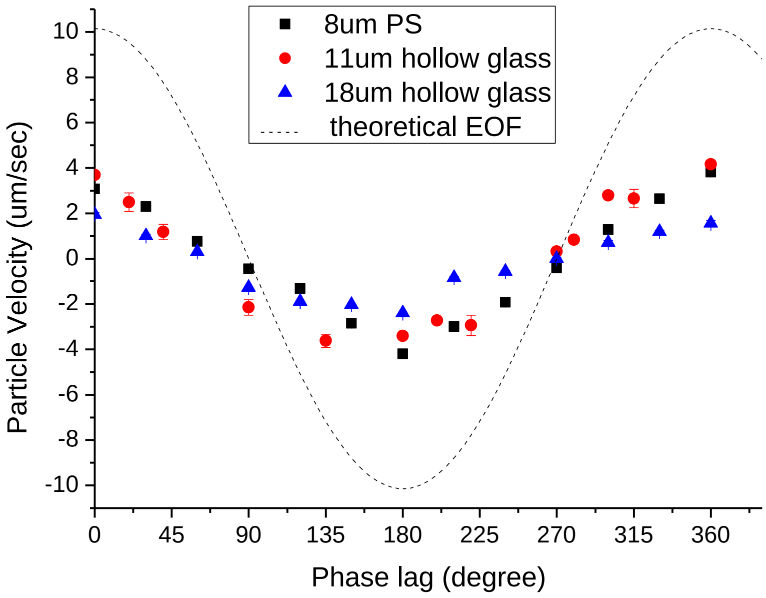

Figure 5-9 Effect of the phase lag on the velocity of 8 µm polystyrene, 11 µm and 18 µm hollow glass particles when the driving electric field and gate signals are kept at 2.5kV/m and 700V respectively. The theoretical velocity of the fluid flow is shown as the dotted line.

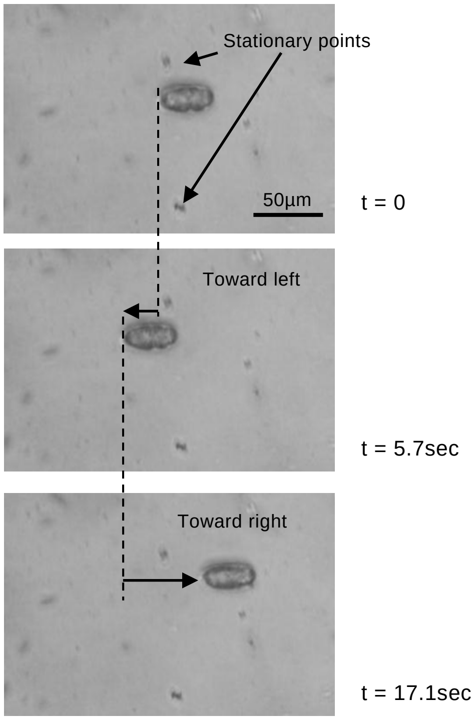

Figure 5-10 Positioning the location of embryo by control the phase lag. The embryos is moved toward the left when the phase lag φ = 0° from t = 0 to 5.7 sec; toward the right when the phase lag φ = 180° from t = 5.7 to 17.1 sec. Frequency is 10Hz , driving electric field is 15V/cm and gate potential is 400V.

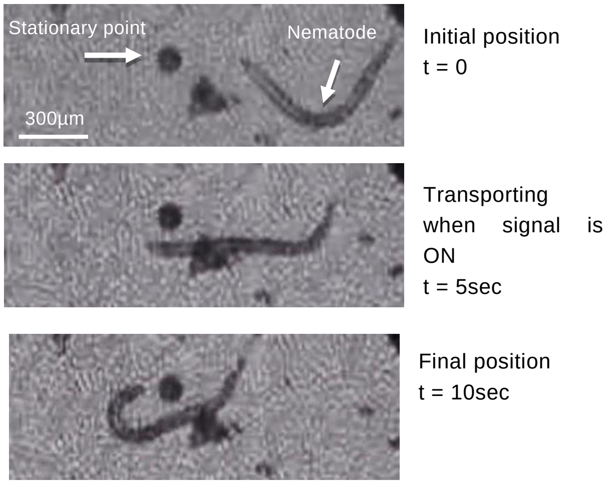

Figure 5-11Transportation of nematode by applying a 3Hz square signal with 100V/cm driving electric field and 200V gate potential. The nematode is being transported and momentarily paralyzed (straighten body) from t = 0 to 10sec when the applied signal is ON. After the signal is turned off at t = 10sec, the nematode recovered and started to swim by itself.

Chapter 6 Polyurethane-Based Microfluidic Devices for Blood Contacting Applications

This chapter is a reproduction of the following article to be submitted to Journal of Lab on a Chip. To eliminate the priming and protein adsorption problems due to PDMS's hydrophobic surface property, a more hydrophilic and biocompatible material, polyurethane (PU), was chosen to replace PDMS. In this chapter, we develop a polyurethane-based soft-lithography microfabrication to replace PDMS while providing better biocompatibility and pumping performance. Two new fabrication processes for making thin, transparent, flexible polyurethane (PU)-based microfluidic devices. We give details not only on the fabrication of microchannels but also their bonding, and the integration of fluidic interconnections as well as surface modification with hydrophilic polyethylene oxide (PEO) to improve their biocompatibility.

Authors: Wen-I Wu, Kyla N. Sask, John L. Brash and P. Ravi Selvaganapathy

Publication Information: Lab on a chip, LC-ART-11-2011-021075

Submitted Date: 8 November, 2011

Polyurethane-Based Microfluidic Devices for Blood Contacting Applications

Wen-I Wu, Kyla N. Sask, John L. Brash, and P. Ravi Selvaganapathy

6.1 Abstract

Protein adsorption on PDMS surfaces poses a significant challenge in microfluidic devices that come in contact with biofluids such as blood. Polyurethane (PU) is often used for the construction of medical devices, but despite having several attractive properties for biointerfacing, it has not been widely used in microfluidic devices. In this work we developed two new fabrication processes for making thin, transparent and flexible PU-based microfluidic devices. Methods for the fabrication and bonding of microchannels, the integration of fluidic interconnections and surface modification with hydrophilic polyethylene oxide (PEO) to reduce protein adsorption are detailed. Using these processes, microchannels were produced having high transparency (96% that of glass in visible light), high bond strength (326.4kPa) and low protein adsorption (80% reduction in fibrinogen adsorption vs. unmodified PDMS), which is critical for prevention of fouling. Our findings indicate that PEO modified PU could serve as an effective alternative to PDMS in blood contacting microfluidic applications.

6.2 Introduction

PDMS has been widely used in microfluidics for rapid prototyping because it is easy to fabricate, it bonds strongly to glass and PDMS substrates, and has good optical transparency and elastomeric properties. However, its intrinsic hydrophobic nature causes significant protein adsorption from protein-containing fluids. Blood is one such fluid with a high protein concentration and where the proteins play a functional role. For instance, fibrinogen, an abundant plasma protein and an important clotting factor, has been found to adsorb significantly more on hydrophobic than on hydrophilic surfaces.[72–74] The adsorption of fibrinogen potentiates the process of thrombosis including platelet adhesion and fibrin (clot) formation. A number of attempts have been made to reduce protein adsorption on PDMS surfaces and microchannels as summarized in recent reviews. Plasma[75–78], UV irradiation[79–81] and gas phase modification[82–84] have been used to make PDMS surface hydrophilic. However, these modifications are temporary and the surface was found to ultimately revert back to the hydrophobic state due to loss of the modifier.[85,86] Other methods are based on covalent attachment of surface groups through chemical modification. Attachment chemistries use organic solvents that swell PDMS[25] and are typically performed on open surfaces that cannot be bonded to other substrates[87] to form channels.

Polyurethanes (PU), since their development in the 1930s[88,89], have been widely used in various blood-contact applications such as the artificial heart[88], intra-aortic balloons[90], pacemaker leads[91], heart valves[92], and hemodialysis membranes[93]. Hydrophobic surfaces are essentially water repellent and provoke adverse reactions in blood contact. Many studies have shown that the blood compatibility of polyurethanes can be improved by making the surface more hydrophilic[94–96]. A number of in-vivo and in-vitro studies have been carried out to assess the cellular and tissue responses of PU either subcutaneously, intramuscularly, or intraperitoneally[97–107].

A very important consideration for hemocompatibility and biocompatibility is protein adsorption. In blood contact, for example, plasma proteins including albumin, haemoglobin, thrombin, fibrinogen (Fg), fibronectin, complement components, and immunoglobulins (IgG) adsorb onto polymeric surfaces immediately. Adsorbed fibrinogen in particular has been shown to be associated with thrombus formation. It has been suggested that blood compatibility may be improved by controlling interfacial interactions such that non-specific protein adsorption is prevented while selective adsorption of proteins for a desired bioactive function is promoted.[108] Approaches to limiting non-specific adsorption include modification of the surface with hydrophilic polymers such as polyethylene oxide (PEO) and poly(2-methacryloyloxyethyl phosphorylcholine) (polyMPC)[109–111]. Photo-chemical reactions[112,113] and various grafting techniques[114,115] have been used for this purpose. PEO is well known for its protein and cell resistant properties and different methods for generation of PEO-rich surfaces include adsorption, blending and grafting.[116–121] Although various methods for surface modification exist, such modification have been demonstrated on open surfaces or films of PU and not inside microfluidic channels. Surface modification inside microchannels present a different set of challenges such as rapid depletion of reagents due to high surface to volume ratio that the modification chemistry has to take into account.

Traditionally, solvent moulding techniques such as vertical dipping, rotating mandrel and rotating plate are used to fabricate PU parts such as sheets, membranes and tubing. The rotating plate method is used for fabricating PU films and sheets, while vertical dipping and rotating mandrel are used for fabricating cylindrical parts, like tubing. However, these fabrication techniques are not suitable for replicating the intricate and detailed microscale features present in microfluidics devices. PU-based microfabrication typically involves injection moulding[122,123], hot embossing[124], imprinting[125], plasma etching[126], sacrificial material[127] and reaction polymerization[123,127–130]. These methods are not suited for rapid prototyping as they use high-cost intermediate moulds and expensive fabrication equipment. Furthermore, the substrates produced are rigid and not transparent. Solvent casting is more suitable since intermediate moulds can be fabricated using photolithography and the fabrication equipment is low cost. However, the substrates that are produced are opaque, do not bond well and are difficult to connect with tubing.

Here, we report on a method for fabrication of PU similar to methods used for PDMS but leading to devices having hydrophilic interior surfaces. This method potentiates PU as an effective alternative to PDMS in many biological and biomedical microfluidic applications. We also develop several effective bonding and interconnection methods for solvent cast PU microfluidic networks to produce PU elastomeric devices that could be rapidly prototyped. In the work reported here we developed an in-situ surface modification method to graft PEO to PU surfaces in the interior of moulded and sealed microfluidic channels. The procedure is adapted from a previously published method[131]. Resistance to biofouling of the surface modified devices was assessed by measuring the adsorption of fibrinogen. Adsorption to devices fabricated using PDMS and unmodified PU was measured for comparison.

6.3 Experimental Details

6.3.1 Materials

The polyurethane Tecothane® TT-1095A was from Thermedics® Polymer Products (Wilmington, MA). SU-8 photoresists including SU-8 100, SU-8 2000.5, SU-8 2007, SU-8 2015, and SU-8 2025 and single-side polished mechanical grade silicon wafers were from Microchem Co (Newton, MA) and University Wafer (Boston, MA) respectively. Polydimethylsiloxane (PDMS) Sylgard® 184 was from Dow Corning (Midland, MI). N,N’-dimethylacetamide (DMA), dimethylformamide (DMF), tetrahydrofuran (THF), methylene chloride, cyclohexanone, chloroform, triethylamine (TEA, 99%), anhydrous toluene, chloroform, dimethyl sulfoxide (DMSO), xylene, 1-propanol, ethyl alcohol, cyclohexane, acetone, isopropyl alcohol (IPA), ethyl ether, methanol, N-hexane, glycerol, formaldehyde and anhydrous acetonitrile were from EMD Chemicals (Gibbstown, NJ) and were used as received. 4,4’-Methylene-bis (phenyl-diisocyanate) (MDI) and dihydroxy polyethylene oxide (PEO, MW=1000) were from Sigma Aldrich (Oakville, ON). Human fibrinogen was from Enzyme Research Laboratories (Southbend, IN). Masterflex® peroxide-cured silicone and Masterflex® Tygon® tubing were from Cole-Parmer (Vernon Hills, IL).

6.3.2 Solvent Casting Process

Solvent casting involves the formation of a replica by pouring the casting solution (prepared by dissolving polymer in solvent) into the mould. After curing (removal of solvent), a solid replica is created that can be removed from the mould. The mould can be used multiple times making the cost of the parts substantially cheaper. An important criterion in the choice of the mould material, the polymer and the solvent is that the casting solvent should dissolve the polymer completely but not dissolve or otherwise alter the mould at all.

In this study, we chose patterned SU-8 photoresist on single-side polished mechanical grade silicon wafers as the mould material due to ease of fabrication and resistance to the casting solvent. Various SU-8 photoresists such as SU-8 100, SU-8 2000.5, SU-8 2007, SU-8 2015, and SU-8 2025 were used to obtain a wide range of feature sizes.

Tecothane® aromatic polyether-based thermoplastic is a medical-grade polyurethane with good chemical resistance and biostability and has been used in many implantable medical[132, 133, 134] and healthcare applications[135, 136, 137]. It is licensed for long-term usage and has passed USP Class VI[134]. This material has been tested extensively in clinical practice. It has density (1.15 g/cc) and melting point (215.5°C) similar to PDMS. Its mechanical properties are superior, namely higher tensile strength (62 MPa), Young's modulus (55 MPa) and hardness (94 Shore A). Its dielectric constant is similar to that of PDMS and it performs well as an insulator. Tecothane® was chosen as a model material in this study due to its excellent properties and ready availability. Various organic solvents including dimethylacetamide, dimethylformamide, tetrahydrofuran (THF), methylene chloride, cyclohexanone and chloroform were tested for their ability to dissolve Tecothane® and for their compatibility with SU-8. THF was chosen since it dissolves PU readily, can be rapidly removed by evaporation at room temperature and leaves SU-8 mould intact after repeated cycles while other solvents either partially dissolve or swell SU-8 after curing. The PU "resin" is prepared by dissolving Tecothane®pellets in THF. A concentration of 10% (w/v) was found to be optimal for fast curing, high transparency and surface smoothness. The solution was prepared by stirring for 3 h at room temperature.

To achieve a robust, flexible and cost-effective interconnection, a solvent based method was developed. This method is suitable for any material that is soluble in THF. Two common tubing materials, silicone and Tygon® tubing, were investigated due to their reasonable solvent resistance and biocompatibility. Typically, Tygon® tubing provides higher pressure tolerance, lower gas permeability, and better chemical resistance than silicone tubing while the latter is relatively cheap.

6.3.3 Fabrication process

The casting based fabrication process for PU microchannels is shown in Figure 6-1. The PU solution is cast directly on the SU-8 mould. After curing for 60 min, fluidic interconnects (ϕ3 mm Tygon® or silicone tubing) are placed manually on top of the inlet and outlet reservoirs on the mould and fixed in place using PU solution as a glue. After curing for another 10 min, the patterned PU film with integrated interconnects is peeled off the mould and subsequently bonded to another flat PU film or glass substrate.

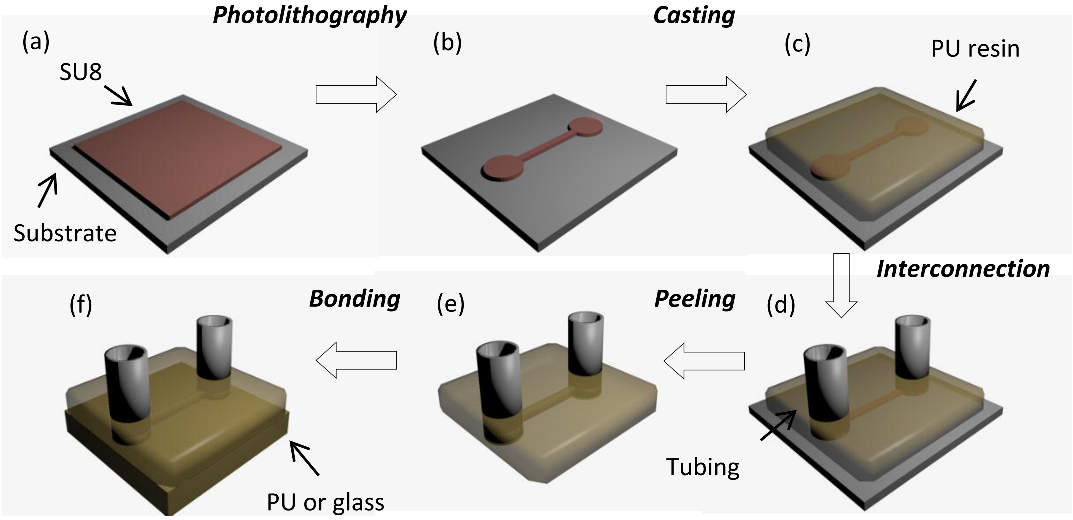

Figure 1

Figure 6-1 Process flow of PU soft-lithography

6.3.4 Moulding Process

The moulds were made with SU-8 photoresist by conventional photolithography (Figure 1). The thickness of the SU-8 moulds ranged from 0.5 µm to 80 µm. The PU solution was cast on the moulds (Figure 6-1(c)). Although solvent casting has been used to form PU thin films less than 50 µm in thickness[138] using THF as solvent, this method is not suitable for fabricating microchannels in thick films with intricate features for several reasons. First, THF is a solvent for many polymeric materials. Therefore, moulds have to be made of glass, silicon, ceramic materials or photoresists covered with electroplated metal layers[128] making them expensive and difficult to fabricate. Second, when thick films of PU are formed using THF as solvent by curing in ambient conditions (Figure 6-2(a)), small microscopic cavities may be present (Figure 6-2(b)). These cavities are formed by the rapid transport of the solvent, enabled by its high vapour pressure (143 mmHg), from the top layer of the thick film surface, into the atmosphere. Subsequently the spaces that are originally filled with THF become cavities or voids. This rapid transport causes the interface with air to dry faster compared to the bulk, leading to solvent trapping which upon evaporation leads to cavity formation.

The experiments with the different solvents showed that SU-8 is an ideal low-cost, photolithographically definable mould material for casting polymers dissolved in THF. Fully cured SU-8 had negligible dissolution in THF even with multiple castings. In order to mitigate cavity formation, the curing process was performed in a closed chamber, where the vapour pressure quickly reaches saturation and the curing process is slowed. Although this modification eliminated cavity formation, the time to completely cure a film 1 mm in thickness took longer than 12 h, making the method impractical. Consequently, a controlled evaporation method was developed using the setup shown in Figure 6-2(c). Here, the evaporation process is accelerated by heating the substrate to 65°C. The vapour pressure is maintained close to saturation by enclosing the substrate in a chamber. This "saturated" chamber prevents the hardening of the top layer and eliminates voids in thick films. Excess THF is allowed to condense and fall to the side. Using this setup, the curing process is complete within 1 h producing a smooth, transparent PU replica. While the surface features of the replica are determined by the mould, the thickness can be controlled by regulating the volume of PU solution. In our experimental setup, a 50 µm-thick PU replica was obtained by casting 10 mL of 10% (w/v) PU solution into the moulds made from SU-8 patterned 3" silicon wafers and placed in glass petri dishes.

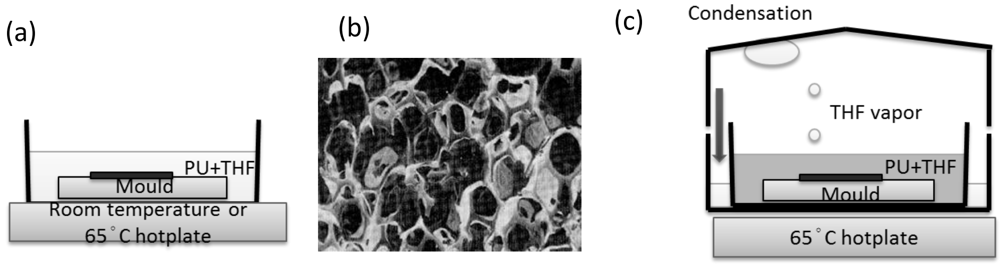

Figure 6-2 (a) General setup for solvent evaporation; (b) air voids and pockets trapped in PU; (c) dedicated setup for solvent evaporation without causing voids.

6.3.5 Interconnection

Reliable and leak-proof fluidic interconnects capable of withstanding high pressures are critical for microfluidic devices. Common methods include the use of adhesives[139, 140], o-rings[141, 142], Mylar polymer sealants[143], molten plastic tubing tips[144], mechanical compression[129,145–147], and commercial connectors such as Upchurch Scientific's Nanoport$^{\text{TM}}$ and LabSmith's CapTite$^{\text{TM}}$. While most commercial connectors provide fast assembly, tolerance of high pressure, and reliable interconnection, customized port design is required for microfluidic devices and the cost is high. The use of adhesives can be implemented easily but there is a risk of clogging if the adhesive seeps into the microchannels during application. Moreover the bonding strength varies depending on the material of the tubing and device. Use of adhesives and O-rings may lead to sample contamination especially if they are attacked by solvents and chemicals used in the device. An alternate low cost, reliable method is to use a solvent that dissolves the substrate and the interconnect thus re-enforcing the material at the interconnect and forming a strong, stable bond. This method, known as solvent welding, is commonly used for connecting plastic tubing such as polycarbonate, polystyrene, PVC and ABS and has been used to seal polymeric microfluidic devices using low boiling azeotropic solvents[148,149]. No foreign material is introduced after the solvent is evaporated and thus there is no contamination and the risk of catastrophic failure is low. Among the various solvents used in this work, THF was found to dissolve not only PU but also other materials such as silicone and Tygon® tubing.

In initial experiments, pure THF was used to partially dissolve the surfaces to be bonded, ie the PU replica and the tubing. The tubing was then placed on the PU surface and allowed to cure. Bonding occurred as the two materials “fused” and no fitting was required. However, since the evaporation of THF was rapid, the bond formed was relatively weak. In subsequent experiments, a solution of PU in THF (10% w/v) was applied to the regions on the PU replica and the tubing that were to be connected. The evaporation process was slower and produced a stronger bond between the interconnect tubing and the PU replica. The tip of the tubing was dipped into the PU solution and then aligned with the reservoir of the PU replica as shown in Figure 6-3(a). The combination was either left at room temperature for 30 min or on a hot plate at 65°C for 10 min to fully cure as shown in Figure 6-3(b). Subsequently, the cured PU replica with integrated interconnects was peeled from the mould as shown in Figure 6-3(c). Punch tools with ϕ3 mm cutter tips were used to remove residual PU inside the tubing as in Figure 6-3(d). The only limitation of this method is the size of the tubing as it becomes difficult to align and hold the tubing in position on the mould and clean residual PU inside it. Tubing with an inner diameter of 3 mm and a length of 25 mm was used in this study.

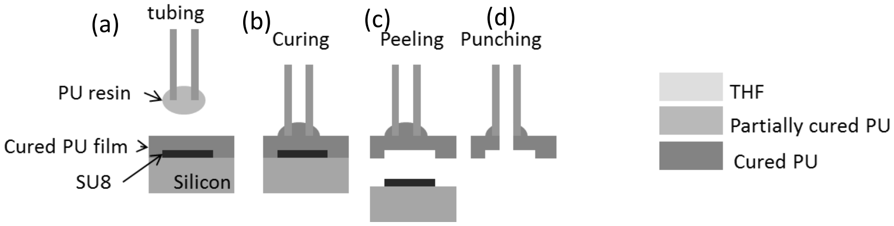

Figure 6-3 Interconnection procedure: (a) dip-coat partially cured PU on the tip of tubing; (b) place tubing on top of the inlet and outlet reservoirs on the mould and complete the curing process; (c) manually peel the pattern PU film with integrated interconnects; (d) remove residual PU from inside the inlet and outlet using punch tools.

6.3.6 Bonding methods

A major advantage of PDMS micromoulding that has made it the most popular rapid prototyping method in microfluidics is the ability to form a strong irreversible bond with glass or PDMS through a simple process of exposure to oxygen plasma. The bond formed is strong and can withstand significant pressure. For other polymers like poly(methyl methacrylate) (PMMA), polycarbonate (PC), polystyrene, cellulose acetate, and poly(ethylene terephthalate), the most common method is lamination to the other polymeric film with pressure sensitive adhesives[150] or thermally-activated adhesives[151, 152]. The bonding surface is wetted by the adhesive thus giving a strong bond. However they are susceptible to dissolution by solvents that may be used in the device and could cause contamination and failure. A similar, simple bonding method for PU does not exist. Semi cured parts of PU have been placed in contact and heated above the glass transition temperature causing fusion of the two parts[123,128]. However, this method is not suitable for retaining the fine structural features needed in microchannels.

In this work we developed several new methods for bonding PU parts with detailed microstructural features to other PU films. These methods can be categorized as dry and wet. Wet bonding methods include the use of dip coating and micro contact printing[130,153] and are suitable for high aspect-ratio channels. In this method, a flat PU film is either dipped vertically into pure THF solution for approximately 10 s to avoid excessive dissolution of the PU (dip coating, Figure 6-4(a)), or spin-coated with a solution of PU in THF (10% w/v) at 100 rpm for 10 s to avoid rapid solvent evaporation that occurs by convection at high rpm (micro-contact printing, Figure 6-4(b)). In the former method, the PU surface is partially dissolved by THF, retains some solvent and becomes adhesive. The microstructured PU layer is then placed on top of this partially dissolved PU film. In the latter method, the microstructured PU layer is stamped on the spin-coated wafer to transfer the PU resin from the wafer to the PU layer and then placed on top of another dry PU film. The combination is transferred to a hotplate and cured at 65°C for 10 min. Both methods are suitable for microchannels but not for nanochannels as the THF and PU resin will destroy any nanostructural features that are present. As an alternative, dry bonding of PU microstructured layers with PU films or glass using oxygen plasma was also investigated and used to fabricate nanochannels of height <1 µm. In this method, patterned and flat PU pieces or glass substrates were treated by oxygen plasma at 60 W for 1 min as shown in Figure 6-4(c) and then placed together under pressure (~1 kg) for 4 h to achieve stronger bonding. Similar procedures have been used for PDMS to improve the bond strength.[154]

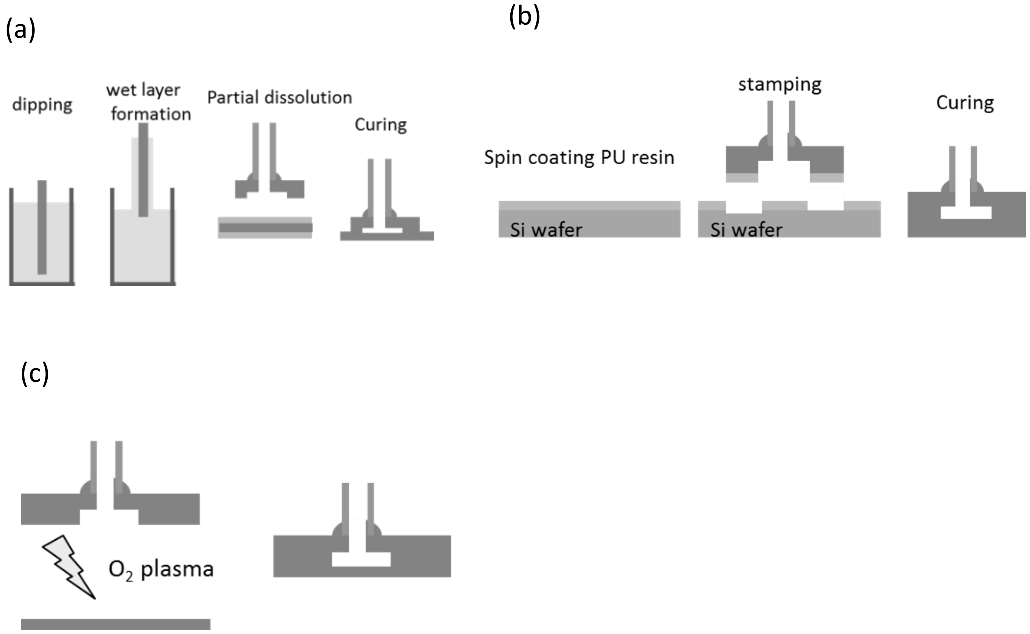

Figure 6-4 PU bonding. (a) Dip coating; (b) micro contact printing; (c) oxygen plasma treatment.

6.3.7 Surface modification

Attempts were made to improve resistance to protein adsorption by grafting poly(ethylene oxide) (PEO). Previous work[116–121] on attachment of PEO to PU used methods adapted for flat films and were found not to be suitable for microfluidic channels. The extent of surface modification was minimal probably due to high surface to volume ratio of the microchannels which leads to rapid depletion of the reactants. Therefore, a two-step process (Figure 6-5), based on previously published protocols[131], was adapted to graft PEO to PU microfluidic devices; typical device dimensions were 1 cm x 1 mm x 80 µm. First, a solution of 4,4'-methylenebis(phenyl isocyanate) (MDI) in anhydrous toluene (7.5%, w/v) containing 2.5% (w/v) triethylamine (TEA) as catalyst was heated to 50°C under a stream of nitrogen. Meanwhile, the PU-based microfluidic devices were dehydrated in a vacuum oven and then preheated to 70°C. The MDI solution (50°C) was then infused into the device with inlet and outlet sealed to prevent evaporation. The MDI solution was refreshed every 30 min. After 2 h, the devices were rinsed with anhydrous toluene and immediately infused with 7.5% (w/v) monomethoxy-poly(ethylene glycol) (MeO–PEO–OH) in toluene and reacted for 24 h at 40°C . The devices were rinsed with water to remove unreacted PEO and dried under vacuum overnight at 40°C.

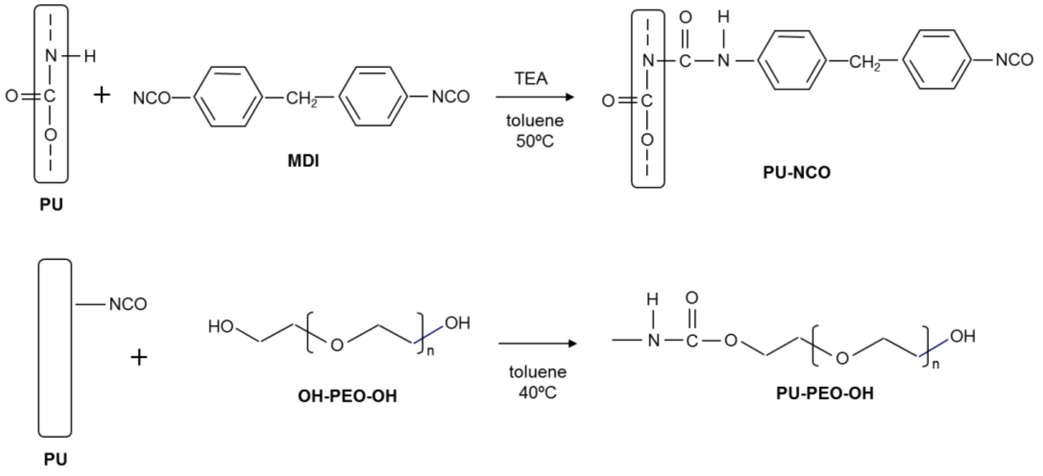

Figure 6-5 PU surface modification with PEO.

6.3.8 Measurement of protein adsorption

The adsorption of fibrinogen from buffer was measured using ^{125}I-labelled protein. Fibrinogen was labelled using the iodine monochloride method[131]. Free iodide was removed on AG 1-X4 resin. Residual free ^{125}I-iodide was determined using the trichloroacetic acid precipitation method and levels were kept below 1%. The solution for adsorption experiments consisted of 2% labelled and 98% non-labelled protein in phosphate buffered saline (PBS) at a total concentration of 1 mg/mL. The devices were incubated in PBS at room temperature for 2 h prior to exposure to the radiolabelled protein solution which was then infused via syringe. Adsorption was allowed to proceed for 3 h at room temperature. Following adsorption, the devices were rinsed 3 times (10 min each time) with PBS. Samples of the microchannels 6 mm x 1 mm x 80 μm (surface area of 0.13 cm^2) were punched from the devices and placed in counting vials for radioactivity determination using a γ-counter (Wizard 1480 – Perkin-Elmer). Unmodified PDMS, unmodified PU and PU-PEO microfluidic devices and ϕ6mm films were used in these experiments.

6.4 Results and discussion

6.4.1 Polyurethane replica characterization

Our modified experimental setup (Figure 6-2(c)) reduced the curing time to ~ 1 h by heating the mould to 65°C. The moulds had patterns for 10 microchannels in parallel between the inlet and outlet reservoirs and the channels had length and width of 1 cm x 150 μm and heights of 500 nm to 80 μm depending on the photoresist. The PU replicas as peeled from the mould appeared smooth and transparent. Images of the fabricated PU microchannels were obtained by scanning electron microscopy (SEM, Hitachi S-2150) (Figure 6-6). It can be seen that very good replication of the patterns in the SU-8 mould was achieved. The top and bottom surface appear very smooth while the sidewalls are straight and rough. The roughness of the side walls is due to the low resolution (10,160 DPI) transparency masks (Fine Line Imaging Co) used in the photolithography process and is observed in the SU-8 mould as well. The replication of striations on the sidewalls from the mould to the PU replica indicates that fine sub micrometer features can be replicated using this solvent casting process. To determine whether sub-micron channel sizes could be fabricated using this method, a mould with 500 nm high channels was used. The cross-sectional profile and surface roughness of the PU replica thus formed were measured using white light interferometry (Zygo NewView 5000, Zygo Corporation, CT) as shown in Figure 6-8. It is seen that features 500 nm in size can be replicated easily using this method. The results showed that the average surface roughness Ra of the channel area (moulded by SU8 photoresist) on the replica is 11 nm which is rougher than 6 nm of the area moulded by polished silicon surface. This result suggests that the surface roughness on the replica can be further reduced using photoresists with smoother surfaces and masks of better quality. The SU8 mould was used a number of times (≥10) without any damage or deterioration. The appearance of sealed devices is showed in Figure 6-7(a).

Optical transparency is crucial in microfluidic devices, especially for prototyping applications. The replicas prepared by casting produce optically transparent films as shown in Figure 6-7. To investigate light transmission, measurements were performed on 500 µm thick PU films (Beckman DU640 UV-vis spectrophotometer) in the wavelength range from 200 to 800 nm. A 150 µm thick cover glass slide (VWR No.1) was used as control. As seen in Figure 6-9 the average transmission of the PU film in the visible region (390-750nm) was above 85%; it absorbed strongly in the near-UV region (300-400nm). Absorption in the near UV is associated with the bonds in the polymer itself and causes photodegradation with gradual change in color (yellowing)[155] which is commonly seen in thermoplastics. The surface wettability of PU formed by solvent casting was determined by water contact angle (KRÜSS DSA100 goniometer) and compared to PDMS and glass. Samples were kept in ambient air for 2 days prior to measurement. The borosilicate glass slides were cleaned with acetone, methanol and DI water, and dried before testing. The results, reported in Table 6-1, show that unmodified PU was significantly more hydrophilic ($\theta = 63°$) than PDMS ($\theta = 113°$) and less hydrophilic than glass ($\theta = 51°$). The angles did not change significantly after two more days in ambient air. Its hydrophilicity can facilitate the priming process without applying pressure into the microchannels. As depicted in Figure 6-7(d), an unfilled PU microchannel was placed vertically and dipped into DI water dyed with methylene blue, and immediately the microchannel was self-priming by the capillary flow.

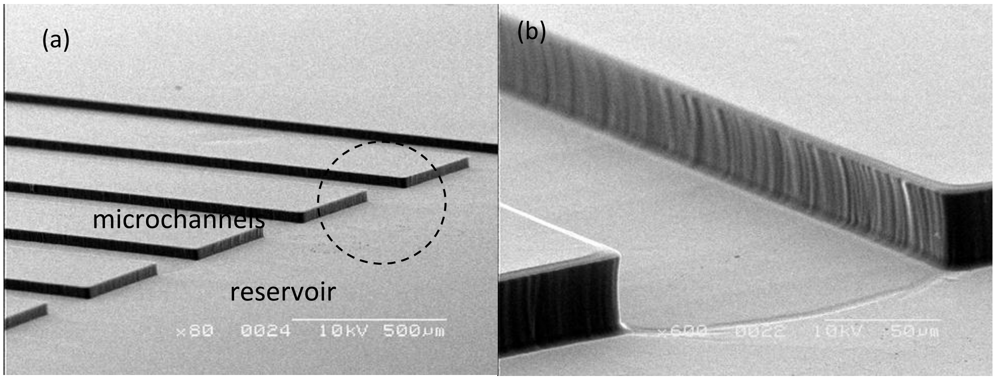

Figure 6-6 SEM of a microfluidic device with 10 microchannels in parallel between inlet and outlet reservoirs. (a) Unsealed PU replica (45 µm high), (b) high magnification view of the bottom and side wall surfaces in the microchannel.

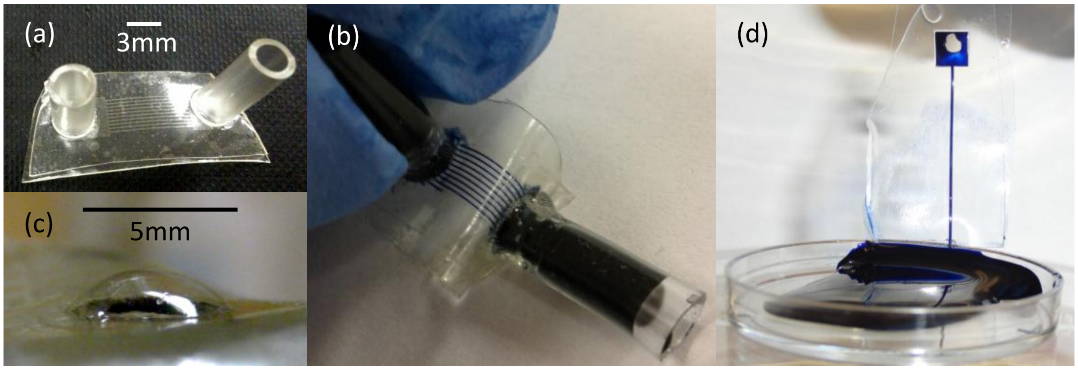

Figure 6-7 Photos of PU-based microfluidic devices. (a) Sealed device with integrated interconnect, (b) a flexible and bendable device with coloured microchannels for visualization, (c) a deflected PU membrane under a pressure of 200 kPa (ϕ5 mm and thickness = 25 µm), (d) self-priming microchannel (4 cm x 500 µm x 80 µm) filled with DI water (dyed with methylene blue) due to its hydrophilicity.

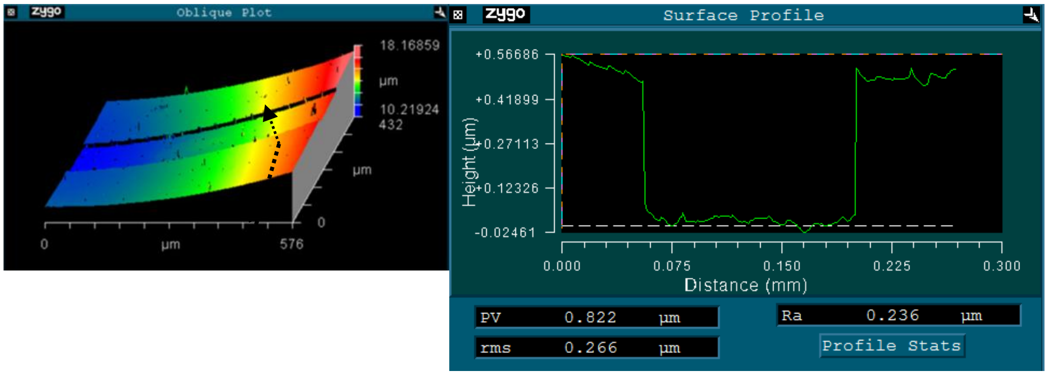

PV 0.822 µm

rms 0.266 µm

Ra 0.236 µm

Figure 6-8 Cross-section profile of unsealed PU nano-channel (500 nm high) from ZYGO optical profilometer.

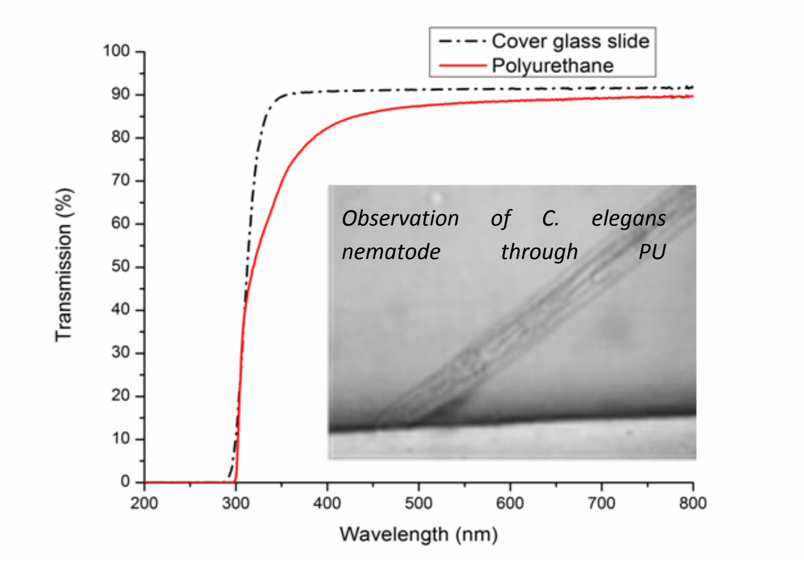

Figure 6-9 Optical transmission spectrum of polyurethane

Table 6-1 Contact angle measurements (4 µL DI water drops)

PU	*PDMS*	*Glass*
63.0±1.38°	112.9±4.8°	51.2±1.33°
	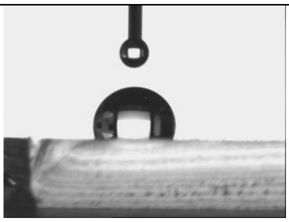	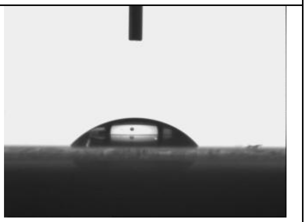

A major disadvantage of PDMS is that it swells in contact with organic solvents. Swelling tests were performed on solvent cast PU films to determine their solvent compatibility compared to that of PDMS. Disks of PU (ϕ6 mm) were immersed in dimethylformamide (DMF), tetrahydrofuran (THF), chloroform, dimethyl sulfoxide (DMSO), xylene, 1-propanol, toluene, ethyl alcohol, cyclohexane, acetone, isopropyl alcohol (IPA), ethyl ether, acetonitrile, methanol, N-hexane, glycerol, formaldehyde, and DI water for 24 h. The diameters of the disks were measured and analyzed (IMAGEJ® software) before and after immersion, with swelling ratio defined as $S = D/D_0$ (D diameter after 24 h in solvent, D_0 diameter of dry disk). As seen in Figure 6-10, THF and DMF dissolved the PU; only chloroform and DMSO gave $S > 1.1$. The swollen PU returned to its original shape after removal of the solvent. With DMSO, however, the PU was transformed into a white gel. These results demonstrate that PU is compatible with most solvents except THF and DMF, and in general swells less than PDMS[25] which has S = 1.39 for chloroform, 1.41 for xylene, 1.33 for cyclohexane, and 1.31 for toluene.

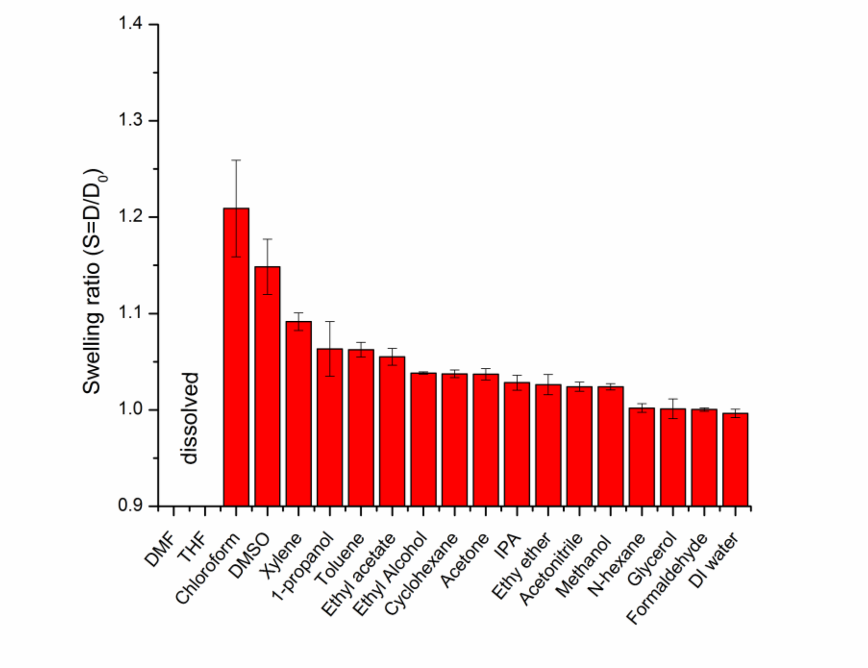

Figure 6-10 Solvent compatibility based on the swelling ratios of PU after 24 h immersion. Data are means ± SD, n = 5.

6.4.2 Characterization of sealed PU microfluidic devices with integrated interconnection

Using the solvent seal method shown in Figure 6-3, Tygon® was used as interconnect tubing since it has higher pressure tolerance than silicone. The combined interconnect and microchannel relief was bonded to a thin PU film to seal the microchannel. Since the surfaces on the PU replica and the tubing were partially dissolved by THF, a strong bond was expected to form. Figure 6-11 shows a SEM cross section of the bonded region where the Tygon tubing interfaces with the PU microchannel. It can be clearly seen that the bottom PU film, the top PU film and the Tygon tubing merge with one another. No clear interface can be seen indicating formation of a strong bond. Burst tests were conducted by sealing the outlet interconnect and applying increasing pressure on the inlet. Failure at the interconnect-PU interface was not observed up to 375 kPa pressure. At higher pressure the fitting connecting the pressure sensor to the device leaked.

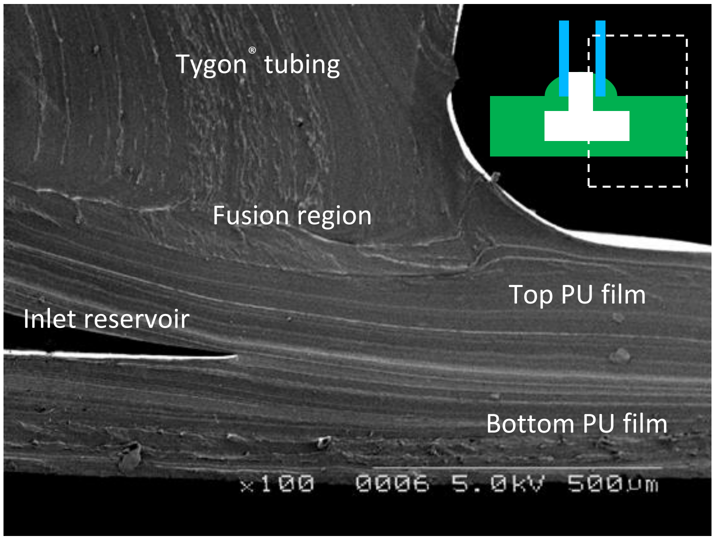

Figure 6-11 SEM of the bonding interface of Tygon® tube and PU film

The various wet and dry bonding methods shown in Figure 6-4 were evaluated for pressure resistance. A cross section of the channels formed by PU films patterned with microchannels bonded to flat PU thin films using microcontact printing (Figure 6-4(b)) is shown in Figure 6-12. It can be seen that the rectangular cross section of the channels was preserved in the microcontact bonding process. Furthermore, no clear interface can be seen between the top and bottom PU film indicating that fusion of the material at the interface is good with strong bonding expected. One notable feature of PU is its high Young's modulus which allows microcontact printing and bonding of thin films while still preserving the integrity of the microchannels. Channels such as those shown in Figure 6-11(c) (10 x 150 um cross section) with thin top and bottom films would collapse during microcontact printing and bonding if made from PDMS. The ability to fabricate extremely thin microfluidic devices allows the device to be much more flexible and bendable as shown in Figure 6-7(b)(c) and therefore useful in applications where rolling is needed.

The burst pressures of sealed PU microfluidic devices with integrated interconnects fabricated by various bonding methods were determined. Water was infused through the Tygon® interconnect at a flow rate of 1 mL/min via a syringe pump (Harvard Apparatus, Holliston, MA), and the outlet of the microfluidic device was connected to a pressure sensor (Omega PX273-300DI). The pressure within the device was recorded. Data are shown in Table 6-2. For each bonding method 5 replicate burst tests were performed and the average values are reported. Dry bonding involving activation of the PU surfaces in oxygen plasma (60 W, 1 min) gave a burst pressure of 42±3.3 kPa indicating a very weak structure. A similar technique used for bonding PU to glass resulted in a slightly higher bonding strength of 150±10.1 kPa. The dip coating method gave a bond strength of 229.9±24.3 kPa, substantially higher than the oxygen plasma method. Dip coating transfers some of the THF to the PU surface, dissolves it and when brought in close contact with the other PU film during bonding, partially dissolves the other surface. After curing, material from both substrates fuses and a tight bond is formed. Similarly, using a more precise microcontact printing method where the amount of THF loaded onto the PU substrate is controlled and uniform yielded an even higher bond strength of 326.4±19.6 kPa.

The various bonding methods were also characterized in terms of changes induced in the channel shape. The width and height of the microchannels in the PU replicas were measured using SEM images (Figure 6-13). It can be seen that the PU replicas retained the width of the SU-8 mould for both the wet and dry bonding methods. However, there were significant differences in the channel heights between the two methods. As expected, the channel height in the dry bonding method was the same as in the SU-8 mould. However, for the wet bonded channels the heights were lower than the height of the SU-8 mould. This indicates that the dissolution of the bonding surfaces and the subsequent application of a force during the bonding process leads to relocation of material and reduction in the channel height. This effect can be minimized by reducing the amount of THF used in the dip coating and micro contact printing processes. These results suggest that the dry bonding method is better suited for channels of small cross section.

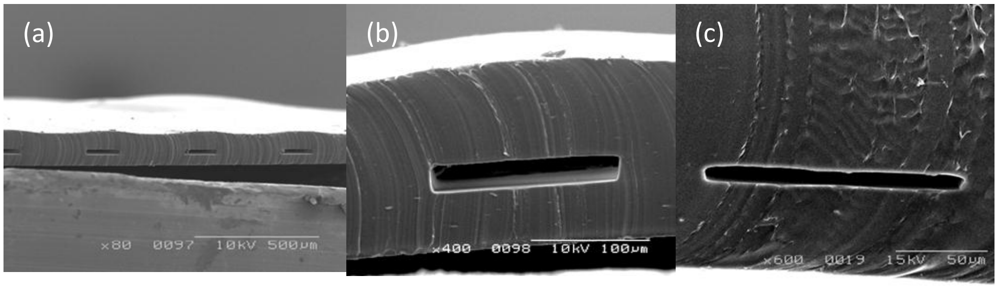

Figure 6-12 SEM images of (a) cross-section of sealed PU channels formed by μcontact printing, (b) 45 μm high sealed PU channel (zoomed view) and (c) high-aspect ratio PU sealed channel, 10 μm high X 150 μm wide (zoomed view).

Table 6-2 Burst pressures of sealed PU microchannels. Data are means ± SD, n = 5.

	PU/PU O_2 plasma	PU/Glass O_2 plasma	PU/PU dip-coating	PU/PU μcontact printing	PDMS/PDMS O_2 plasma

Pressure (kPa)	42.2 ±3.3	150.4 ±10.1	229.9 ±24.3	326.4 ±19.6	300
Failure	Delamination	Delamination	Burst at edge	Leakage at connector	Burst at edge

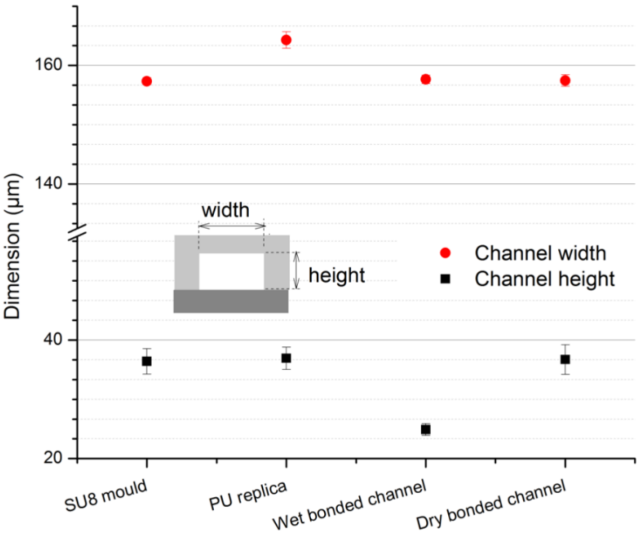

Figure 6-13 Variation of channel width and height for bonding methods. Data are means ± SD, n = 4.

6.4.3 Electroosmotic mobility and dielectric performance

Other characteristics that may be of importance in microfluidic devices such as electroosmotic mobility and dielectric constant were also investigated. Since there are no surface charges on unmodified PDMS and PU, electroosmosis is expected be low and similar in microfluidic channels of these materials. This could be beneficial for applications like capillary electrophoresis and protein separation, but detrimental for DC electroosmotic pumping.

Electroosmotic flow (EOF) was measured by tracking the movement of 1 µm neutral polystyrene particles in buffer solution at pH varying from 4 to 10 and voltage from 100V to 200V applied across 1 cm long microchannels. The particle motion was recorded and analyzed by microparticle image velocimetry (TSI) to obtain the electroosmotic velocity. The electroosmotic mobility (velocity divided by applied electric field) was found to be $2.47\times10^{-8} m^2V^{-1}s^{-1}$ at pH 7 (Figure 6-14), slightly smaller than reported for

PDMS ($3.8\times10^{-8}m^2V^{-1}s^{-1}$)[156]. Both PU and PDMS[157] showed increasing electroosmotic mobility with increasing pH.

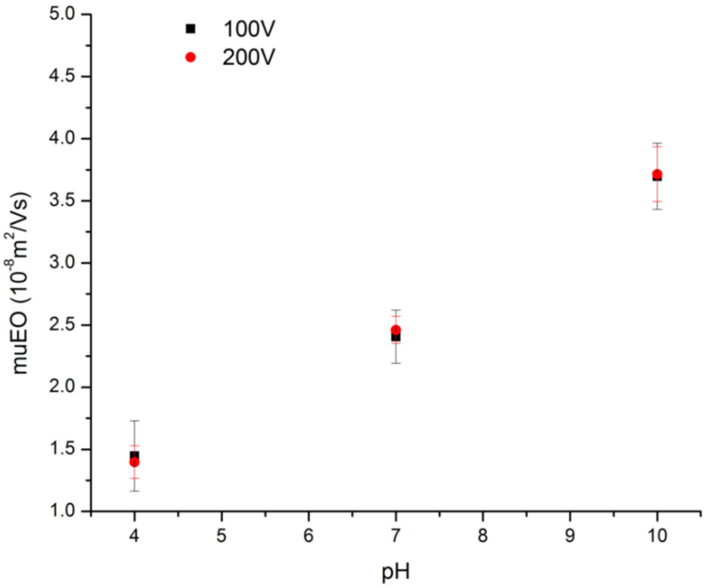

Figure 6-14 Electroosmotic mobility (muEO which is defined by the EO velocity over the applied electric field) versus pH. Data are mean ± SD, n = 4.

6.4.4 Protein adsorption

Biofouling is a significant issue in many applications and in blood contacting devices it is particularly problematic because of its propensity to initiation the blood coagulation cascade. Once coagulation is triggered a fibrin clot will soon form and for microfluidic devices that have limited space, blockages would be detrimental to their continued function. This effect was tested by filling native PDMS microfluidic channels (L 3 cm x W 1 mm x H 100 µm) with human blood and observing clot formation. Within five min of incubation at room temperature, a clot formed and immediately stopped the flow through the device (data not shown).

For these experiments thin films as well as microchannels made from PDMS, unmodified PU and PEO-modified PU were used. Adsorption was found to be similar on unmodified PDMS and PU for both films and devices (Figure 6-15). The PEO-modified PU device samples showed a significant reduction in adsorption >80% compared to unmodified PDMS and PU. The similar levels of fibrinogen adsorption observed on devices and films confirmed that the surface modification process as adapted for the microfluidic devices was successful. These low levels of fibrinogen adsorption are expected to translate to reduced platelet adhesion and reduced procoagulant activity. Further investigation of these and other biological responses are warranted.

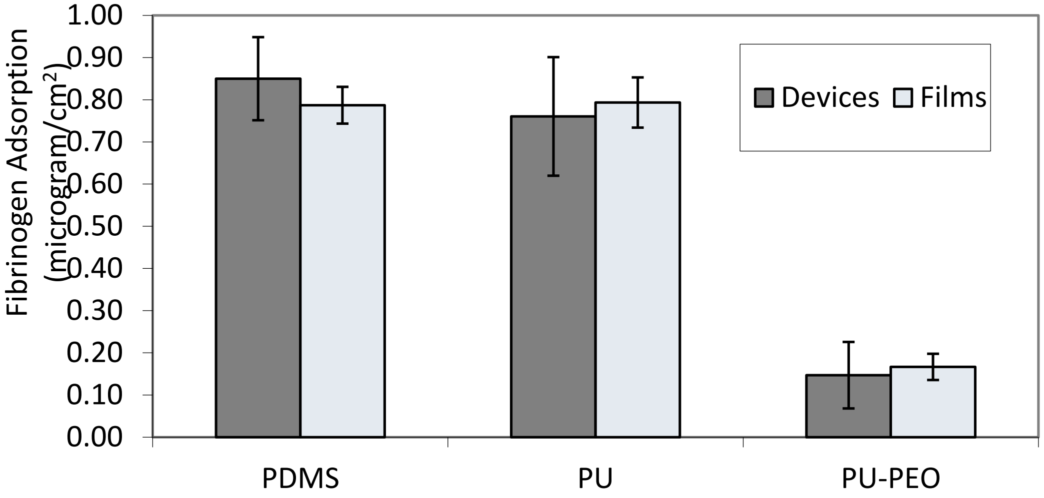

Figure 6-15 Fibrinogen adsorption (1 mg/mL in PBS, 3 h) to devices and films. Data are means ± SD, n =3.

6.5 Conclusion

A new fabrication method for PU-based microfluidic devices was developed. Devices fabricated using biomedical grade PU showed similar properties to PDMS such as replica quality (roughness of 11 nm), bonding strength (326.4 kPa), optical transparency (96% that of glass) and solvent compatibility (better than PDMS). The PU surfaces showed increased hydrophilicity compared to PDMS and were amenable to chemical modification. Three bonding methods were developed that could cater to various application specific factors such as convenience (dip coating), strongest bonding strength (micro-contact printing) and nanostructural features (oxygen plasma treatment). The micro-contact printing provides the best performance for most microfluidic applications that have the channel size is micrometer scale. An integrated fabrication of interconnects facilitates the tubing processes for flow connection in microfluidic devices and the entire device has the ability to withstand a pressure up to 326.4 kPa. The in-situ surface modification method was also successfully demonstrated to graft PEO to PU inside the moulded and sealed microfluidic devices. The reduced levels of fibrinogen adsorption (80%) observed on PEO modified PU devices in comparison to native PDMS and native PU, demonstrate successful modification of the inner device surfaces and provide a more biocompatible surface with potential for resistance to blood clot formation. Extending the micro-contact printing technique to smaller dimension channels and testing of clotting behaviour in surface modified PU channels are possible future avenues for research.

Chapter 7 The Development of Electrokinetic Pumps using Rectified AC Electroosmotic Flows

This chapter is a reproduction of the following article to be submitted to Journal of Microfluidics and Nanofluidics. Finally, an electroosmotic pumping device driven by zeta potential modulation and fabricated by PU soft lithography was presented. The flow rate and pressure output are characterized through several parameters as driving potential, gate potential, applied frequency, and phase lag between the driving and gate potentials. Direct measurements of the pressure generation are detailed without using flow rate conversion which has been found in most previous literature.

Authors: Wen-I Wu, and P. Ravi Selvaganapathy

Publication Information: To be submitted

Submitted Date: To be determined

The Development of Electrokinetic Pumps using Rectified AC Electroosmotic Flows

Wen-I Wu and, P. Ravi Selvaganapathy

7.1 Abstract

This paper details the development of the rectified AC electroosmotic microfluidic pumps. The rectified flow is obtained by synchronous zeta-potential modulation with the driving potential in the microchannel. The flow rate and pressure output can be controlled through several parameters like the driving potential, gate potential, applied frequency, and phase lag between the driving and gate potentials. Direct measurements of the pressure generation without using flow rate conversion are investigated. A maximum pressure output of 2.7 kPa can be obtained from this pumping device with 1 Hz square-waveform signals, and 1000 V and 1500 V amplitudes for driving and gate potentials respectively using DI water as working solution while a maximum flow rate of 9.5×10^6 $\mu m^3/s$ was obtained with 1 Hz square-waveform output signals, and 1500 V and 1300 V amplitudes for driving and gate potentials respectively.

7.2 Introduction

Among all the components for the microfluidic systems, developing micropumps capable of generating pressures and flow rate to precisely move microscopic volumes of fluids across precise distances, is the most challenging. Micropumps have a variety of applications in almost all microfluidic devices used in cell trapping, drug delivery and chemical synthesis among others. Pressure driven pumps are generally used for the fluid transport to overcome large hydraulic resistances in microfluidic and nanofluidic channels by applying high pressure to produce small flow rates. On the other hand, electrokinetic phenomena that include electroosmosis, electrophoresis, streaming potential and sedimentation potential occur due to the interactions of electric charges and liquids and scale favourably with miniaturization and offer unique advantages in microfluidics, such as low hydrodynamic dispersion, no moving part, electrical actuation and sensing, and easy integration with microelectronics. Electrokinetic pumping using the interaction of the working fluid with an electric field to generate the fluidic movement and pressure are attractive alternatives for transporting fluid on the microscopic scale because of the minimal fabrication requirements due to the absence of moving parts and the resulting low cost. The flow depends on the surface charge at the walls of the microchannel and can be controlled by modification of the solid/liquid interface. This modification can be either chemical[20,21] or electrical[18,158–160]. The former had been used to minimize the electroosmotic flows in capillary electrophoresis by changing the chemical composition of the buffer solution or the coating of the inner surfaces of the microfluidic channels, and the latter uses a way analogous to the solid-state field-effect transistor (FET) by embedding the gate electrodes underneath the microchannels. The surface charge will be modified upon the application of a gate potential through the capacitor effect.

The field-effect flow control (FEFC) using this electrical modification was first demonstrated in the early 1990s to enhance the separation efficiency while preventing protein adsorption onto the wall in capillary electrophoresis[1]. In 1999, this was then demonstrated in microfluidic networks to control the flow and even reverse the electroosmotic flows in the SiN_x fabricated microchannels by applying a gate potential[22]. Later, glass and polydimethylsiloxane (PDMS) were used to replace the dielectric material as they are more robust and have better flow visualization in the gate region[22]. More recently, it has been applied in nanofluidic channels to modulate the concentration of ions and molecules inside[161].

This mechanism was then used to generate rectified AC electroosmotic flows[35,13,36] by synchronizing the gate potentials with the channel potentials. Compared to DC operated electroosmotic pumping that generally requires very high voltages applied along the channels and sensitive to the pH of the working solution, the electrolysis reaction can be eliminated using AC operation and lower voltages. To distinguish this FEFC method from the traditional AC electroosmosis (ACEO) where the flow is generated by the action of an electric field on its own induced diffuse charge near a polarizable surface and mostly operated at a frequency higher than 1kHz, this rectified AC electroosmotic flow is obtained by synchronization of zeta-potential modulation of the walls of the microchannel with the AC axial driving voltage along the microchannel. Although AC electroosmotic flow has been demonstrated earlier, it has not been fully characterized. In addition, pressure generation using AC electroosmotic effect has not been demonstrated. All the existing work either focus on flow generation on report calculated pressure heads based on experimental observed flow. The objective of this study was to fully characterize the rectified AC electroosmotic flow and investigate the pressure generation using direct measurements.

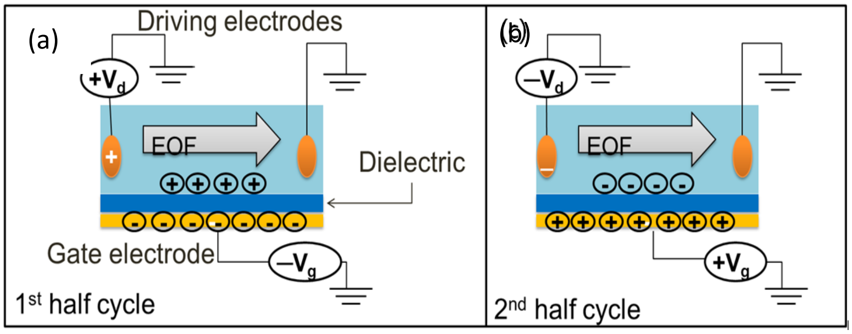

Figure 7-1 (a) At the 1st half cycle, the electroosmotic flow velocity is enhanced over the native state due to the accumulating positive ions near the surface when a positive driving potential and a negative gate potential are applied. (b) At the 2nd half cycle, the electroosmotic flow is reduced or even reversed due to the accumulating negative ions near the surface when a negative driving potential and a positive gate potential are applied.

7.3 Methods

7.3.1 Theory

When a potential is applied across a microchannel, the charges in the double layer induce fluid flow close to the wall surface. The flow velocity U_{EO} near the channel wall can be expressed by the product of electroosmotic mobility μ_{EO} and the local electric field E as

$$\overrightarrow{U_{EO}} = \mu_{EO}\vec{E} = \frac{\varepsilon\xi}{\eta}\vec{E} \tag{1}$$

where ζ is the zeta potential, *ε* is the permittivity and *η* is the viscosity of the working liquid. However, the application of a DC voltage in a local area can lead to gas evolution through electrolysis which changes the local pH and ionic concentrations as well as introduction convection due to formation and release of gas bubbles. The application of an AC potential with simultaneous zeta-potential modulation through a gate electrode at the walls of the microchannel has been shown to induce rectified fluid flow while avoiding gas evolution. The working principle of rectified AC electroosmotic flow is depicted in Figure 7-1. Here a driving potential, which is a symmetric square voltage waveform (V_d), is applied along the axis of the microchannel. Another symmetric square voltage waveform, the gate potential (V_g), is applied on the gate electrode and phase synchronized with the driving voltage. The gate electrode covered the entire microchannel with a dielectric layer on top. The application of a gate potential, causes accumulation of oppositely charged ions in the solution side of the gate dielectric which changes the native charge in the double layer. The proper synchronization of the gate and driving potentials causes a simultaneous change in the axial electric field and the charge in the double layer, producing a rectified body force and thus fluid transport. This is illustrated for the case when the native zeta potential and the charge on the double layer are positive. During the first half cycle, as shown in Figure 7-1(a), the driving potential is positive and the gate potential is negative. The zeta potential of the walls of the microchannel close to the gate electrode is enhanced over its native state since more positive ions are attracted to the surface to balance the charges on the gate electrode. The electroosmotic flow velocity in this half cycle is enhanced over the native state. During the second half cycle, the gate potential is positive, therefore a lesser number of positive ions than in the native state will be attracted to the surface which decreases the zeta potential and reduces the electroosmotic flow velocity. When this positive gate potential is larger than a certain threshold potential, the negative counter ions near the surface can be completely replaced by positive ions which results in a positive zeta potential and reversal of electroosmotic flow. Since the driving electric field is also reversed at this stage, the electroosmotic flow (Equation 1) under an alternating electric field can be rectified by this mechanism, while it would have a net-zero flow rate without the synchronization of the zeta potential modulation.

When the gate electrode is covered with an insulator which interacts with the solution in the microchannel, the zeta potential in the gate region can be controlled by the application of a gate potential. The insulator, the Stern and diffuse double layer can be represented by capacitors. When a square wave AC potential is applied to the gate electrode, the influence of the gate potential on the local zeta potential can be described by[23]

$$\Delta\xi = \frac{C_{insulator}}{C_d} V_g \cdot z(\omega t) \tag{2}$$

where $C_{insulator}$ and C_d are the capacitance of the insulator and electric double layer, and V_g is the gate potential. Also,

$z(\omega t) = 1$ when $\omega t < \pi$

$z(\omega t) = -1$ when $\pi < \omega t < 2\pi$

The capacitance of the insulator is given by

$$C_{insulator} = \frac{\varepsilon_0 \varepsilon_r A}{d_{insulator}} \tag{3}$$

where A is the surface area, $d_{insulator}$ is the thickness of the insulator, and ε_0 and ε_r are the dielectric constant of vacuum and of the solution respectively.

Multiplying Equation (2) by ε/η, the modified electroosmotic mobility μ_{EO} is obtained as

$$\Delta\mu_{EO} = \frac{\varepsilon}{\eta}\Delta\xi = \frac{\varepsilon}{\eta}\frac{C_{insulator}}{C_d}V_g \cdot z(\omega t) \tag{4}$$

When an AC square waveform driving potential V_d is applied along the channel, flow along the channel wall is generated by the native zeta potential of the surface. The flow is propagated to the bulk fluid due to viscous drag. The net flow however is zero, unless the zeta potential is modulated. The net flow rate Q induced by the zeta potential modulation in a microchannel with a length of L, a width of w and a height of h can be expressed as

$$\begin{aligned} Q &= w \cdot h \cdot \Delta\mu_{EO}[E_d \cdot z(\omega t + \phi)] \\ &= w \cdot h \frac{\varepsilon}{\eta}\frac{C_{insulator}}{C_d}\frac{V_g V_d}{L} \cdot z(\omega t) \cdot z(\omega t + \phi) \end{aligned} \tag{5}$$

Here the driving potential V_d has an angular frequency of ω and a phase lag of φ with respect to the gate potential. The influence of the driving potential V_d, gate potential V_g, applied frequency ω, phase lag φ and dielectric constant ε on particle transportation in an AC rectified electroosmotic flow in an microchannel was experimentally determined in this study. From our previous study[36], we found the maximum flow rate Q_{max} happens at $\varphi = 0^0$ while no back pressure is present.

$$Q_{\max} = w \cdot h \frac{\varepsilon}{\eta}\frac{C_{insulator}}{C_d}\frac{V_g V_d}{L} \cdot z^2(\omega t) \tag{6}$$

For pumps operating in the viscous regime of low Reynolds number, the flow rate decreases linearly with the back pressure P according to $\frac{Q}{Q_{\max}} = 1 - \frac{P}{P_{\max}}$ where P_{max} is the pressure at $Q = 0$. Most literature[30,34] used the formula below to convert the maximum flow rate Q_{max} obtained from experiments to the maximum pressure head P_{max} due to various reasons.

$$P_{\max} = Q_{\max} \cdot R \tag{7}$$

where R is the hydraulic resistance of the device. However, this conversion might overestimate the theoretical pressure due to the intrinsic flow dynamics in AC electroosmotic flow operated at high frequencies. Moreover, most literature used either particle image velocimetry which only represents the flow rate at certain plan/depth or the tracking of air/water interface inside the microchannel filled with a single phase fluid. Such velocity measurements assume negligible gravitational and capillary forces which become very important in pressure generation experiments (Figure 7-2). A method to generate adequate pressure to facilitate a direct measurement of the generated pressure head would be able to characterize the capabilities of the AC electroosmotic technique better.

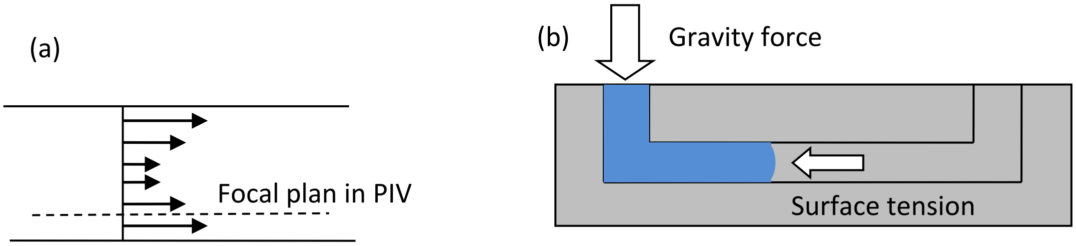

Figure 7-2 Errors in flow rate measurement. (a) Non-uniform flow profile in rectified AC electroosmotic flow; (b) Overestimated flow due to gravity force and underestimated due to surface tension

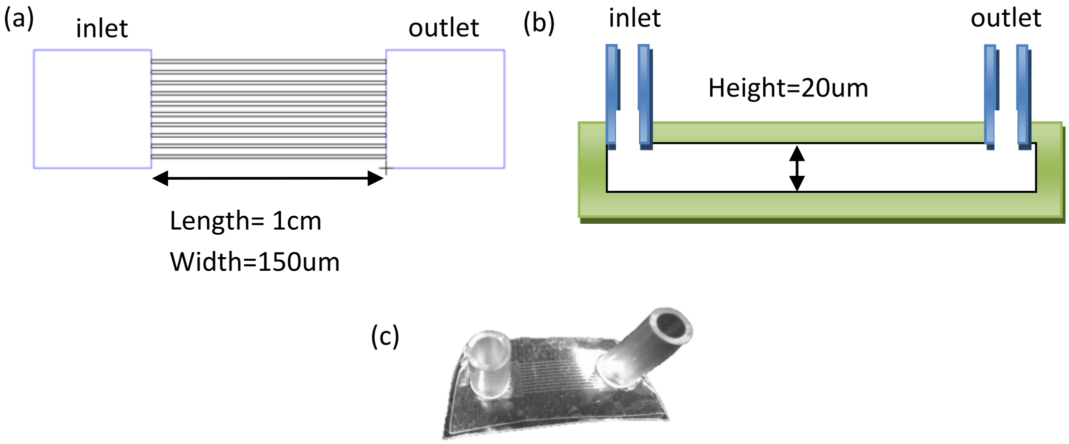

Figure 7-3 Schematic of electroosmotic pumping device (a) top view and (b) side view. (c) the photo of the PU-based microfluidic device

7.3.2 Device fabrication

The electroosmotic pumping device is composited of 10 microchannels in parallel between inlet and outlet as shown in Figure 7-3 and is fabricated using the polyurethane (PU)-based microfabrication process described elsewhere [Chapter6]. Briefly, the moulds were made by SU-8 photoresists through a conventional photolithography process. The PU resin was prepared by dissolving 10 wt% Tecothane® PU pellets in tetrahydrofuran (THF) and then casting on SU-8 molds. The cured thickness of PU film and replica can be estimated as the volume of PU pellets divided by the size of the mold. After the PU was cured, the interconnection using Tygon® tubing was made through a solvent sealing method. This consisted of using THF to partially dissolve the surface to be bonded on the PU replica and the tubing, placing them together and allowing them to dry. A strong bond was formed by fusing the two materials together and no fitting was required. The PU replica with integrated interconnects was then peeled from the mold. Punch tools were used to clean residual PU inside the tubing. The PU replica was then bonded to a flat PU film using solvent sealing method. Both surfaces were solvated by THF which can be spin-coated or dip-coated before placing together. The device was then assembled as the process flow showed in Figure 7-4. Platinum wires were inserted at the inlet and outlet as driving electrodes. The microchannels were then filled with working solution (DI water) by syringe. Either aluminum foil or silver epoxy acted as gate electrode was placed on the outer surface of PU film. Subsequently, a C-clamp is used to apply pressure directly on top of PU film to obtain smaller channel heights while electrodes were connected to the driving and gate power supply. Since the PU channel walls are flexible, the clamping compresses the sidewalls producing a smaller channel cross section.

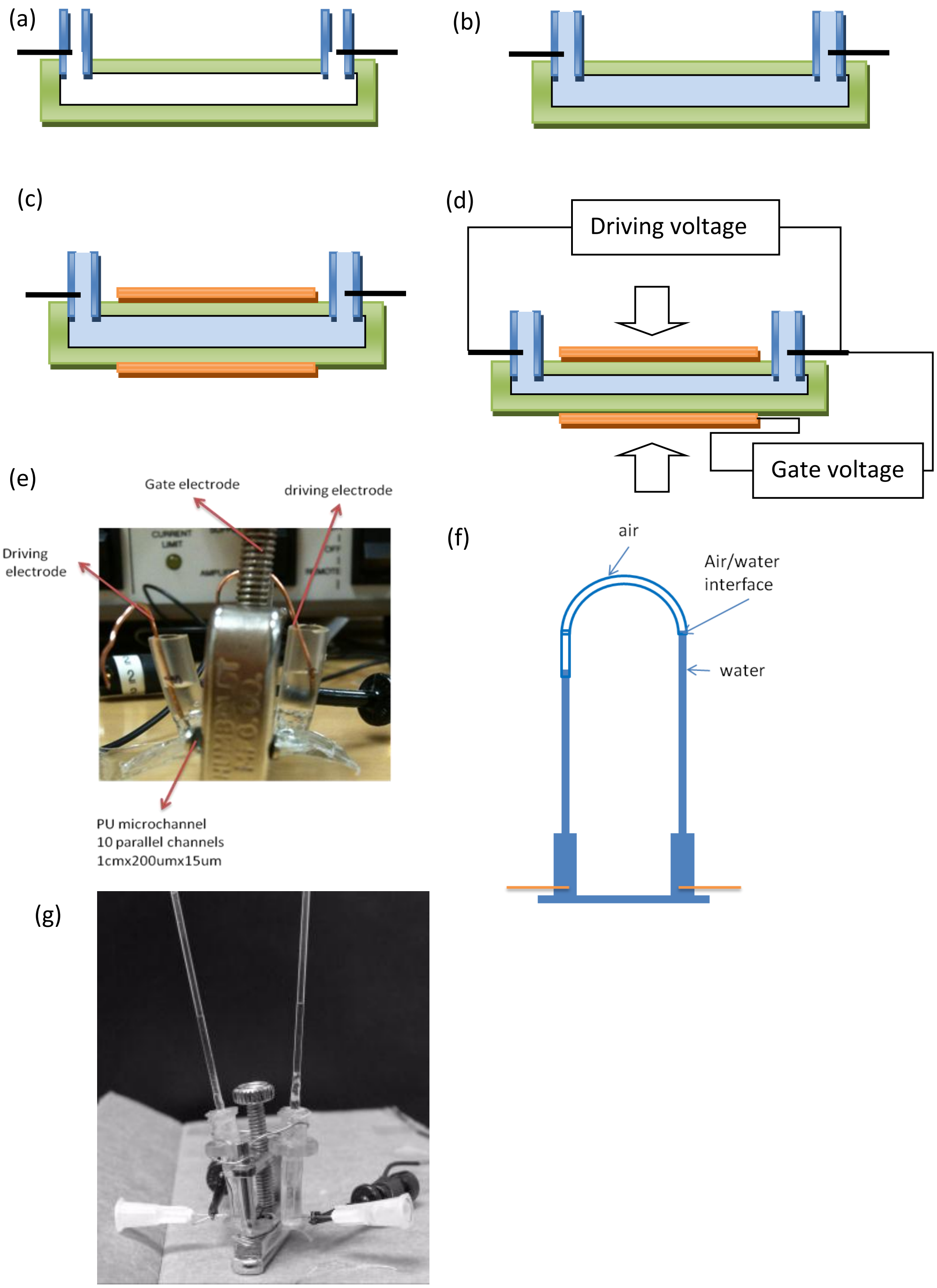

Figure 7-4 Schematic of assembly process (a) insertion of platinum wires as driving electrodes; (b) fill channel with working solution; (c) apply aluminum foil or silver epoxy at the outer surface as gate electrode; (d) use C-clamp to control the channel height and connect electrodes

to power; (e) the appearance of electroosmotic pumping device; (f) setup for flow rate measurement; (g) the rectified AC EOF pumping device with capillary tubes at the inlet and outlet for pressure head measurement.

7.4 Results and discussion

7.4.1 The effective cross-section area of the microchannel

One of the main reasons for using clamps is to facilitate the solution filling process as the hydraulic resistance in smaller channel ($R \propto h^3$) is too high so that it requires a very high pressure held over long period of time to complete the filling process. The initial channel height which is 20μm in this study is large enough to quickly fill the channel. Subsequently, the channel height and its cross section can be reduced by compressing the flexible PU microchannel by a clamp. The reduction in cross section is critical for pressure generation as it does not impede the AC electroosmotic flow while it presents a high hydraulic resistance for the pressure driven back flow due to build up of higher pressure on the outlet side. However, it is not straightforward to determine the channel height and cross section when various levels of clamping force is applied. The determination of the channel height as well as the cross-section area is important to relate the theoretical electroosmotic linear velocity to the experimental volume flow rate obtained. Therefore, a method was developed first to estimate the effective cross-section area of the microchannel based on the DC electroosmotic flow rate. The DC electroosmotic flow rate can be measured directly from the air/water interface movement in external tubing. The assumption here is the electroosmotic mobility, which mostly depends on the solid/liquid interface (polyurethane and DI water here respectively), should be independent from the channel size. Therefore, the effective cross-section area A_{eff} can be calculated from the empirical volume flow rate $Q_{empirical}$ divided by the theoretical electroosmotic velocity U_{EO} shown in the formula below.

$$A_{eff} = \frac{Q_{empirical}}{U_{EO}} = \frac{Q_{empirical}}{\mu_{EO\_empirical} \cdot E} \tag{8}$$

The electroosmotic mobility of DI water (pH7) in the PU-based microfluidic channel is found to be 2.4×10^{-8} m^2/Vs from our previous study[36]. Four distinct settings of clamping and their corresponding DC electroosmotic flows were investigated using Equation (8), their effective cross-sections computed. In addition, the PU microchannels in those settings were frozen in liquid nitrogen to make them rigid, sectioned and the cross sections observed under the SEM. The results of both the computation and experimental observation are presented in Figure 7-5. Figure 7-6 shows the cross section of the channel prior and after clamping. It can be seen that the while the width of the channel remains almost the same (2.7% reduction) the height has reduced significantly

(30% reduction). The sidewalls of the compressed channels are no longer straight and seem to be tilted in order to accommodate the reduction in height. The uniformity of the cross-section area along the channel had been investigated through the SEM images at various locations along the channels as shown in Figure 7-7. The results showed a variation of 1.6% in cross-section area among 4 samples, and validate that this method of using electroosmotic flow rates is capable to determine the cross-section areas in microfluidic channels for the characterization of flow rate and pressure in the following experiments.

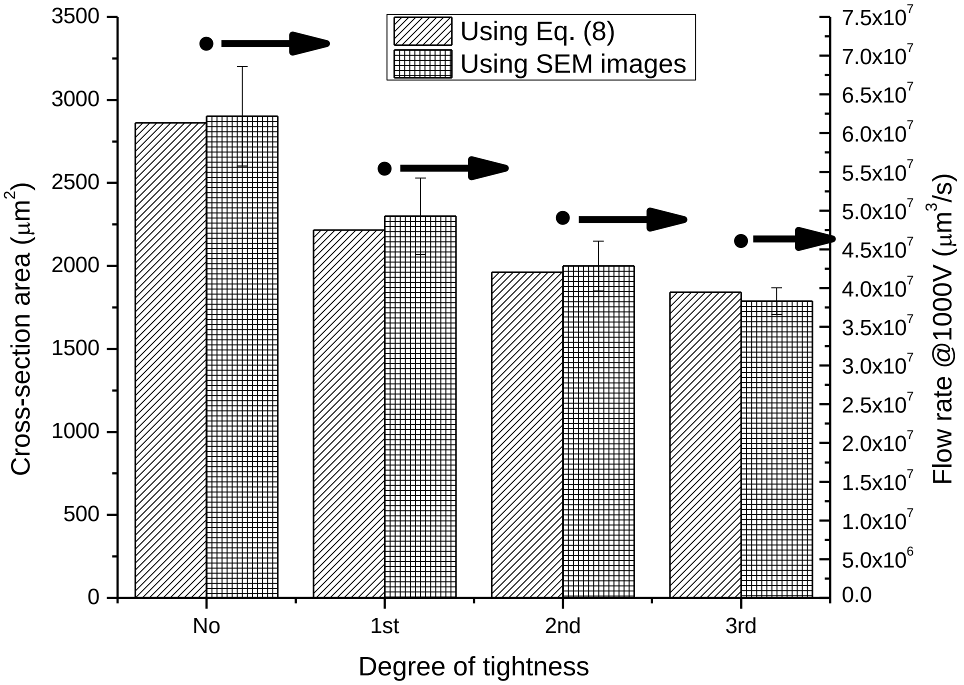

Figure 7-5 The effective cross-section areas of the microchannels under different degrees of tightness of clamping and their corresponding flow rates

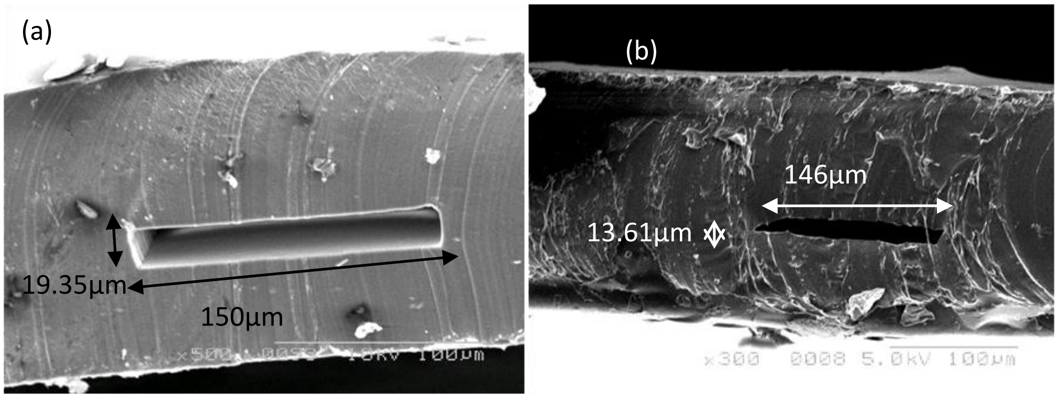

Figure 7-6 SEM photo of the channel cross-section before clamping (a) and after clamping (b)

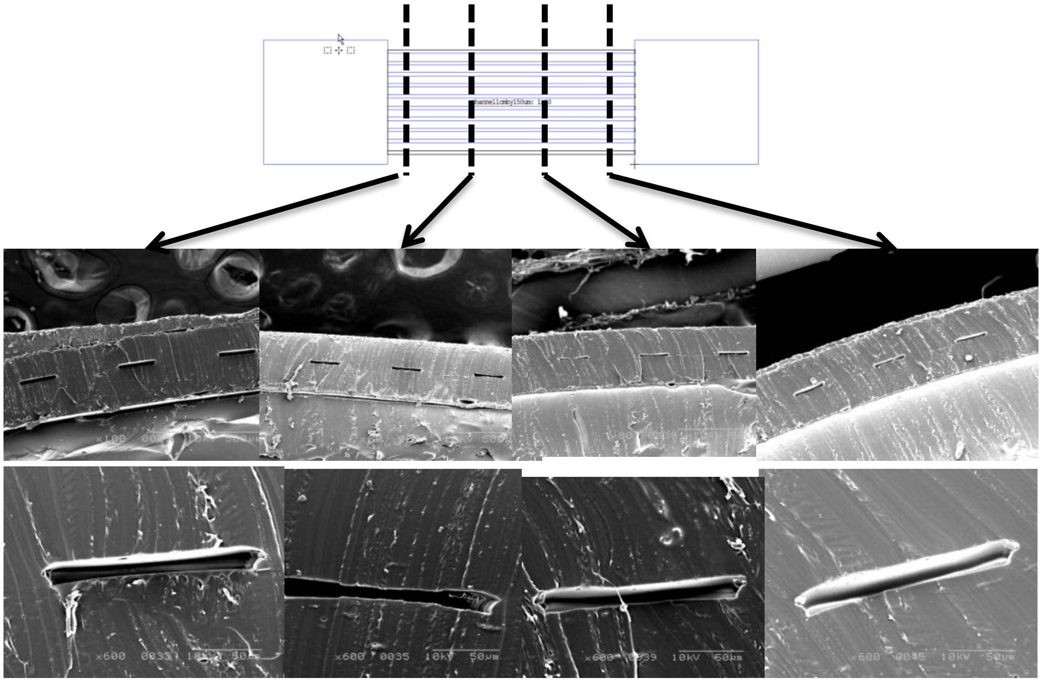

Figure 7-7 SEM photos of the cross-section views at various locations along the channel after being clamped

7.4.2 Flow rate characterization

After developing a method to characterize the cross sectional area of the clamped channel, flow rates produced by rectified AC electroosmotic pumping under various channel cross sections and field conditions were characterized. First, the effect of the cross sectional area on the effectiveness of flow generation was characterized. In this experiment, the electrical potential was kept at 1300V for the DC electroosmotic flow in order to generate significant flow for visualization. For the rectified AC electroosmotic flow a 1Hz square waveform signal with 50% duty cycle, and 1300V amplitude for both driving and gate potentials was applied. Prior to the measurement, the pressure head between inlet and outlet was adjusted to be zero. As seen in Figure 7-8, the flow rate increases for both DC and rectified AC electroosmosis, when the cross section as increases. This increase in flow rate can be explained by equation (5). It can also be observed that the AC electroosmotic flow produced significantly, smaller flow rate (by a factor of ~ 10) as compared to DC electroosmosis at the same amplitude. From the 2nd term of equation (6) in Chapter 3, the underperformance of the AC electroosmotic flow could be due to the low value of (C_{PU}/C_d) and can be improved by either a thinner PU dielectric layer or higher potential applied on gate electrode. However, it was observed that application of DC voltage at 1300V produced significant net gas evolution at the electrodes which led to bubble formation. Large bubbles were clearly visible at the outlet ~ 30 min in operation (Figure 7-9). The AC electroosmotic signal did not generate any observable gas bubbles even after 5 hrs of operation.

Next, the effect of applied frequency was characterized using an AC square-waveform signal with 1300V magnitude and varying the frequency from 1 to 50Hz for various channel sizes. The electroosmotic flow depends on the electric double layer (EDL) built up at the channel wall, and this EDL essentially acts like a capacitor. This particular charging mechanism is typically referred to as capacitive charging. When the applied frequency approaches the inverse of RC time constant, the charging effect in electric double layer becomes rate limiting, and this imposes a limitation on applicable frequency. Here we found that the flow rates decrease as the frequency increases and the flow rate still depends on the channel size as shown in Figure 7-10.

The variation of the flow rates with the driving and gate potential for a symmetric square signal with a frequency of 1Hz is shown in Figure 7-11. The gate potential is equal to the driving potential since they are simply connected together. The applied potential was varied from 1000 to 1300V. It shows that the flow rate increases with the applied potential as expected from equation (5).

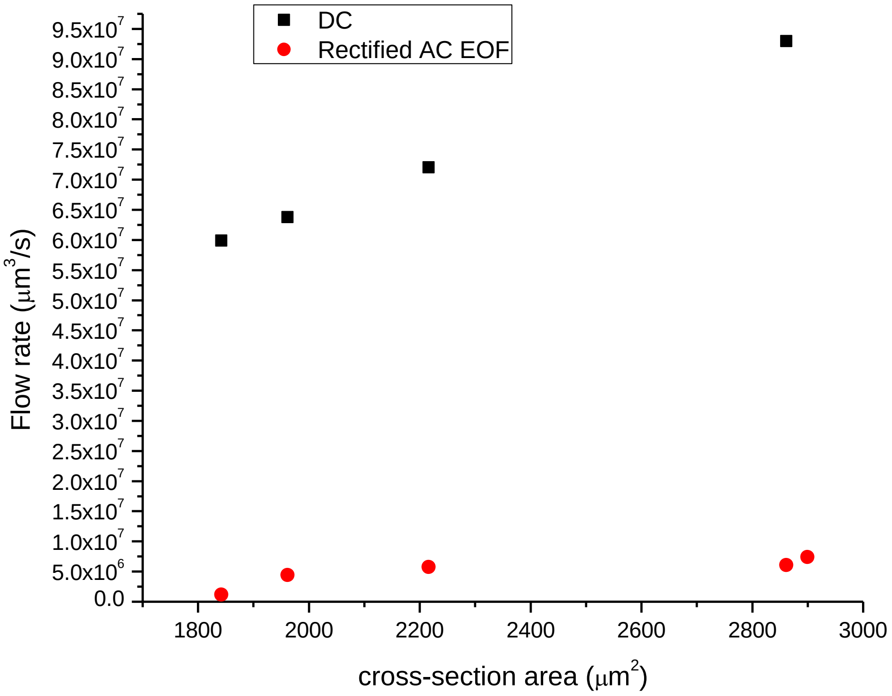

Figure 7-8 The comparison of the flow rates between 1300V DC EOF and 1Hz 1300V AC EOF in various sizes of the microfluidic channels.

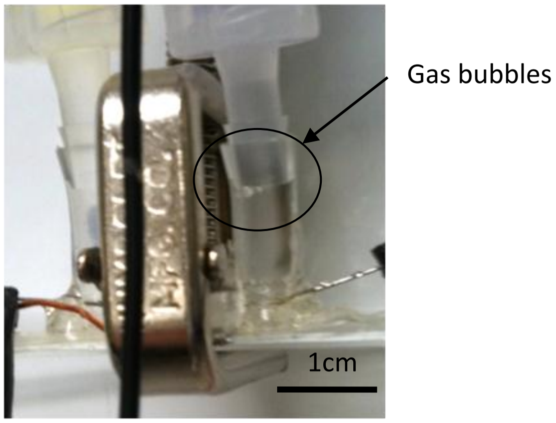

Figure 7-9 The gas bubble generated from the driving electrode was then floated to the corner between tubing and connector after 0.5hr operation in DC electroosmotic mode

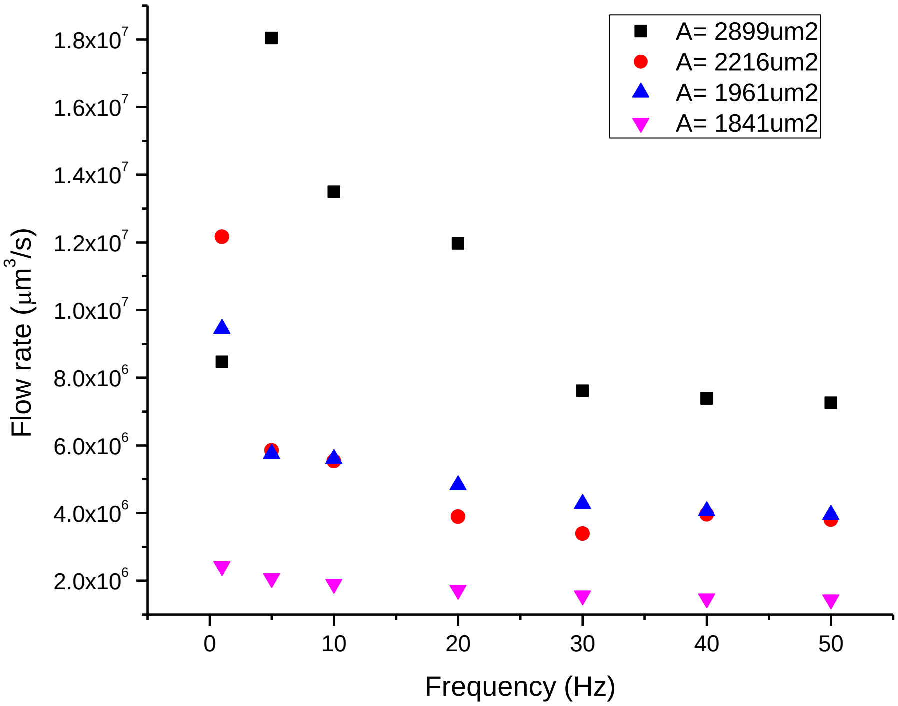

Figure 7-10 Effect of the applied frequency on the flow rates of rectified AC electroosmotic flow when the driving and gate potentials were kept at 1300V with square waveforms

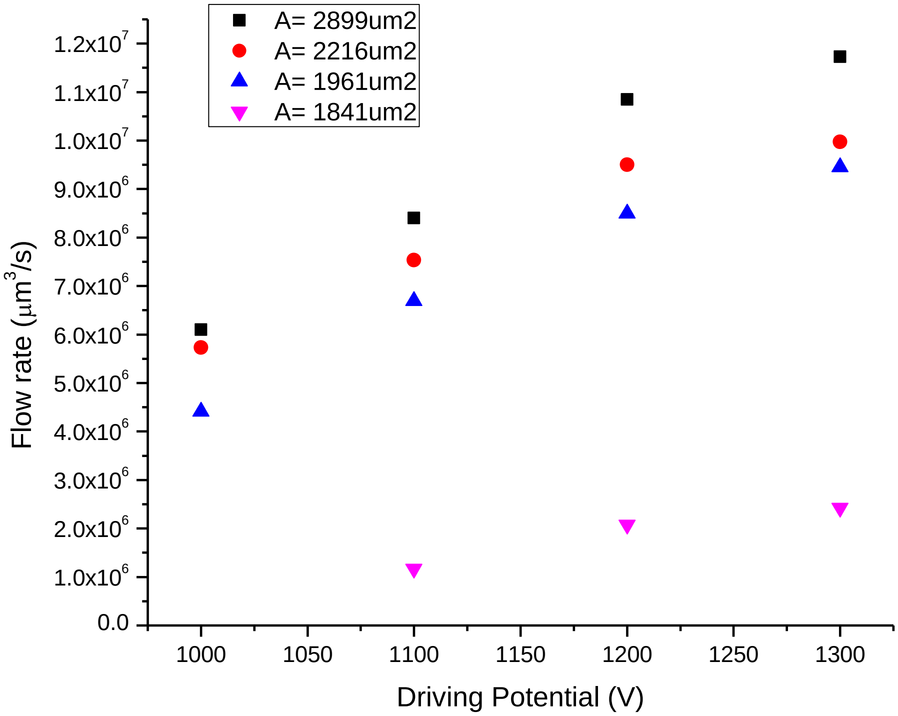

Figure 7-11 Effect of the applied voltage on the flow rates of rectified AC electroosmotic flow when the frequency was kept at 1Hz

A series of experiments were performed to further investigate the effect of the driving potential, gate potential, phase lag between them, and the thickness of dielectric layer. The results showed the flow rate of the rectified AC EOF increases with the driving and gate potentials as shown in Figure 7-12(a) and (b). This behaviour matches the linear response for flow rates versus driving and gate potentials that are described in equation (5). The effect of phase lag between the driving voltage and the gate voltage provide an elegant way to modulate the synchronization of the two voltages. The phase lag was varied between -180° and 180° and its effect on the flow rate shown in Figure 7-12(c). It can be seen that when the phase lag is equal to -180° and 180°, the flow rate will be the highest. When the phase lag approaches -90° and 90°, the flow stops. Finally, when phase lag is 0°, the flow rate is the lowest as predicted in equation (5). There was no time delay between the flow rate and the applied signal when the phase lag changed from -180° to 180°. As dicussed in equation (3), a dielectric layer with thinner thickness $d_{insulator}$ makes the gate potential more effective and results in a faster flow rate under the same condition which can be observed in Figure 7-12(d) by comparing 25 µm and 50 µm thick dielectric layers.

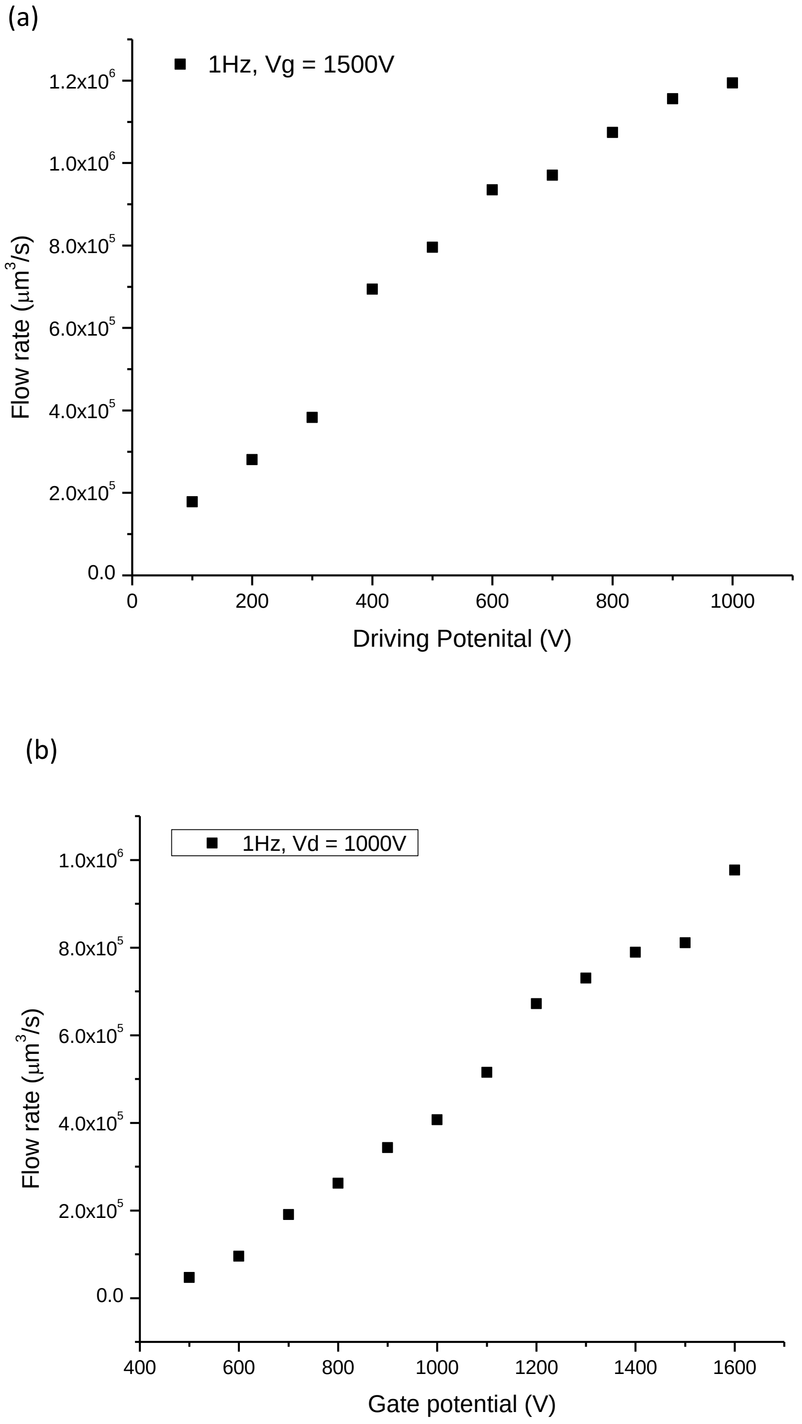

(c)

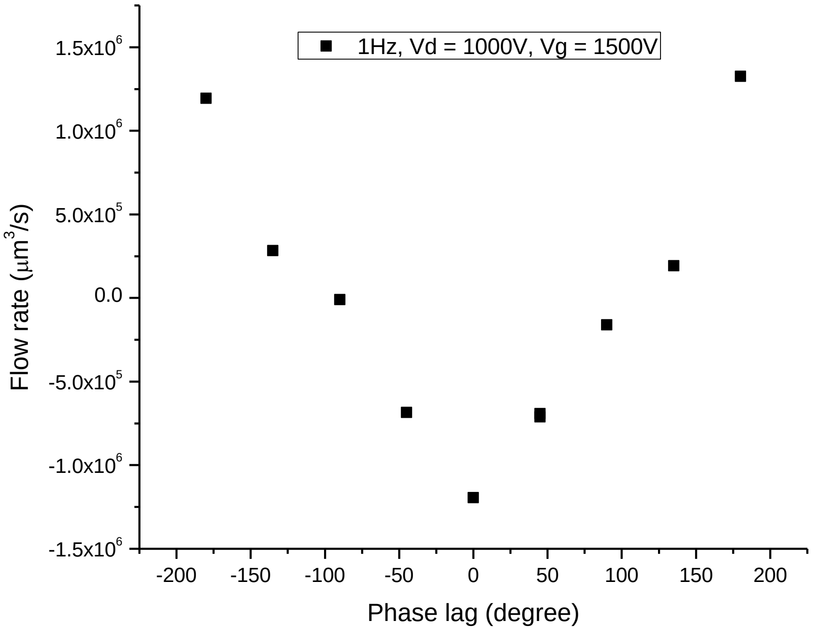

(d)

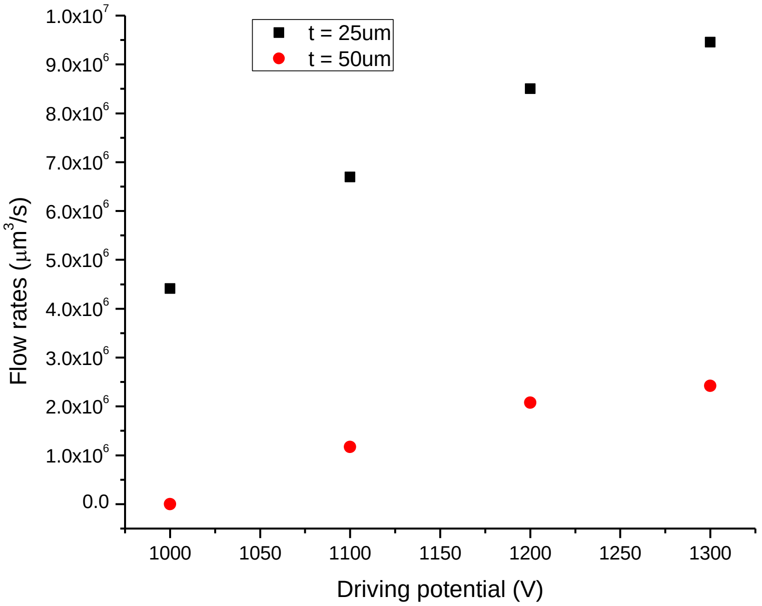

Figure 7-12 (a) Effect of the driving potential on the flow rate of the rectified AC EOF where a 1Hz square-waveform signal was applied and the gate potential was kept at 1500V. (b) Effect of

the gate potential on the flow rate where a 1Hz square-waveform signal was applied and the driving potential was kept at 1000V. (c) Effect of the phase lag between the driving and gate potentials on the flow rates when the driving and gate potentials were kept at 1000V and 1500V respectively. (d) Effect of the thickness of the dielectric layer on the flow rate where a 1Hz square-waveform signal was applied and the gate potential was kept at 1500V

7.4.3 Pressure head characterization

After establishing the flow characteristics generated by the pump under various operating conditions, the pressure generating capability was tested. Various techniques were used to estimate the pressure generated. Hydrostatic height difference between the inlet and the outlet reservoirs was used to measure pressure differences up to 1 kPa. Pressure sensor connected to a blocked outlet was used for higher pressures. In addition, another technique which uses the compression of air trapped in a confined space to estimate pressure using ideal gas law was also used. Since static pressure is determined by the density and the height, the height difference is commonly used for pressure measurement. While being the most straight-forward, its major disadvantage is it takes a long time for the pump to achieve the maximum pressure output. EO pumps that generate high pressure usually require small microchannels to be able to resist the back pressure. However, small microchannels generate slow EOF that can be found in the previous experimental results. For instance, the maximum flow rate can be generated from the rectified AC EOF device with the smallest channel (cross-section area = 1841 μm^2) is only 2×10^6 $\mu m^3/s$. It could take half day to fill up the volume and reach the maximum pressure output. The Boyle's law, which describes the inversely proportional relationship between the absolute pressure and volume of a gas at constant temperature within a closed system, can be used for measuring pressure in microfluidic devices more rapidly. As the fluid is pumped the volume of the confined space reduces and its pressure increases. However, in this technique the measurement of the displacement of the meniscus is critical in estimating the pressure. Alternatively, a pressure gauge can be connected to the outlet of the pumping device directly. Here again, the large volumetric flows are not reduced to obtain the maximum pressure. These three techniques for pressure measurement were compared to each other under the same conditions of 1Hz, 5Hz and 10Hz square-waveform signals with the driving potential of 1000V and the gate potential of 1500V. Similar results were obtained as shown in Figure 7-13. It can be seen that the hydrostatic height difference method produces consistently lower reading even after 7 hrs of operation as expected as the pressure head approaches the maximum pressure asymptotically. It can also been seen that the pressure sensor reading shows higher variance below 1kPa. This is because the pressure gauge (Omega PX273-300DI) used is a wide range sensor (0 to 2MPa) and has a sensitivity of 259kPa/V and causes errors of the measurement at 10Hz. Although the investigation of the pressure generation on the DC EOF have been studied before, however these are, to the authors' knowledge, the first investigation on the pressure generation of the rectified AC EOF using direct measurements instead of converting the maximum flow rates. The maximum pressure output from this device is 2.7kPa when square-waveform signals with the driving potential of 1000V and the gate potential of 1500V are applied. No bubble can be visually observed during the operation (7 hrs).

For most biomedical application, it usually requires buffered solution as working fluid. Here a 0.1mM phosphate buffered solution (PBS) is tested against the DI water. The results in Figure 7-14 show the buffered solution can still be working fluid however the pressure output decreases due to its higher ionic strength.

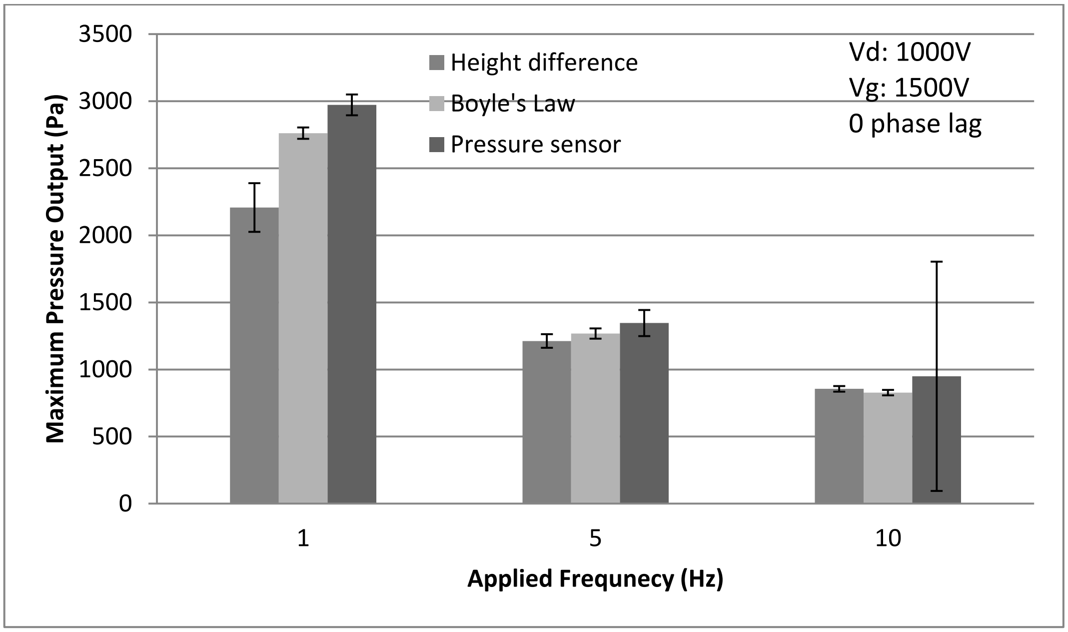

Figure 7-13 Maximum pressures from the rectified AC EOF pumping devices measured as a function of applied frequency using various direct measurement mothods.

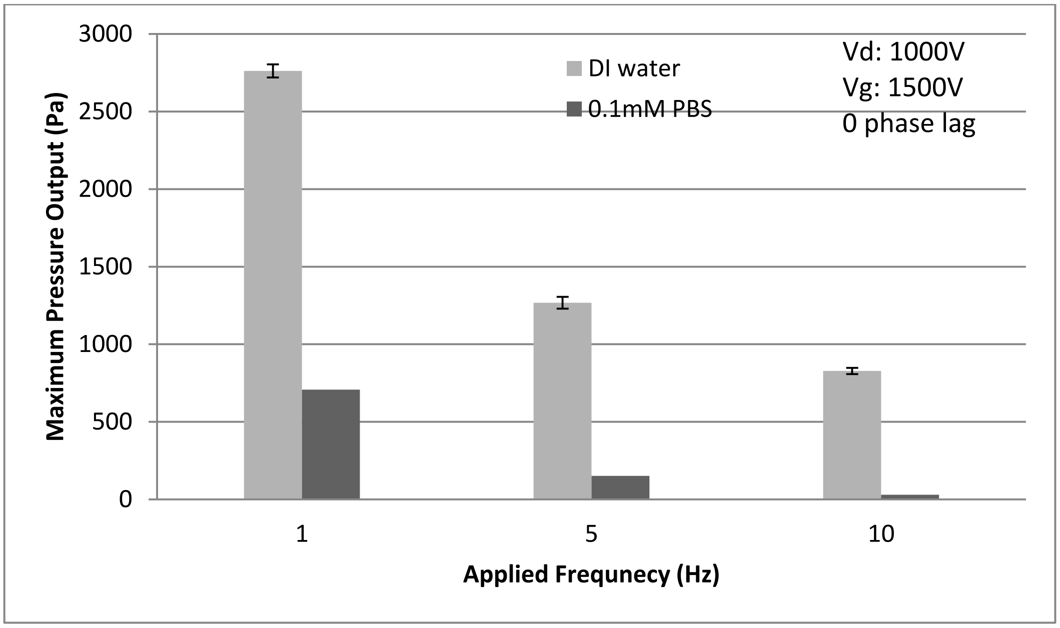

Figure 7-14 Maximum pressures from the rectified AC EOF pumping devices with the DI water and 0.1mM PBS as the working solution.

7.5 Conclusion

The first demonstration of the pressure generation from the rectified AC EOF pumping device is presented, and the result shows the maximum pressures of 2.7kPa is obtained on a microfluidic pump. The clamped microfluidic channels facilitate the filling process and provide the control over the size of microfluidic channel. The effects of driving potential, gate potential, applied frequency, phase lag and dielectric layer on the flow rates were characterized. The pressure generation assessed by three methods provides the creditability of the experimental results. Although the performance of the rectified AC EOF cannot complete with that of DC EOF, however it provides more approaches to adjust the flow rate and pressure output while eliminating electrolysis problems.

Chapter 8 Summary and Recommendations for Future Work

8.1 Summary of Thesis Work

Bubble generation due to application of potential greater than the gas evolution potential is a major problem with conventional electroosmotic (EO) pumping and prevents the integration of electrodes inside microchannels for local flow control in lab on chip applications. In this study we present the use of zeta potential modulation synchronized with AC driving voltage to obtain rectified unidirectional EO flow, while eliminating water electrolysis at the same time.

Since the electric field applied is unsteady, the body force produced and therefore the flow induced is also unsteady but periodic. In order to understand the fluid dynamics under unsteady conditions and study the link between the electric field, body force and the fluid velocity produced, it is critical to visualize the flow with high spatial and temporal resolutions. A phase-sampling method using conventional micro particle image velocimetry (PIV) for forced periodic flows was developed to investigate the AC electroosmotic flows. In this technique, each velocimetry data set from laser pulses represents a unique point in phase for a periodic flow. The flow characteristics over a single cycle can be reconstructed from these unique points obtained over larger timeframe spanning a number of cycles, thus allowing measurement at higher temporal resolutions. Without upgrading to the costly high-speed equipment, this technique can be used to measure the flow variation of the rectified AC electroosmotic flows and characterize its flow response upon the electrical potential is applied. This flow information could be helpful in order to obtain the optimum performance by choosing proper operation conditions and device design. Moreover, this technique can be applied for any forced periodic flow with high operation frequency.

With the ability to characterize the flows, the first application of using the rectified AC electroosmotic flow is to transport particles, cells, and other micro organisms. Both neutral and charged particles in various sizes were able to be transported. The effects of dielectric layer, driving electric field, gate potential, applied frequency, and phase lag between the driving and gate signals on the particle velocities were determined. Each parameter can be used independently to control the transportation of the particles. Our work shows that both of driving electric field and gate potential can increase the particle velocity efficiently. The experimental results also suggest a higher frequency can be chosen to avoid electrolysis without an adverse effect on the particle velocity. Besides, the phase lag between driving and gate potentials can be used to modulate the particle velocity and even reverse the particle movement without changing other parameters, which could be beneficial in precise positioning. The benefits of such device can be a low-cost alternative to optical tweezers in certain applications.

In order to develop the electroosmotic pumping devices to deliver pressure output, the cross-section area of the microchannel needs to be as small as enough ($h < 10$ µm) in order to hold the back pressure. However, it is challenge to prime the PDMS microchannels as it is hydrophobic and repels water. Moreover, its intrinsic hydrophobic nature causes significant protein adsorption from protein-containing fluids and impedes its usage in biomedical applications. To solve the problems, a more hydrophilic and biocompatible material, polyurethane (PU), was chosen to replace PDMS. Two new fabrication processes for making thin, transparent, flexible polyurethane (PU)-based microfluidic devices. We give details not only on the fabrication of microchannels but also their bonding, and the integration of fluidic interconnections as well as surface modification with hydrophilic polyethylene oxide (PEO) to improve their biocompatibility. Using these processes, microchannels were produced with high transparency (96% that of glass in visible light), high bond-strength (326.4kPa) and low protein adsorption (80% reduction in fibrinogen adsorption vs. PDMS), which is critical for non-fouling and prevention of thrombosis. Our findings indicate that PEO modified PU could serve as an effective alternative to PDMS in many blood contacting microfluidic applications. An in-situ surface modification method was also successfully demonstrated to graft PEO to PU inside the moulded and sealed microfluidic devices.

Finally, a PU-based electroosmotic pumping device using zeta potential modulation was developed and it is capable of running under high back pressures. The rectified flow is obtained by synchronous zeta-potential modulation with the driving potential in the microchannel. The flow rate and pressure output can be controlled through several parameters like the driving potential, gate potential, applied frequency, and phase lag between the driving and gate potentials. Direct measurements of the pressure generation without using flow rate conversion which has been found in most previous literature are investigated. We had successfully demonstrated the pressure generation using pressure head measurement, and showed the maximum pressures of 2.7kPa can be obtained from the rectified AC electroosmotic pumping device.

8.2 Research Contributions

My research contributions are divided into several areas that include the development for:

- Periodic flow characterization using micro particle image velocimety

Without upgrading to the costly high-speed equipment, the phase-sampling technique we developed in this study can be used to measure the flow variation and characterize their flow responses for any forced periodic flows with a high operation frequency (> laser pulse repetition rate). The sampling resolution can be as low as 20 20 µs for 100Hz periodic flows with sufficient number of dataset, and a resolution of 200 µs was obtained in the experiment using 40 sets of velocimetry results that only took <10 sec for laser to collect the results. Compared to the existing phase-locking technique that is more difficult, time-consuming, multi-experiment method in order to control the stroboscopic instance using series of time delays, this technique can become a useful tool of flow measurement for any forced periodic flows.

- Particle transportation

A number of methods have been developed to transport particles and cells in closed channels using pressure-driven flow, electrokinetics, electroosmosis, electrowetting, and dielectrophoresis. Most of these methods are only applicable in closed microchannels and cell transportation in open microfluidic devices is seldom reported. Open microchannels have their top side open to the ambient air and can provide advantages like maintaining the physiological conditions for normal cell growth and for introducing accurate amounts of chemicals and biological materials. Currently, the use of optical tweezers is the mainstream method to manipulate particles and cells in open plates and microchannels. However, it requires complex optical setups and expensive lens systems that limit their widespread use. In this study, the use of this rectified AC electroosmotic flow to transport both neutral and charged particles of various sizes in an open microchannel is successfully demonstrated to potentially achieve the core functionality of optical tweezers in particle manipulation without its associated high cost.

- Polyurethane-based soft-lithography microfabrication

PDMS's intrinsic hydrophobic nature causes significant protein adsorption from protein-containing fluids. Although a number of attempts have been made to reduce protein adsorption on PDMS surfaces and microchannels, some modifications are temporary and the surface was found to ultimately revert back to the hydrophobic while some based on covalent attachment of surface groups through chemical modification tends to swell PDMS due to the use of organic solvents. In this study, we developed a method for fabrication of polyurethane similar to methods used for PDMS but leading to devices having hydrophilic interior surfaces. We also developed several effective bonding and interconnection methods for solvent cast PU microfluidic networks to produce PU elastomeric devices that could be rapidly prototyped. An in-situ surface modification method to graft PEO to PU surfaces in the interior of moulded and sealed microfluidic channels is also developed to increase its resistance to biofouling.

- Pressure generation of rectified AC electroosmotic flows

Although the rectified AC electroosmotic flows have been used for flow generation widely, its capability of pressure generation is not clear as most literature had focused on the investigation of the effectiveness of the gate potential and the flow characterization on the rectified AC electroosmotic flows. Their pressures were estimated from the maximum flow rate can be obtained from the microchannels and no direct measurement has been demonstrated yet. In this study, a microfluidic pump using rectified AC electroosmotic flow is first developed to generate pressure, and its flow rate and pressure output can be controlled through several parameters like the driving potential, gate potential, applied frequency, and phase lag between the driving and gate potentials. Then direct measurements of the pressure generation using pressure heads, pressure sensors and Boyle's law are presented to increase their creditability. Although the results show the performance of rectified AC EOF cannot complete with that of DC EOF, it provides more approaches to adjust the flow rate and pressure output while eliminating electrolysis problems.

8.3 Recommendations for Future Work

More work on the characterization of AC EOF operated in higher frequencies should be carried out as electrolysis and bubble generation could be happened without notice and affect the accuracy of the measurement. A higher operating frequency can totally avoid the electrolysis, but as the frequency goes higher it approaches the transient regime. More understanding of transient behaviours needs to be done to investigate the frequency limit. The maximum operating frequency that can be achieved depends on the charging dynamics of the EDL and the time needed for the EOF to become established by viscous coupling. The charging of the EDL upon application of a gate potential is limited by the current, which depends on the series impedance of the gate insulation capacitance and the channel electrolyte resistance. A further study need to be done to investigate the transient state thus the optimum operation frequency can be determined to achieve either high flow rate or high pressure.

More study on finding the most suitable working solution for the rectified AC electroosmotic flow. While DC electroosmotic pumping requires an absolutely high zeta potential present at the solid/liquid interface in order to generate a faster flow or higher pressure in the microchannel, the rectified AC electroosmotic flow does not. Instead, it requires a working solution which provides a more effective variation in electroosmotic mobility under gate potential. Solvent-based liquids should have larger variations in electroosmotic mobility (or zeta potential) under the gate voltage effect, since the effect of the gate voltage on the EOF scales inversely proportional to the dielectric constant of the solution, however their compatibility with the channel materials needs to be investigated. For cases that need biological buffers as working solutions, low conductivity buffers such as tris(hydroxymethyl)aminomethane (Tris) need to be investigated to avoid electrolysis while maintaining the pumping efficiency.

For applications with high pressure generation, a solid/liquid interface which provides a small Debye length λ_D allows high-pressure performance without reducing the flow rate according to the equation below.

$$\Delta P_{max,EO} = \frac{8\varepsilon\zeta E_z l}{a^2} f(\frac{a}{\lambda_D})$$

Here *a is the radius of channel* and *l is the length*, ε is the electrical permittivity, ζ is the zeta potential, E_z is the applied electric field, λ_D is the Debye length and *f(a/* λ_D*)* approaches unity when a>> λ_D. However, decreasing λ_D by increasing ion density also increases the ionic current through the pump and thereby induces bubble generation and lowers thermodynamic efficiency. A further study on the working solution is necessary to obtain the optimum flow and pressure outputs.

AC electroosmotic pumps with multi-stage configuration in serial have the advantage of using lower driving voltage while generating a higher output pressure. Using the zeta potential modulation prevents the reversing flow between stages and reduces the total length of the channels, allowing more stages to be incorporated in the same footprint, increasing the flow rate and the pressure as well. Although several attempts had been made in this study, the devices were not successful due to the detachment of dielectric layer around the driving electrode. This problem should be solved by a dielectric layer with better adhesion such as chemical-vapour-deposition (CVD) silicon oxide or silicon nitride.

For the phase sampling technique in particle image velocimetry, the highest temporal resolution using this technique relies on the frequency of the laser pulse, therefore more work on the characterization of laser pulse timing needs to be carried out to ensure the accuracy. Moreover, a higher sampling rate A/D converter (>10k Samples per second) would be helpful in order to obtain more accurate results for periodic flows with even higher frequencies.

For the particle transportation, two axial configuration with two pairs of electrodes placed orthogonally need to be accomplished to generate flows that can transport and position samples on a planar platform. Moreover, an intensive study on using biological buffers as working solutions need to be carried out in order to optimize the applied voltages and the moving speed of the samples.

For the PU-based microfabrication process, the PEO modified PU surface might not be fully blood-compatible. A further modification using antithrombin-heparin (ATH) complex which has demonstrated potential as an anticoagulant surface modifier should be implemented to strengthen its biocompatibility. Moreover, different surface modifications on PU surface should be explored since PU has the ability to be chemically tailored for a specific application.

References

1. Lee, C.S., Blanchard, W.C. & Wu, C.T. Direct control of the electroosmosis in capillary zone electrophoresis by using an external electric field. *Analytical Chemistry* **62**, 1550-1552 (1990).

2. Pertsov, A.V. & Zaitseva, E.A. Discovery of Electrokinetic Phenomena. *Moscow* (2008).

3. Karniadakis, G., Beşkök, A. & Aluru, N.R. *Microflows and Nanoflows: Fundamentals and Simulaiton*. (Springer: 2005).

4. Masliyah, J.H. & Bhattacharjee, S. *Electrokinetic and Colloid Transport Phenomena*. 736 (Wiley-Interscience: 2006).at <http://www.amazon.com/Electrokinetic-Colloid-Transport-Phenomena-Masliyah/dp/0471788821>

5. Kaspar, J. Zur Theorie der elektrolytischen Doppelschicht und der potentialbestimmenden Ionenadsorption. *Helvetica Chimica Acta* **21**, 650-663 (1938).

6. *Microsystem Engineering of Lab-on-a-Chip Devices*. 297 (Wiley-VCH: 2008).at <http://www.amazon.com/Microsystem-Engineering-Lab-Chip-Devices/dp/3527319425>

7. Theeuwes, F. Elementary osmotic pump. *Journal of pharmaceutical sciences* **64**, 1987-91 (1975).

8. Gan, W.E. *et al.* Mechanism of porous core electroosmotic pump flow injection system and its application to determination of chromium(VI) in waste-water. *Talanta* **51**, 667-75 (2000).

9. Chen, L. Fabrication and characterization of a multi-stage electroosmotic pump for liquid delivery. *Sensors and Actuators B: Chemical* **104**, 117-123 (2005).

10. Mikkelsen, J.C. & Santiago, J.G. Fabrication and characterization of electrokinetic micro pumps. *ITHERM 2000. The Seventh Intersociety Conference on Thermal and Thermomechanical Phenomena in Electronic Systems (Cat. No.00CH37069)* 31-36doi:10.1109/ITHERM.2000.866167

11. Takamura, Y. *et al.* Low-voltage electroosmosis pump for stand-alone microfluidics devices. *Electrophoresis* **24**, 185-92 (2003).

12. Brask, A., Snakenborg, D., Kutter, J.P. & Bruus, H. AC electroosmotic pump with bubble-free palladium electrodes and rectifying polymer membrane valves. *Lab on a chip* **6**, 280-8 (2006).

13. Mutlu, S., Svec, F., Mastrangelo, C.H., Frechet, J.M.J. & Gianchandani, Y.B. Enhanced electro-osmotic pumping with liquid bridge and field effect flow rectification. *17th IEEE International Conference on Micro Electro Mechanical Systems. Maastricht MEMS 2004 Technical Digest* 850-853 (2004).doi:10.1109/MEMS.2004.1290720

14. Brask, A., Kutter, J.P. & Bruus, H. Long-term stable electroosmotic pump with ion exchange membranes. *Lab on a chip* **5**, 730-8 (2005).

15. Selvaganapathy, P., Renaud, P. & Mastrangelo, C.H. Bubble-free electrokinetic pumping. *Journal of Microelectromechanical Systems* **11**, 448-453 (2002).

16. Studer, V., Pepin, A., Chen, Y. & Ajdari, A. An integrated AC electrokinetic pump in a microfluidic loop for fast and tunable flow control. *The Analyst* **129**, 944-9 (2004).

17. Ramos, A., Morgan, H., Green, N.G., González, A. & Castellanos, A. Pumping of liquids with traveling-wave electroosmosis. *Journal of Applied Physics* **97**, 084906 (2005).

18. Lee, C.S., McManigill, D., Wu, C.T. & Patel, B. Factors affecting direct control of electroosmosis using an external electric field in capillary electrophoresis. *Analytical Chemistry* **63**, 1519-1523 (1991).

19. Ghowsi, K. & Gale, R.J. Field effect electroosmosis. *Journal of Chromatography A* **559**, 95-101 (1991).

20. Hayes, M.A., Kheterpal, I. & Ewing, A.G. Effects of buffer pH on electroosmotic flow control by an applied radial voltage for capillary zone electrophoresis. *Analytical chemistry* **65**, 27–31 (1993).

21. Hayes, M.A. Extension of External Voltage Control of Electroosmosis to High-pH Buffers. **71**, 3793-3798 (1999).

22. Schasfoort, R.B. Field-Effect Flow Control for Microfabricated Fluidic Networks. *Science* **286**, 942-945 (1999).

23. Mcmanigill, D. Factors Affecting Direct Control of Electroosmosis Using an External Electric Field in Capillary Electrophoresis. *Society* **1523**, 1519-1523 (1991).

24. Hunter, R. *Zeta potential in colloid science : principles and applications*. (Academic Press: London ;;New York, 1981).at <http://www.worldcat.org/title/zeta-potential-in-colloid-science-principles-and-applications/oclc/8066651>

25. Lee, J.N., Park, C. & Whitesides, G.M. Solvent Compatibility of Poly(dimethylsiloxane)-Based Microfluidic Devices. *Analytical Chemistry* **75**, 6544-6554 (2003).

26. Ho, C.-M. & Tai, Y.-C. MICRO-ELECTRO-MECHANICAL-SYSTEMS (MEMS) AND FLUID FLOWS. *Annual Review of Fluid Mechanics* **30**, 579-612 (1998).

27. Jacobson, S.C., McKnight, T.E. & Ramsey, J.M. Microfluidic Devices for Electrokinetically Driven Parallel and Serial Mixing. *Analytical Chemistry* **71**, 4455-4459 (1999).

28. Pollack, M.G., Fair, R.B. & Shenderov, A.D. Electrowetting-based actuation of liquid droplets for microfluidic applications. *Applied Physics Letters* **77**, 1725 (2000).

29. Spehar, A.-M. *et al.* Electrokinetic characterization of poly(dimethylsiloxane) microchannels. *Electrophoresis* **24**, 3674-8 (2003).

30. Borowsky, J., Lu, Q. & Collins, G.E. High pressure electroosmotic pump based on a packed bed planar microchip. *Sensors and Actuators B: Chemical* **131**, 333-339 (2008).

31. Ramos, A., Morgan, H., Green, N.G. & Castellanos, A. Ac electrokinetics : a review of forces in microelectrode structures. **2338**, (1998).

32. Senol Mutlu *et al.* Micromachined porous polymer for bubble free electro-osmotic pump. *Micro Electro Mechanical Systems, 2002. The Fifteenth IEEE International Conference on* 19–23 (2002).doi:10.1109/MEMSYS.2002.984050

33. Ramos, A., Morgan, H., Green, N.G. & Castellanos, A. AC electric-field-induced fluid flow in microelectrodes. *Journal of colloid and interface science* **217**, 420–422 (1999).

34. Huang, C.-C., Bazant, M.Z. & Thorsen, T. Ultrafast high-pressure AC electro-osmotic pumps for portable biomedical microfluidics. *Lab on a chip* **10**, 80-5 (2010).

35. van der Wouden, E.E.J., Liang, D., Hermes, D.D.C., Gardeniers, J.G.E.J. & van Den Berg, A. Field-effect control of electro-osmotic flow with synchronized AC-switching of channel and gate potentials. *Micro Electro Mechanical Systems, 2006. MEMS 2006 Istanbul. 19th IEEE International Conference on* 510–513 (2006).doi:10.1109/MEMSYS.2006.1627848

36. Wu, W.-I., Selvaganapathy, P.R. & Ching, C.Y. Transport of particles and microorganisms in microfluidic channels using rectified ac electro-osmotic flow. *Biomicrofluidics* **5**, 013407 (2011).

37. Wu, W.-I., Selvaganapathy, P.R. & Ching, C.Y. Zeta potential modulation and synchronization with AC electric field for rectified electroosmotic flow. *The 5th International conference on Microtechnologies in Medicine and Biology* 68-69 (2009).

38. Lin, C.-H., Wang, J.-H. & Fu, L.-M. Improving the separation efficiency of DNA biosamples in capillary electrophoresis microchips using high-voltage pulsed DC electric fields. *Microfluidics and Nanofluidics* **5**, 403-410 (2008).

39. Meinhart, C.D., Wereley, S.T. & Santiago, J.G. PIV measurements of a microchannel flow. *Experiments in Fluids* **27**, 414-419 (1999).

40. Tretheway, D.C. & Meinhart, C.D. Apparent fluid slip at hydrophobic microchannel walls. *Physics of Fluids* **14**, L9 (2002).

41. Devasenathipathy, S., Santiago, J.G., Wereley, S.T., Meinhart, C.D. & Takehara, K. Particle imaging techniques for microfabricated fluidic systems. *Experiments in Fluids* **34**, 504-514

42. Devasenathipathy, S., Santiago, J.G. & Takehara, K. Particle tracking techniques for electrokinetic microchannel flows. *Analytical chemistry* **74**, 3704-13 (2002).

43. Adamczyk, A.A. & Rimai, L. 2-Dimensional particle tracking velocimetry (PTV): Technique and image processing algorithms. *Experiments in Fluids* **6**, 373-380 (1988).

44. Cowen, E.A. & Monismith, S.G. A hybrid digital particle tracking velocimetry technique. *Experiments in Fluids* **22**, 199-211 (1997).

45. Gendrich, C.P., Koochesfahani, M.M. & Nocera, D.G. Molecular tagging velocimetry and other novel applications of a new phosphorescent supramolecule. *Experiments in Fluids* **23**, 361-372 (1997).

46. Fercher, A. In vivo measurement of fundus pulsations by laser interferometry. *IEEE Journal of Quantum Electronics* **20**, 1469-1471 (1984).

47. Wang, Y., Bower, B.A., Izatt, J.A., Tan, O. & Huang, D. In vivo total retinal blood flow measurement by Fourier domain Doppler optical coherence tomography. *Journal of biomedical optics* **12**, 041215 (2007).

48. Ashauer, M. Thermal flow sensor for liquids and gases based on combinations of two principles. *Sensors and Actuators A: Physical* **73**, 7-13 (1999).

49. Williams, S.J., Park, C. & Wereley, S.T. Advances and applications on microfluidic velocimetry techniques. *Microfluidics and Nanofluidics* **8**, 709-726 (2010).

50. Shinohara, K. *et al.* High-speed micro-PIV measurements of transient flow in microfluidic devices. *Measurement Science and Technology* **15**, 1965-1970 (2004).

51. Yan, D., Nguyen, N.-T., Yang, C. & Huang, X. Visualizing the transient electroosmotic flow and measuring the zeta potential of microchannels with a micro-PIV technique. *The Journal of Chemical Physics* **124**, 021103 (2006).

52. Yan, D., Yang, C., Nguyen, N.-T. & Huang, X. Diagnosis of transient electrokinetic flow in microfluidic channels. *Physics of Fluids* **19**, 017114 (2007).

53. Nabavi, M., Siddiqui, M.H.K. & Dargahi, J. Simultaneous measurement of acoustic and streaming velocities using synchronized PIV technique. *Measurement Science and Technology* **18**, 1811-1817 (2007).

54. Nabavi, M., Siddiqui, K. & Dargahi, J. Analysis of regular and irregular acoustic streaming patterns in a rectangular enclosure. *Wave Motion* **46**, 312-322 (2009).

55. Kuang, C., Qiao, R. & Wang, G. Ultrafast measurement of transient electroosmotic flow in microfluidics. *Microfluidics and Nanofluidics* **11**, 353-358 (2011).

56. Quaglio, M. *et al.* Evaluation of different PDMS interconnection solutions for silicon, Pyrex and COC microfluidic chips. *Journal of Micromechanics and Microengineering* **18**, 055012 (2008).

57. Marcos, Yang, C., Ooi, K.T., Wong, T.N. & Masliyah, J.H. Frequency-dependent laminar electroosmotic flow in a closed-end rectangular microchannel. *Journal of Colloid and Interface Science* **275**, 679-698 (2004).

58. Nikcevic, I. *et al.* Adsorption of fluorescently labeled microbeads on PDMS surfaces. *Proceedings of SPIE* **5718**, 159-167 (2005).

59. Telleman, P., Larsen, U., Philip, J., Blankenstein, G. & Wolff, A. Cell sorting in microfluidic systems. 39 (1998).

60. Blankenstein, G. & Darling Larsen, U. Modular concept of a laboratory on a chip for chemical and biochemical analysis. *Biosensors and Bioelectronics* **13**, 427-438 (1998).

61. McClain, M.A., Culbertson, C.T., Jacobson, S.C. & Ramsey, J.M. Flow Cytometry of Escherichia coli on Microfluidic Devices. *Analytical Chemistry* **73**, 5334-5338 (2001).

62. Ajdari, A. Electrokinetic “ratchet” pumps for microfluidics. *Applied Physics A: Materials Science & Processing* **75**, 271-274 (2002).

63. Fu, A.Y., Spence, C., Scherer, A., Arnold, F.H. & Quake, S.R. A microfabricated fluorescence-activated cell sorter. *Nat Biotech* **17**, 1109-1111 (1999).

64. Li, P.C.H. & Harrison, D.J. Transport, Manipulation, and Reaction of Biological Cells On-Chip Using Electrokinetic Effects. *Analytical Chemistry* **69**, 1564-1568 (1997).

65. Walker, S. & Shapiro, B. A control method for steering individual particles inside liquid droplets actuated by electrowetting. *Lab on a Chip* **5**, 1404–1407 (2005).

66. Fiedler, S., Shirley, S.G., Schnelle, T. & Fuhr, G. Dielectrophoretic Sorting of Particles and Cells in a Microsystem. *Analytical Chemistry* **70**, 1909-1915 (1998).

67. Voldman, J., Gray, M.L., Toner, M. & Schmidt, M.A. A Microfabrication-Based Dynamic Array Cytometer. *Analytical Chemistry* **74**, 3984-3990 (2002).

68. M\üller, T. *et al.* A 3-D microelectrode system for handling and caging single cells and particles. *Biosensors and Bioelectronics* **14**, 247–256 (1999).

69. Leach, J., Mushfique, H., Leonardo, R., Padgett, M. & Cooper, J. An optically driven pump for microfluidics. *Lab on a Chip* **6**, 735–739 (2006).

70. Enger, J. *et al.* Optical tweezers applied to a microfluidic system. *Lab on a Chip* **4**, 196–200 (2004).

71. Li, N., Hsu, C.-H. & Folch, A. Parallel mixing of photolithographically defined nanoliter volumes using elastomeric microvalve arrays. *ELECTROPHORESIS* **26**, 3758-3764 (2005).

72. Horbett, T.A. & Weathersby, P.K. Adsorption of proteins from plasma to a series of hydrophilic-hydrophobic copolymers. I. Analysis with the in situ radioiodination technique. *Journal of Biomedical Materials Research* **15**, 403-423 (1981).

73. Wertz, C.F. & Santore, M.M. Fibrinogen Adsorption on Hydrophilic and Hydrophobic Surfaces: Geometrical and Energetic Aspects of Interfacial Relaxations. *Langmuir* **18**, 706-715 (2001).

74. Tunc, S. *et al.* In situ conformational analysis of fibrinogen adsorbed on Si surfaces. *Colloids and surfaces. B, Biointerfaces* **42**, 219-25 (2005).

75. Ren, X., Bachman, M., Sims, C., Li, G.P. & Allbritton, N. Electroosmotic properties of microfluidic channels composed of poly(dimethylsiloxane). *Journal of Chromatography B: Biomedical Sciences and Applications* **762**, 117-125 (2001).

76. Peterson, S.L., McDonald, A., Gourley, P.L. & Sasaki, D.Y. Poly(dimethylsiloxane) thin films as biocompatible coatings for microfluidic devices: Cell culture and flow studies with glial cells. *Journal of Biomedical Materials Research Part A* **72A**, 10-18 (2005).

77. Tan, H.M.L., Fukuda, H., Akagi, T. & Ichiki, T. Surface modification of poly(dimethylsiloxane) for controlling biological cells' adhesion using a scanning radical microjet. *Thin Solid Films* **515**, 5172-5178 (2007).

78. Vickers, J.A., Caulum, M.M. & Henry, C.S. Generation of Hydrophilic Poly(dimethylsiloxane) for High-Performance Microchip Electrophoresis. *Analytical Chemistry* **78**, 7446-7452 (2006).

79. Berdichevsky, Y., Khandurina, J., Guttman, A. & Lo, Y.-H. UV/ozone modification of poly(dimethylsiloxane) microfluidic channels. *Sensors and Actuators B: Chemical* **97**, 402-408 (2004).

80. Efimenko, K., Wallace, W.E. & Genzer, J. Surface Modification of Sylgard-184 Poly(dimethyl siloxane) Networks by Ultraviolet and Ultraviolet/Ozone Treatment. *Journal of Colloid and Interface Science* **254**, 306-315 (2002).

81. Hillborg, H., Tomczak, N., Olàh, A., Schönherr, H. & Vancso, G.J. Nanoscale Hydrophobic Recovery: A Chemical Force Microscopy Study of UV/Ozone-Treated Cross-Linked Poly(dimethylsiloxane). *Langmuir* **20**, 785-794 (2003).

82. Chen, H.-Y. & Lahann, J. Fabrication of Discontinuous Surface Patterns within Microfluidic Channels Using Photodefinable Vapor-Based Polymer Coatings. *Analytical Chemistry* **77**, 6909-6914 (2005).

83. Chen, H.-Y., Elkasabi, Y. & Lahann, J. Surface Modification of Confined Microgeometries via Vapor-Deposited Polymer Coatings. *Journal of the American Chemical Society* **128**, 374-380 (2005).

84. Chen, H.-Y., McClelland, A.A., Chen, Z. & Lahann, J. Solventless Adhesive Bonding Using Reactive Polymer Coatings. *Analytical Chemistry* **80**, 4119-4124 (2008).

85. Morra, M. On the aging of oxygen plasma-treated polydimethylsiloxane surfaces. *Journal of Colloid and Interface Science* **137**, 11-24 (1990).

86. Hillborg, H. & Gedde, U.W. Hydrophobicity changes in silicone rubbers. *Dielectrics and Electrical Insulation, IEEE Transactions on* **6**, 703-717 (1999).

87. Hu, S. *et al.* Surface Modification of Poly(dimethylsiloxane) Microfluidic Devices by Ultraviolet Polymer Grafting. *Analytical Chemistry* **74**, 4117-4123 (2002).

88. Lyman, D.J. *et al.* The development and implantation of a polyurethane hemispherical artificial heart. *Transactions - American Society for Artificial Internal Organs* **17**, 456-63 (1971).

89. Boretos, J.W. & Pierce, W.S. Segmented polyurethane: a polyether polymer. An initial evaluation for biomedical applications. *Journal of biomedical materials research* **2**, 121-30 (1968).

90. Brash, J.L., Fritzinger, B.K. & Bruck, S.D. Development of block copolyether-urethane intra-aortic balloons and other medical devices. *Journal of biomedical materials research* **7**, 313-34 (1973).

91. Devanathan, T., Sluetz, J.E. & Young, K.A. In vivo thrombogenicity of implantable cardiac pacing leads. *Biomaterials, medical devices, and artificial organs* **8**, 369-79 (1980).

92. Tsutsui, T., Imamura, E. & Kayanagi, H. The development of nonstended trileaflet valve prosthesis. Artif Organs. *Artif Organs (Japan)* **10**, 590-593 (1981).

93. Lyman, D., Seare, W. & Albo, D. Polyurethane elastomers in surgery. *International Journal of Polymeric Mater* **5**, 211-229 (1977).

94. Takahara, A., Tashita, J.I. & Kajiyama, T. Microphase separated structure, surface composition and blood compatibility of segmented poly(urethaneureas) with various soft segment components. *Polymer* **26**, 987-996 (1985).

95. Okano, T. *et al.* Effect of hydrophilic and hydrophobic microdomains on mode of interaction between block polymer and blood platelets. *Journal of biomedical materials research* **15**, 393-402 (1981).

96. Okano, T. *et al.* Hydrophilic-hydrophobic microdomain surfaces having an ability to suppress platelet aggregation and their in vitro antithrombogenicity. *Journal of biomedical materials research* **20**, 919-27 (1986).

97. Lennon, G.M. *et al.* “Firm” versus “soft” double pigtail ureteric stents: a randomised blind comparative trial. *European urology* **28**, 1-5 (1995).

98. Watkinson, A.F., Ellul, J., Entwisle, K., Mason, R.C. & Adam, A. Esophageal carcinoma: initial results of palliative treatment with covered self-expanding endoprostheses. *Radiology* **195**, 821-7 (1995).

99. Bruin, P., Meeuwsen, E.A., van Andel, M.V., Worst, J.G. & Pennings, A.J. Autoclavable highly cross-linked polyurethane networks in ophthalmology. *Biomaterials* **14**, 1089-97 (1993).

100. Bakker, D. *et al.* Biocompatibility of a polyether urethane, polypropylene oxide, and a polyether polyester copolymer. A qualitative and quantitative study of three

alloplastic tympanic membrane materials in the rat middle ear. *Journal of biomedical materials research* **24**, 489-515 (1990).

101. Han, D.K. *et al.* In vivo canine studies of a Sinkhole valve and vascular graft coated with biocompatible PU-PEO-SO3. *ASAIO journal (American Society for Artificial Internal Organs : 1992)* **39**, M537-41

102. van der Giessen, W.J. *et al.* Marked inflammatory sequelae to implantation of biodegradable and nonbiodegradable polymers in porcine coronary arteries. *Circulation* **94**, 1690-7 (1996).

103. Akiyama, N., Esato, K., Fujioka, K. & Zempo, N. A comparison of CORVITA and expanded polytetrafluoroethylene vascular grafts implanted in the abdominal aortas of dogs. *Surgery today* **27**, 840-5 (1997).

104. Okoshi, T., Soldani, G., Goddard, M. & Galletti, P.M. Penetrating micropores increase patency and achieve extensive endothelialization in small diameter polymer skin coated vascular grafts. *ASAIO journal (American Society for Artificial Internal Organs : 1992)* **42**, M398-401

105. Marois, Y. *et al.* Vascugraft microporous polyesterurethane arterial prosthesis as a thoraco-abdominal bypass in dogs. *Biomaterials* **17**, 1289-300 (1996).

106. Marois, Y. *et al.* A novel microporous polyurethane vascular graft: in vivo evaluation of the UTA prosthesis implanted as infra-renal aortic substitute in dogs. *Journal of investigative surgery : the official journal of the Academy of Surgical Research* **6**, 273-88

107. Marois, Y. *et al.* In vivo evaluation of hydrophobic and fibrillar microporous polyetherurethane urea graft. *Biomaterials* **10**, 521-31 (1989).

108. Brash, J.L. Exploiting the current paradigm of blood-material interactions for the rational design of blood-compatible materials. *Journal of biomaterials science Polymer edition* **11**, 1135-1146 (2000).

109. LEE, J., LEE, H. & ANDRADE, J. Blood compatibility of polyethylene oxide surfaces. *Progress in Polymer Science* **20**, 1043-1079 (1995).

110. Feng, W., Brash, J.L. & Zhu, S. Non-biofouling materials prepared by atom transfer radical polymerization grafting of 2-methacryloloxyethyl phosphorylcholine: separate effects of graft density and chain length on protein repulsion. *Biomaterials* **27**, 847-55 (2006).

111. Martwiset, S., Koh, A.E. & Chen, W. Nonfouling characteristics of dextran-containing surfaces. *Langmuir : the ACS journal of surfaces and colloids* **22**, 8192-6 (2006).

112. Saito, N., Nojiri, C., Kuroda, S. & Sakai, K. Photochemical grafting of alpha-propylsulphate-poly(ethylene oxide) on polyurethane surfaces and enhanced antithrombogenic potential. *Biomaterials* **18**, 1195-7 (1997).

113. van der Heiden, A.P., Goebbels, D., Pijpers, A.P. & Koole, L.H. A photochemical method for the surface modification of poly(etherurethanes) with phosphorylcholine-containing compounds to improve hemocompatibility. *Journal of biomedical materials research* **37**, 282-90 (1997).

114. Fujimoto, K., Inoue, H. & Ikada, Y. Protein adsorption and platelet adhesion onto polyurethane grafted with methoxy-poly(ethylene glycol) methacrylate by plasma technique. *Journal of biomedical materials research* **27**, 1559-67 (1993).

115. Fujimoto, K., Tadokoro, H., Ueda, Y. & Ikada, Y. Polyurethane surface modification by graft polymerization of acrylamide for reduced protein adsorption and platelet adhesion. *Biomaterials* **14**, 442-8 (1993).

116. Kim, Y.H., Han, D.K., Park, K.D. & Kim, S.H. Enhanced blood compatibility of polymers grafted by sulfonated PEO via a negative cilia concept. *Biomaterials* **24**, 2213-2223 (2003).

117. Nojiri, C. *et al.* Blood compatibility of PEO grafted polyurethane and HEMA/styrene block copolymer surfaces. *Journal of biomedical materials research* **24**, 1151-71 (1990).

118. Tan, J. & L. Brash, J. Nonfouling biomaterials based on polyethylene oxide-containing amphiphilic triblock copolymers as surface modifying additives: Synthesis and characterization of copolymers and surface properties of copolymer–polyurethane blends. *Journal of Applied Polymer Science* **108**, 1617-1628 (2008).

119. Freij-Larsson, C., Nylander, T., Jannasch, P. & Wesslén, B. Adsorption behaviour of amphiphilic polymers at hydrophobic surfaces: effects on protein adsorption. *Biomaterials* **17**, 2199-2207 (1996).

120. AMIJI, M. & PARK, K. Prevention of protein adsorption and platelet adhesion on surfaces by PEO/PPO/PEO triblock copolymers. *Biomaterials* **13**, 682-692 (1992).

121. Lee, J.H., Kopecek, J. & Andrade, J.D. Protein-resistant surfaces prepared by PEO-containing block copolymer surfactants. *Journal of biomedical materials research* **23**, 351-68 (1989).

122. Folch, A., Mezzour, S. & Du, M. Stacks of Microfabricated Structures as Scaffolds for Cell Culture and Tissue Engineering. *Tissue Engineering* 207-214 (2000).

123. Kuo, J.S. *et al.* Microfabricating high-aspect-ratio structures in polyurethane-methacrylate (PUMA) disposable microfluidic devices. *Lab on a chip* **9**, 1951-6 (2009).

124. Shen, J.-Y., Chan-Park, M.B.-E., Feng, Z.-Q., Chan, V. & Feng, Z.-W. UV-embossed microchannel in biocompatible polymeric film: application to control of cell shape and orientation of muscle cells. *Journal of biomedical materials research. Part B, Applied biomaterials* **77**, 423-30 (2006).

125. Xu, J., Locascio, L., Gaitan, M. & Lee, C.S. Room-Temperature Imprinting Method for Plastic Microchannel Fabrication. *Analytical Chemistry* **72**, 1930-1933 (2000).

126. Rossier, J.S. *et al.* Plasma etched polymer microelectrochemical systems. *Lab on a chip* **2**, 145-50 (2002).

127. Haraldsson, K.T. *et al.* 3D polymeric microfluidic device fabrication via contact liquid photolithographic polymerization (CLiPP). *Sensors and Actuators B: Chemical* **113**, 454-460 (2006).

128. Piccin, E. *et al.* Polyurethane from biosource as a new material for fabrication of microfluidic devices by rapid prototyping. *Journal of chromatography. A* **1173**, 151-8 (2007).

129. Thorsen, T., Roberts, R.W., Arnold, F.H. & Quake, S.R. Dynamic Pattern Formation in a Vesicle-Generating Microfluidic Device. *Physical Review Letters* **86**, 4163-4166 (2001).

130. Kim, Y.S., Lee, H.H. & Hammond, P.T. High density nanostructure transfer in soft molding using polyurethane acrylate molds and polyelectrolyte multilayers. *Nanotechnology* **14**, 1140-1144 (2003).

131. Sask, K.N., Berry, L.R., Chan, A.K.C. & Brash, J.L. Modification of Polyurethane Surface with an Antithrombin-Heparin Complex for Blood Contact: Influence of Molecular Weight of Polyethylene Oxide used as Linker/Spacer. *Langmuir* **submitted**, (2011).

132. Böswald, M. *et al.* Biocompatibility testing of a new silver-impregnated catheterin vivo. *Infection* **27**, S38-S42 (1999).

133. Böswald, M. *et al.* Thrombogenicity testing of central venous cathetersin vitro. *Infection* **27**, S30-S33 (1999).

134. Hentschel, T. & Münstedt, H. Thermoplastic polyurethane—The material used for the erlanger silver catheter. *Infection* **27**, S43-S45 (1999).

135. Belanger, M.-C. *et al.* Selection of a Polyurethane Membrane for the Manufacture of Ventricles for a Totally Implantable Artificial Heart: Blood Compatibility and Biocompatibility Studies. *Artificial Organs* **24**, 879-888 (2000).

136. Cornelius, R.M., Macri, J. & Brash, J.L. Interfacial interactions of apolipoprotein AI and high density lipoprotein: Overlooked phenomena in blood-material contact. *Journal of biomedical materials research. Part A* 1-7 (2011).doi:10.1002/jbm.a.33169

137. Barron, V. Durability of APC2/Polyurethane adhesive joints for biomedical applications. *International Journal of Adhesion and Adhesives* **20**, 361-366 (2000).

138. Moraes, C. *et al.* Integrating polyurethane culture substrates into poly(dimethylsiloxane) microdevices. *Biomaterials* **30**, 5241-50 (2009).

139. Pattekar, A.V. & Kothare, M.V. Novel microfluidic interconnectors for high temperature and pressure applications. *Journal of Micromechanics and Microengineering* **13**, 337-345 (2003).

140. Lee, E.S., Howard, D., Liang, E., Collins, S.D. & Smith, R.L. Removable tubing interconnects for glass-based micro-fluidic systems made using ECDM. *Journal of Micromechanics and Microengineering* **14**, 535-541 (2004).

141. Tze-Jung, Y., Sangwook, L., Weileun, F. & Yu-Chong, T. Micromachined rubber O-ring micro-fluidic couplers. *Proceedings IEEE Thirteenth Annual International Conference on Micro Electro Mechanical Systems (Cat. No.00CH36308)* 624-627doi:10.1109/MEMSYS.2000.838590

142. Bhagat, A.A.S., Jothimuthu, P., Pais, A. & Papautsky, I. Re-usable quick-release interconnect for characterization of microfluidic systems. *Journal of Micromechanics and Microengineering* **17**, 42-49 (2007).

143. Tsai, J.-H. & Lin, L. Micro-to-macro fluidic interconnectors with an integrated polymer sealant. *Journal of Micromechanics and Microengineering* **11**, 577-581 (2001).

144. Puntambekar, A. & Ahn, C.H. Self-aligning microfluidic interconnects for glass- and plastic-based microfluidic systems. *Journal of Micromechanics and Microengineering* **12**, 35-40 (2002).

145. Liu, J., Hansen, C. & Quake, S.R. Solving the “World-to-Chip” Interface Problem with a Microfluidic Matrix. *Analytical Chemistry* **75**, 4718-4723 (2003).

146. Chang-Yen, D. a., Myszka, D.G. & Gale, B.K. A Novel PDMS Microfluidic Spotter for Fabrication of Protein Chips and Microarrays. *Journal of Microelectromechanical Systems* **15**, 1145-1151 (2006).

147. Lo, R. & Meng, E. Reusable, adhesiveless and arrayed in-plane microfluidic interconnects. *Journal of Micromechanics and Microengineering* **21**, 054021 (2011).

148. Glasgow, I.K., Beebe, D.J. & White, V.E. Design rules for polyimide solvent bonding. *Sensors and Materials* **11**, 269-278 (1999).

149. Lin, C., Chao, C. & Lan, C. Low azeotropic solvent for bonding of PMMA microfluidic devices. *Sensors and Actuators B: Chemical* **121**, 698-705 (2007).

150. Huang, F.-C., Chen, Y.-F. & Lee, G.-B. CE chips fabricated by injection molding and polyethylene/thermoplastic elastomer film packaging methods. *Electrophoresis* **28**, 1130-7 (2007).

151. Roberts, M.A., Rossier, J.S., Bercier, P. & Girault, H. UV Laser Machined Polymer Substrates for the Development of Microdiagnostic Systems. *Analytical chemistry* **69**, 2035-42 (1997).

152. Klank, H., Kutter, J.P. & Geschke, O. CO(2)-laser micromachining and back-end processing for rapid production of PMMA-based microfluidic systems. *Lab on a chip* **2**, 242-6 (2002).

153. Choi, D.-G., Jang, S.G., Yu, H.K. & Yang, S.-M. Two-Dimensional Polymer Nanopattern by Using Particle-Assisted Soft Lithography. *Chemistry of Materials* **16**, 3410-3413 (2004).

154. McDonald, J.C. & Whitesides, G.M. Poly(dimethylsiloxane) as a Material for Fabricating Microfluidic Devices. *Accounts of Chemical Research* **35**, 491-499 (2002).

155. Rosu, D., Rosu, L. & Cascaval, C.N. IR-change and yellowing of polyurethane as a result of UV irradiation. *Polymer Degradation and Stability* **94**, 591-596 (2009).

156. Liu, Y., Fanguy, J.C., Bledsoe, J.M. & Henry, C.S. Dynamic Coating Using Polyelectrolyte Multilayers for Chemical Control of Electroosmotic Flow in Capillary Electrophoresis Microchips. *Analytical Chemistry* **72**, 5939-5944 (2000).

157. Tandon, V., Bhagavatula, S.K., Nelson, W.C. & Kirby, B.J. Zeta potential and electroosmotic mobility in microfluidic devices fabricated from hydrophobic polymers: 1. The origins of charge. *Electrophoresis* **29**, 1092-101 (2008).

158. Wouden, E. *et al.* Field-effect control of electro-osmotic flow in microfluidic networks. *Colloids and Surfaces A: Physicochemical and Engineering Aspects* **267**, 110-116 (2005).

159. Vajandar, S.K. *et al.* Field-Effect Control of Electroosmotic Pumping Using Porous Silicon–Silicon Nitride Membranes. *Journal of Microelectromechanical Systems* **18**, 1173-1183 (2009).

160. Horiuchi, K. & Dutta, P. Electrokinetic flow control in microfluidic chips using a field-effect transistor. *Lab on a chip* **6**, 714-23 (2006).

161. Karnik, R. *et al.* Electrostatic Control of Ions and Molecules in Nanofluidic Transistors. *Nano Letters* **5**, 943-948 (2005).